Modelling and Analysis of Drosophila Early Visual System

A Systems Engineering Approach

Carlos Ricardo Luna Ortiz

Department of Automatic Control and Systems Engineering
University of Sheffield

This dissertation is submitted for the degree of
Doctor of Philosophy

February 2018

To *God* and my beloved *parents*. Con amor a *Dios* y a mis *padres*.

Acknowledgements

This thesis could have not been completed without the support, time, patience, collaboration, guidance and company of many people and institutions around me.

First I would like to deeply thank my supervisor Prof. Daniel Coca, who since the very early stages of my Ph. D. journey has been hollistically supportive. In the professional side, during our formal and casual meetings his insight, excitement for research and imagination provided a great paltform for discussions that led to fruitful sources of ways to move forward. On the other hand, he helped and advise me when I was confronted with non academic related situations. Also I would like to express my gratitude to Dr. Uwe Friederich for the very helpful discussion that we had about his work and the pointers that he gave me, both contributed greatly to get my research started on the right track.

Before naming people and as a anticipated form of apology for missing someone, I would like to thank every person that shared space or time with me during this journey, thanks for being there I learnt a lot from everyone around me. Thanks to Dr. Ernesto Vidal and Dr. Uriel Marinez for helping me settling down at the very beginning of my Ph D, their support in academic and personal matters was invaluable.Also I would like to thank my fellow citizens and collegues Daniela, Jose, Francisco, Victor, Francisco for being being part of my journey and sharing their time, emotions and struggles with me. Also I owe a lot to the people who shared the office with me, our professional and personal chats were very useful during fun times and help in coping with more challenging situations, so thanks to Suradet, Matei, Jose Antonio and Carlos. I would also like to thank Erick, Aldo and Jose Roberto with whom I spent more time with because personal and professional circumstances, your patience,time and sincere affection were crucial in this journey for me. I hope somehow I also contributed to your life as well. In addition I would thank Adam and Dorian, my most recent colleagues, with whom I share the office. Our every day interaction has really made a mark on my personal and professional development.

A special thanks to my parents Sergio Luna and M. Guadalupe Ortiz, their support not just during this journey but my entire life is the reason why I am here. The last person I would like to thank is Briseida Garcia, her ways and wisdom have given me the opportunity to be a better human.

Last but not least, I would like to thank CONACyT, my Mexican sponsor during most of my Ph. D. journey. And all the institutions here in the United Kingdom, starting by the University of Sheffield, that have made this Ph. D. possible.

Abstract

Over the past century or so *Drosophila* has been established as an ideal model organism to study, among other things, neural computation and in particular sensory processing. In this respect there are many features that make *Drosophila* an ideal model organism, especially the fact that it offers a vast amount of genetic and experimental tools for manipulating and interrogating neural circuits. Whilst comprehensive models of sensory processing in *Drosophila* are not yet available, considerable progress has been made in recent years in modelling the early stages of sensory processing. When it comes to visual processing, accurate empirical and biophysical models of the R1-R6 photoreceptors were developed and used to characterize nonlinear processing at photoreceptor level and to demonstrate that R1-R6 photoreceptors encode phase congruency.

A limitation of the latest photoreceptor models is that these do not account explicitly for the modulation of photoreceptor responses by the network of interneurones hosted in the lamina. As a consequence, these models cannot describe in a unifying way the photoreceptor response in the absence of the feedback from the downstream neurons and thus cannot be used to elucidate the role of interneurones in photoreceptor adaptation.

In this thesis, electrophysiological photoreceptor recordings acquired in-vivo from wild-type and histamine defficient mutant fruit flies are used to develop and validate new comprehensive models of R1-R6 photoreceptors, which not only predict the response of these photoreceptors in wild-type and mutant fruit flies, over the entire environmental range of light intensities but also characterize explicitly the contribution of lamina neurons to photoreceptor adaptation. As a consequence, the new models provide suitable building blocks for assembling a complete model of the retina which takes into account the true connectivity between photoreceptors and downstream interneurones.

A recent study has demonstrated that R1-R6 photoreceptors employ nonlinear processing to selectively encode and enhance temporal phase congruency. It has been suggested that this processing strategy achieves an optimal trade-off between the two competing goals of minimizing distortion in decoding behaviourally relevant stimuli features and minimizing the information rate, which ultimately enables more efficient downstream processing of spatio-temporal visual stimuli for edge and motion detection.

Using rigorous information theoretic tools, this thesis derives and analyzes the rate-distortion characteristics associated with the linear and nonlinear transformations performed by photoreceptors on a stimulus generated by a signal source with a well defined distribution.

Table of contents

List of figures

List of tables

Chapter 1

Introduction

1.1 Background and Motivation

Understanding how the brain works, its anatomy and structure, as well as its information processing and computational capabilities is considered to be one of the biggest engineering challenges of this century.

The fruit fly, *Drosophila Melanogaster*, is one of the most popular model organisms. *Drosophila* fly has been used for around 100 years (Beckingham et al., 2007) as a genetic model. The main reasons why the fruit fly has received a lot of attention include: ease of culture and maintenance, short life cycle, low number of chromosomes, the fact that about 60% of genes found in humans have counterparts in *Drosophila*, also the complete genome sequence of Drosophila was published in 2000. Besides the previous facts, the fact that *Drosophila* was selected as a genetic model, provided a unique opportunity to relate behavioral, physiological and developmental studies to be related to changes in genes (Paulk et al., 2013).

The focus of this thesis is the early visual system of the fruit fly. For many years *Drosophila* has been used to investigate the information processing principles underlying not only neurons in the visual system (Borst, 2009) but also other sensory systems as well (Ai et al., 2010; Kim et al., 2011, 2015).

As a result of the synergistic combination of the almost complete wiring diagram of the visual system (Borst, 2009), the protocols for genetic manipulation and data collection from *in vivo* experiments (Hadjieconomou et al., 2011), great progress has been made in modelling *Drosophila's* visual system. In recent years, our understanding of the information processing that takes place in the fly's early visual system has increased as a result of the biophysical and empirical modeling efforts reported by (Dau et al., 2016; Hardie, 2012a; Hardie and Postma, 2008b; Hardie and Raghu, 2001a; Hateren and Snippe, 2006; Song et al., 2012) and

(Borst, 2009, 2014; Friederich et al., 2016; Hateren, 1992; van Hateren, 1997) respectively. The outcome of these studies has confirmed some theories, for example of the molecular mechanisms in phototransduction cascade (Song et al., 2012). It has also, answered some questions and elucidated the role of nonlinearity in photoreceptors' response to naturalistic stimulation. In addition, it has set the foundation to ask new questions, such as what is the role of the lamina, the neural layer that follows the retina and which neurons are connected bidirectionally with photoreceptors in the retina, in shaping the response of photoreceptors, and produce complete and more accurate models of *Drosophila's* early visual system.

1.2 Aims and objectives

The aim of this work is to use system identification techniques and previously reported empirical fruit fly photoreceptor's models to develop and analyse data-driven models of *Drosophila's* early visual system.

The main goal is to develop a new photoreceptor model that represents explicitly the connectivity and interactions of photoreceptors with the large monopolar cells such that the same model can be used to describe not only the photoreceptor responses in the wild-type fruit flies but also in histamine deficient mutants, by simply removing the synaptic interconnection between photoreceptors and the lamina.

The main advantages of such model over existing ones are: (i) the fact that it can be used to characterise the contribution of the lamina to photoreceptor adaptation and (ii) that it can form the building block for a complete anatomically realistic retina model.

In order to achieve this goal, data collected from wild-type and histamine deficient ($\mathrm{hdc}^{\mathrm{JK910}}$) flies was used. Due to the lack of histamine, the connection between photoreceptors and lamina in the $\mathrm{hdc}^{\mathrm{JK910}}$ doesn't take place. This fact indicates that these flies are blind. By comparing the responses of photoreceptors of wild and $\mathrm{hdc}^{\mathrm{JK910}}$ flies, it is possible to obtain a functional characterisation of the network of lamina interneurones in modulating the photoreceptor's response.

The second goal of this thesis is to use rate-distortion analysis, a concept from information theory, together with photoreceptor models and their recently reported (Friederich et al., 2016) phase congruency detection properties to characterize the processing of visual information in *Drosophila* photoreceptors.

1.3 Thesis outline

The thesis is organised in seven Chapters that are summarised below.

- *Chapter 2* reviews the basic anatomical and functional organisation of *Drosophila* early visual system. The main signalling mechanisms involved in the phototransduction cascade by which visual light stimuli are converted into electrical signals are presented. The second part of the chapter provides a succinct description of the experimental methods and data used to develop and validate the models derived in this thesis.

- *Chapter 3* provides an overview of the modelling and analysis methods and tools used throughout the thesis. A short survey on system identification approaches used in neuroscience is followed by a more in-depth description of the NARMAX methodology, the main system identification framework used in this thesis. The polynomial NARMAX expansion is discussed. The Chapter also introduces the higher order frequency analysis framework that is used to characterise the linear and nonlinear transductions at photoreceptor level.

- *Chapter 4* reviews a state-of-the-art empirical photoreceptor model highlighting its limitation in reproducing the response of blind hdc$^{\mathrm{JK910}}$ fly's photoreceptor. In order to address this limitation a novel empirical model, which features mean and contrast gain adaptation strategies is developed and validated.

- *Chapter 5* introduces a new PR1-6/LMC retinal network model which has as the main building block the model developed in Chapter 4. Specifically, a new model architecture that exposes the lamina contribution explicitly is introduced and validated.

- *Chapter 6* characterises separately, for the first time, the linear and nonlinear transductions at photoreceptor level, using an information theoretic framework. Particularly, the Chapter presents a rate-distortion (R-D) analysis of photoreceptor transductions when stimulated with pulses, which are signals with high phase-congruency content. The efficiency and robustness of the linear and nonlinear transductions of photoreceptors are assessed.

- *Chapter 7* is the concluding Chapter that provides a summary of the results, discusses their broader implications and suggests opportunities and directions of future research.

The key novel and significant contributions to Science of this thesis are the following. Firstly, a new model of Drosophila R1-R6 photoreceptors was developed. This model can be tuned to predict responses of wild and histamine deficient fruit fly photoreceptors. The model represents a significant improvement on the previously reported models which were capable of predicting responses of photoreceptors of just wild flies. The second relevant contribution is the development of the empirical model of Drosophila R1-6/LMC retinal network. The objective of this model is to explicitly model the contribution of the lamina interneurons in shaping the response at photorecptor level. The model can be used to build a biologically realistic model of the entire retina, which captures the actual connectivity between photoreceptors and the lamina. The thesis for the first time provides a rigorous information-theoretic characterisation of the linear and nonlinear processing at photoreceptor level, using rate distortion theory.

Chapter 2

Overview of Drosophila's Early Visual System, Experimental Methods and Data

2.1 Introduction

In neuroscience, one of the main questions that need to be answered is how the brain of animals, including the human, carries out computations. This is a major undertaking since the brain is a complex and highly interconnected system (Bassett and Gazzaniga, 2011). So in oder to simplify the study of such a complex system, it is common to use 'model' organisms which offer particular 'tools' to better understand the brain (Bellen et al., 2010; Heintz, 2001; Kalueff et al., 2014; Rankin et al., 1990).

One of the most modelled organisms is *Drosophila*, the fruit fly. Besides being easy to breed and keep, the scientific community has developed a comprehensive molecular and genetic 'toolbox' which has contributed to the fact that *Drosophila* has over hundred years of history in helping to advance neuroscience research (Bellen et al., 2010). Furthermore, *Drosophila* is a complex organism that features developmental and behavioral aspects which have parallels in humans(Beckingham et al., 2007).

Despite being used to study different sensory systems such as olfaction or taste, in this thesis the focus is mainly on the visual system, more particularly on the early visual system. The type of studies, related to the visual system, that wild and mutant *Drosophila* flies have been used for include: phototransduction cascade, i.e. the molecular mechanisms that occur so light can be turned into neural representation, motion detection, colour vision and phase congruency detection among others.

In the past, the visual system of invertebrates has been studied using both bigger flies such as *Calliphora*, *Musca*, and *Drosophila* itself. The combined body of knowledge generated has helped to increase the understanding of the adaptive visual processing strategies in the early visual system.

The layout of this chapter is as follows. Section 2 provides a brief overview of the anatomy of *Drosophila*'s early visual system.

Section 3 covers the anatomy of photoreceptors in more detail and summarizes the molecular mechanisms of phototransduction.

The hardware setup and data acquisition system used to obtain the experimental data are explained in section 4. This data was used throughout the thesis for the derivation of *Drosophila* photoreceptors and retinal network models.

Section 5 describes in more detail the experimental stimuli and intracellular recordings obtained from wild-type and mutant hdc$^{\mathrm{JK910}}$ fruit flies, highlighting the similarities and differences between responses to the same stimulus sequence.

The concluding remarks of the chapter and their relevance to the rest of the thesis are provided in section 6.

2.2 The Anatomy of the Early Visual System of *Drosophila*

Ocelli, a three small lens organ, and two large compound eyes constitute the visual system of an adult *Drosohpila melanogaster* fly. This organ is considered to be primitive (Heisenberg and Wolf, 2013). Its complexity and role in the visual system vary considerably depending on the insect (Mizunami, 1995; Wilson, 1978). The focus of this thesis is on the visual processing mechanisms that take place in photoreceptors and neurons in the lamina. This path has the compound eye as the entry point to the visual system.

A general diagram of the *Drosophila's* visual system can be found in Fig. 2.1.

Drosophila's retina is an optically compound eye which is made up of a regularly arranged array of about 800 small elements, which share the same anatomical structure, called facets or ommatidia. Every single ommatidium is composed of 8 photoreceptors R1-R8 which in conjunction are capable of detecting electromagnetic waves that range from the UV to green wavelengths (Heisenberg and Buchner, 1977). Each of this units possesses a photosensitive rhabdomere, a stack of about 30000 very fine microvilli, which is extracellular and points to a central canal inside the facet. It is precisely in each of these individual microvilli that the so-called phototransduction cascade takes place (Hardie and Postma, 2008c; Minke and Hardie, 2000) and as a result, the captured light is transformed into electrical signals that are transmitted to other further ganglionic relays inside the *Drosophila's* brain to make sense of the visual stimuli. Out of the 8 available photoreceptors, the 6 outer/peripheral ones R1-R6, which form a trapezoidal pattern around the inner stacked R7/R8 photoreceptors, have

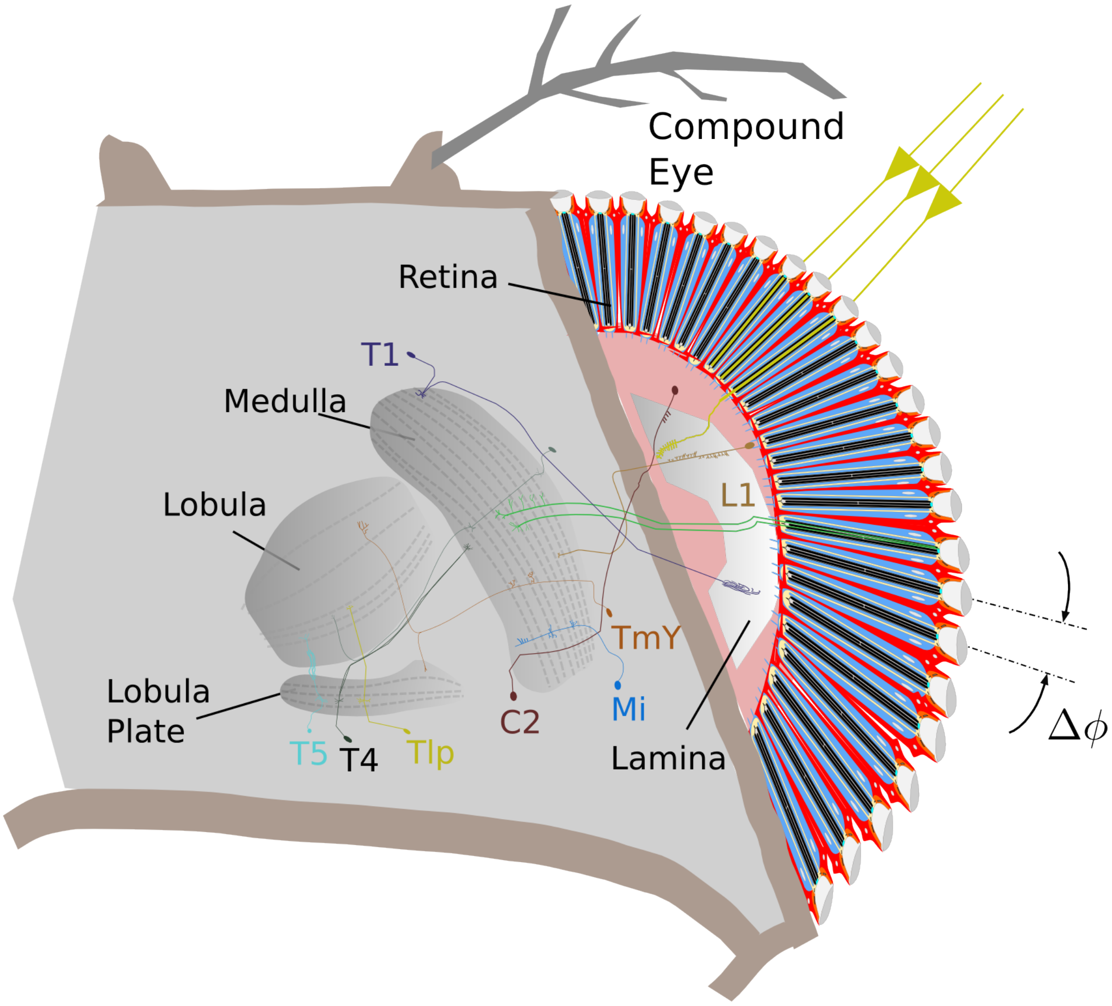

Fig. 2.1 *Drosophila's* Visual System Overview adapted from (Borst, 2009). This figure shows a cross-section of the interconnection of the retina with the remaining visual ganglia(Lamina, Medulla, Lobula and Lobula Plate) that participate in higher visual processes. It shows bushy T1, T4-T5 cells, transmedulla neuron TmY, centrifugal cell C2, large monopolar cell L1 and intrinsic medulla neuron Mi. The interommatidial angle and light energy are represented by $\Delta\phi$ and yellow arrows respectively.

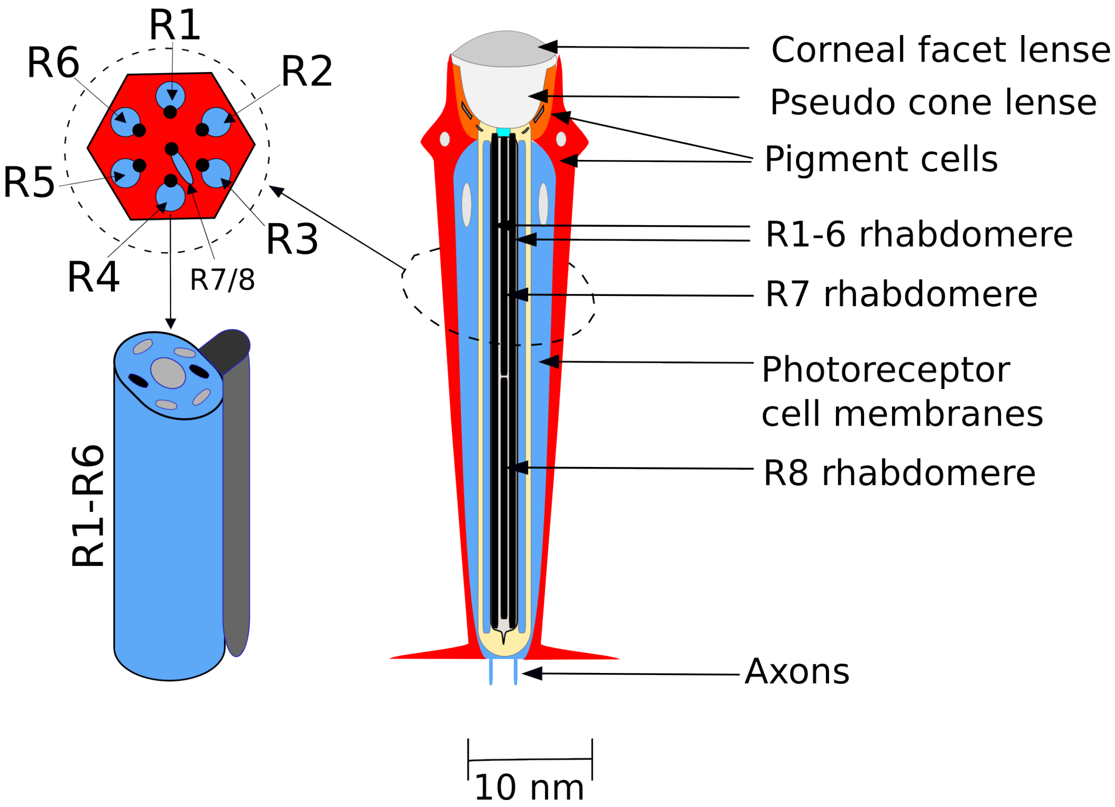

Fig. 2.2 Ommatidium Anatomy. This figure shows a single ommatidium with its outer(R1-6) and its inner photoreceptors (R7-8). The cross-section indicates the spatial disposition of the photoreceptors in each ommatidium. Also, a more detailed figure of an individual outer photoreceptor is depicted. The rhabdomere ultrastructure is shown in black. This ultrastructure is composed of microvilli and acts as a light guide.

rhabdomeres that cover the full length of its hosting ommatidium. It has been reported that the outer photoreceptors are responsible for motion vision on a broad range of wavelengths (Borst, 2014; Rister et al., 2007; Vogt and Desplan, 2007). Whilst the remaining R7/R8 photoreceptors are known to mediate colour and polarized vision (Borst, 2014; Hardie, 2012b; Morante and Desplan, 2008; Yamaguchi et al., 2008) The anatomy of a single ommatidium is presented in Fig. 2.2

Once visual information has been translated from light into electrical signals by the photoreceptors located in the retina, this information is transmitted to the optical lobe: lamina, medulla, lobula and lobula plate. Each of these layers is built so it has a retinotopically arrangement by columns that reflect the layout in the retina(Borst, 2014). More precisely, the outer photoreceptors extend their axons to connect with the interneurons located in the so called lamina cartridges. These interneurons include large monopollar L1-L5, amacrine and centrifugal cells (Meinertzhagen and Sorra, 2001). On the other hand, the inner photoreceptors R7/R8 terminate not in the lamina but in the medulla. A very detailed explanation of the 'wiring' diagram for the *Drosophila's* visual system can be found in (Hadjieconomou et al., 2011).

The visual spacial resolution in *Drosophila* melanogaster is given by its interommatidial angle which is about 5 degrees (Borst, 2014). Since this interommatidial angle is the same as the angle between any pair of rhabdormeres withing the same ommatidium, it follows that each photoreceptor belonging to the same ommatidium has a different visual field, which is the same as one of the photoreceptors located in one of the 6 neighbouring ommatidia (Kirschfeld, 1967). Actually, photoreceptors of neighbouring ommatidia that share the same visual field have a common postsynaptic target in the lamina cartridges (Trujillo-Cenóz, 1965), refer to Fig. 2.3. This type of arrangement is known as synaptic superposition and has the advantage of increased sensitivity and signal-to-noise ratio without sacrificing resolution.

Previous works (Hardie, 1987, 1989; Pantazis et al., 2008) have reported that communication between retina and lamina use histamine as neurotransmitter. This communication occurs between photoreceptors in the retina and large monopolar cells L1-L3 and amacrine cells in the lamina. Also, there are gap junction connections between photoreceptors hosted in the same cartridge (Meinertzhagen and Sorra, 2001). These are specialised intracellular connections that communicate the cytoplasm of two cells. In addition, there exist communication between lateral cartridges through monopolar cells L2 and L4. It has also been reported that there exists excitatory feedback from the lamina, monopolar cell L2 and amacrine cells, to the retina (Meinertzhagen and Sorra, 2001; Zheng et al., 2006, 2009). Lastly, the communication between the interneurons hosted in lamina cartridges and the medulla is bidirectional, all LMCs and tangential cell T1 transmit information to the medulla, whilst centrifugal cells C1 and C2 are responsible for capturing the feedback coming from medulla (Meinertzhagen and Sorra, 2001). The interconnection between retina and lamina is shown in Fig. 2.3.

Colour and polarized light vision

Each photoreceptor features a light-sensitive pigment Rhodopsin. The spectral sensitivity of the fly is thus determined by this pigment. It has been reported that six different types, rh1-rh6, of Rhodopsin are expressed in *Drosohpila's* retina (Salcedo et al., 1999). Which particular type of Rhodopsin is expressed depends on both the type of photoreceptor and the eye region.

Rhodopsin rh1 is expressed in the outer photoreceptors R1-R6, thus they are sensitive to blue/green (Hardie, 1985). Opposite to that, the outer photoreceptors R7/R8 feature either of

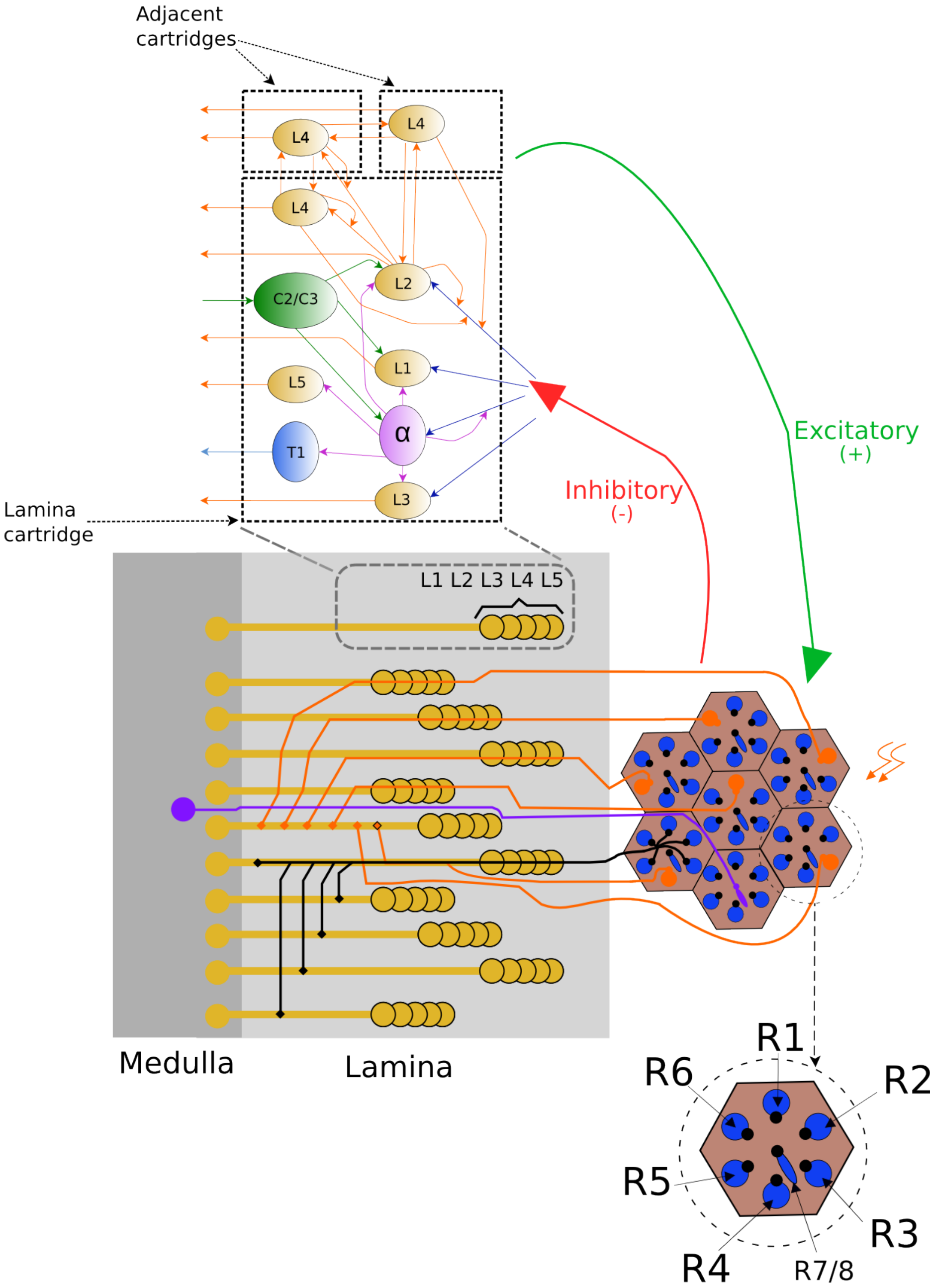

Fig. 2.3 *Drosophila's* Retina/Lamina connectome. This figure shows the Retina/Lamina interconnection and the Lamina network. The top part of the figure displays a synaptic signalling diagram that presents the information flow in the Lamina.Each Lamina cartridge is composed of Large monopolar (L), Centrifugal (C), Tangential (T) and Amacrine (α) cells. In the middle part of the figure, the neural superposition of the photoreceptors is shown. This part shows that photoreceptors with the same target in the lamina are located in neighboring ommatidia. The red and green arrows that connect the top with the middle part of the figure indicate that there is a bidirectional communication between Retina and Lamina. Finally, the bottom part of the figure shows in more detail the components of each ommatidium.

three different combinations rh3/rh5, rh3/rh3/ rh4/rh6, which are known as pale, yellow or DRA (dorsal rim area) ommatidia respectively (Wernet et al., 2003).

Regardless of the combination, R7 always has an UV sensitive pigment, i.e. rh3 or rh4, whereas R8 features a blue- or green- sensitive opsin, i.e. rh5 or r6 respectively. Moreover, it has been reported that there exist a 70/30 % ratio between 'yellow' and 'pale'. The stacked arrangement of R7/R8 is what makes it possible for colour and polarised light to be detected.

In fact DRA ommatidia, which has rh3 in both R7 and R8, are in charge of detecting the vector of polarised light(Hardie, 2012b; Wernet et al., 2003), which is known to be used by the fly to locate sun's position even when obscured by cloudy conditions (Labhart and Meyer, 1999) and other animals use the same capability for migration purposes (Homberg et al., 2011; Reppert et al., 2010).

2.3 The Phototransduction Cascade

In order for the fly to use the visual stimuli to make sense of the surrounding environment the perceived visual stimulation undergoes an energy conversion process that turns light into electrical signals. This process takes place in the retina. More especially in each microvilli belonging to the rhabdomere of each photoreceptor, and is called phototransduction cascade. This is mainly a biochemical process by which light energy is first amplified and then, after a series of chemical reactions where several different mechanisms and molecules are involved, it is converted into a membrane potential.

In *Drosophila* this process of turning light into electrical signals interpretable by the brain has been reported to, not only be highly sensitive, capable of reacting from a single photon hit but also still show dynamical adaptation under full sunlight. In addition to that, it overtakes in reaction speed, by one or two orders of magnitude, vertebrate rods when responding to single photon hits. Furthermore, it has been argued that *Drosophila's* phototransduction cascade is one of the fastest, if not the fastest, signalling cascades in the animal kingdom (Hardie and Postma, 2008a; Hardie, 2001).

In spite of the fact that phototransduction cascade has been studied intensely, there are still fine details which are not known (Hardie, 2012a). In the section, a brief explanation of the known main mechanisms that take place so the light can be turned into a membrane potential is outlined.

2.3.1 Activation of the Phototransduction Cascade

When a light passes through the rhabdomere the energy of the photons captured by individual microvillies, causes rhodopsin to be isomerised and as a result, metarhodopsin (M) is produced.

The production of metarhodopsin causes a second messenger, the G-protein, to be activated. G-protein activation results in guanosine diphosphate (GDP) to be exchanged with guanosine triphosphate (GTP), this exchange triggers a dissociation process of the G_α subunit from the G protein which leads to the activation of phospholipase C-β(PLCβ) an enzyme effector. This enzyme causes phosphatidylinositol 4,5-bisphosphate(PIP$_2$), a phospholipid, to hydrolyse into inositol 1,4,5-triphosphate (InsP$_3$) and diacyglicerol (DAG) which are two signalling molecules.

This hydrolisation process leads to the release of PUFA, poly unsaturated fatty acids. At this point, the highly permeable by calcium(Ca$^2+$) TRP (Transient Receptor Potential) and the non-selective cation TRP-like channels; both of which are light sensitive, open. The opening of these channels causes an influx of both sodium(Na$^+$) and magnesium(Mg$^2+$). This last process is responsible for the generation of the light-induced current (LIC) that depolarises the photoreceptor. It has been reported that the forward pathway of the phototransduction, from light absorption to opening of the first TRP channel takes about 20ms (Hardie, 2001). Also, there are two possible related mechanisms, positive feedback (Hardie, 1991) and 'all or none'(Hardie and Raghu, 2001b) excitation, regarding TRP channels that might help in achieving such fast responses.

2.3.2 Phototransduction cascade inactivation

In order to have high sensitivity to rapidly changing visual stimulation, both activation and deactivation mechanisms have to be fast. In *Drosophila* photoreceptors there are two main mechanisms that contribute to this process.

The first one is a re-isomerisation process from metarhodopsin to rhodopsin which occurs thanks to the absorption of red light which happens efficiently in *Drosophila's* since this contains pigments which are transparent to long wavelength light (Hardie, 2012a; Hardie and Raghu, 2001b).

The second has to do with the closure of TRP/TRPL channels. It has been shown that during the termination of the light into current process, Ca^{2+} provides negative feedback signals to TRP/TRPL channels to facilitate their closure (Hardie and Minke, 1994).It also has been suggested that metarhodopsin inactivation can be regulated by Ca^{2+}.

For a detailed explanation of all the phototransduction cascade in *Drosophila* the interested reader is referred to following reviews (Hardie and Postma, 2008a; Hardie, 2012a; Hardie and Raghu, 2001b; Minke and Cook, 2002; Montell, 2012).

2.3.3 Photoreceptor Membrane Potential

Any microvilli belonging to a rhabdomere of any photoreceptor is a candidate to be hit by a photon or beam of them and as a result, generates a voltage response. This process is known as *quantum bump* and it is believed to follow Poisson statistics.

There is a variable latency period between photon absorption and the moment in which the first TRP/TRPL channel opens (Hardie and Raghu, 2001b). Positive feedback amplification and negative feedback effects ensure that the bump itself rises and decays fast.

However consecutive bumps occur only after a refractory period of about 100-200ms (Scott et al., 1997). Depending on the light intensity contained in the visual stimulus, the superposition of all quantum bumps generate a macroscopic light response, that is known as light-induced current(LIC)(Hardie and Raghu, 2001b).

Ultimately the observed change in membrane potential is characterized not only by the kinetics and sensitivity of the phototransduction cascade but also by the electrical properties of the light-insensitive membrane. The LIC is actively filtered by the membrane, whose filtering properties are defined by voltage-sensitive K^+ channels. These include the *Shaker* K^+ and some variants of the non-inactivating K^+ channel (Niven et al., 2003b). In addition to these channels, the membrane hosts K^+ and Cl^- leak channels that help to maintain the resting membrane potential.

2.4 Experimental Methods

This section describes the experimental setup used to measure *in vivo* neural responses to naturalistic visual stimulation, from wild and histamine deficient hdc^{JK910} fruit flies.

The actual experiments from which the experimental data was collected were not done by the author of this thesis. The experiments and data gathered as the outcome were shared by a collaborator whose work and detailed explanation of the followed protocols in the experiments can be found in (Friederich, 2011; Friederich et al., 2016, 2012).

2.4.1 Electrophysiology

Preparation

During the actual experiments, the fly was placed in a copper conical holder. In order to minimise sources of measurement artifacts and following the protocol suggested in (Juusola and Hardie, 2001), the animal's thorax, proboscis, and right eye were fixed using beeswax. To obtain *in vivo* intracellular recordings a microelectrode was introduced in the left eye's dorsal cornea, which was first pierced to produce a hole with of about 6-10 ommatidia span. In order to prevent the eye from drying out the hole was sealed with a drop of Vaseline.

In addition to the intracellular recordings, extracellular electroretinograms (ERG) were also recorded at the eye's dorsal surface. For both types of measurements intra- and extracellular, a blunt reference electrode was placed close to the ocelli, in Drosophila's head capsule. Also following (Juusola and Hardie, 2001) a Peltier element was used to keep a constant temperature of 19°C.

A horizontal laser puller (Sutter Instrument, P-2000), was used to pull the 0.6mm-recording and 1mm-reference electrodes, from the glass tubings. Before inserting them into the tissue, the tips of the electrodes were broken blunt. The recording electrodes had an in-tissue average resistance of 100-180MΩ. Previous studies(Tamara, 2009) have reported that this type of electrodes have widths that vary from 0.23 to 0.35 μm once they have penetrated the photoreceptor, and thus are suited to recording from *Drosophila* photoreceptors R1-R6 that are about 4μm in diameter.

The electrodes used to measure the ERG were broken to increase the contact, thus conductance in the eye's surface. Following the proposed protocol in (Juusola and Hardie, 2001), the ringer's solution was made up 120mM NaCl, 5mM KCl, 10mM TES, 1.5mM CaCl2, 4mM MgCl2, and 30mM sucrose, also the electrodes used for both intracellular and extracellular recordings were filled with 3 M Cl. A micromanipulator(Mertzhauser, PM10) and stereomicroscope(Nikon SMZ 1B) were used to position the recording electrodes.

The developed rig is capable of delivering parallel light stimulation,and electrical injections in the form of current or voltage while recording their electrophysiological responses.

A digital-to-analogue (A/D) converter board (NI, PCI 6713) controlled by a desktop computer(Pentium 4HT, 3.2GHz, 2GB RAM) was used to deliver stimulus waveforms to the animals. The same workstation in conjunction with a analogue-to-digital(A/D) converter board (NI, PCI M-IO 16E4) were used to captured the externally measured signals from the flies. A -10/+10V reference voltage range, resolution of 12 bits and a sampling rate of $\geq$ 2KHz were used in both A/D and D/A boards. A 500Hz cut-off frequency, antialising analogue low-pass filter(KEMO Limited, VBF/23 elliptic filter) was used to prefilter the signals before they were sampled. The interfacing boards were controlled using a custom-developed toolbox (Biosyst, M. Juusola; MATDAQ, H.P.C. Robinson) for the MATLAB environment(Mathworks, version R 7.14) Also, current injection commands and electrophysiological responses were amplified by a single, high-impedance head-stage, switched-clamp amplifier (NPI Electronic, SEC-10L). This setup allows good quality current and voltage photoreceptor-intracellular monitoring and recording capabilities, during current or light stimulation(Juusola, 1994). A switched clamp mode with a selected frequency of 30kHz was used for all voltage recordings and injections of current. The experimental rig had a mechanism to keep the fly's body temperature constant at either 19°C or 25°C. This mechanism was built using a Peltier-element and bimetal sensor based controller. This type of controller prevents artifacts when recording experimental data (Juusola and Hardie, 2001).

2.4.2 Stimulus design

In this thesis, extra- and intra- cellular data was collected just from the R1-R6 outer photoreceptors.

For intracellular recordings, target photoreceptors were picked by monitoring the remotely controlled micromanipulator which followed a blind-scoping strategy along the animal's retina and stopped when a photoreceptor was found. A voltage drop in the range of 50 to 70 mV was an indication of a successful photoreceptor penetration. From all successful photoreceptor penetrations, the following scouting strategy was used to decide whether or not data from that photoreceptor were collected.

First, the photoreceptor responses to a sequence of 10ms-width light pulses, with a 200ms interval between each pulse were collected. Then the photoreceptor type was characterised by analysing the response shape and magnitude. Finally, recordings that featured a peak response greater than 50mV were kept. For the selected responses up to the previously discussed point, an assessment of the light sensitivity of each photoreceptor was performed by using its voltage response to logarithmically intensified light flashes. The normalised $V/\log_{10}(I)$ curves were used to characterise the photoreceptor sensitivity, this process was done by comparing the voltage responses against a sequence of intensity pulses (Horridge et al., 1976). Furthermore, an outlier spotting strategy was implemented by adjusting the light source using the information provided by the $V/\log_{10}(I)$ curves. In the end cells with abnormal $V/\log_{10}(I)$ curves were discarded.

In the case of ERG, extracellular recordings were mainly used to monitor the response in the lamina for blind flies. As described above, the animal was fixed to the holder then a blunt recording electrode was subtly placed so it would be in contact with the retina's surface, in the contact point a fly ringer was used as a moisturiser to improve the signal conductance. The electrodes used had a resistance of less than 5MΩ. In this type of experiments the centre of the retina was stimulated with very bright pulses of 700ms, of pulse width, produced using a wild field LED. A 5-seconds dark period in between light pulses was used. On average 25 pulses were collected from each animal.

Stimuli design for intracellular recordings

In *Drosophila’s* photoreceptors, a 60mV range is enough to represent visual stimulation that can vary from single photons to over 10^6-fold(Juusola and Hardie, 2001). The photoreceptor’s ability to respond to this very broad range of stimuli has been suggested to come from the different adaptation mechanisms that photoreceptors use to adjust their sensitivity to different light conditions (Juusola and Hardie, 2001). Previous studies have one of the following types of stimulation

- Light pulses/steps(Dubs, 1981; French et al., 1993; Laughlin, 1989a; Laughlin and Hardie, 1978; Weckström, 1989). This type of stimulation is good for characterising fast adaptation mechanisms, however, little or none can be learned as to how sensory neurones adjust their sensitivity to continuous stimulus variations.

- Pseudoramdom Gaussian Noise (GWN) (French, 1979; French et al., 1993; Juusola et al., 1995a). The adaptive-filtering properties of photoreceptors have been studied further with this type of stimuli, however photoreceptor’s response to this type of stimulation is linearised by its inherent constant statistical properties (Van Hateren, 1997).

- Natural time-series of intensities (NTSI) (Van Hateren, 1997). This type of stimuli can have either continuously varying local statistics (Brinkworth et al., 2008; Juusola and de Polavieja, 2003; Van Hateren, 1997; Van Hateren and Snippe, 2001) or constant local statistics(Friederich et al., 2016). In either case, photorecetpors responses are not linearised as with GWN (Simoncelli and Olshausen, 2001; Van Hateren, 1997). NTSI with constant local statistics was the type of stimulation used in this thesis. In order to understand how information about visual invariances, i.e. same visual stimulus at different luminance levels, is processed by the early visual system, a NTSI with constant local statistics stimulation was used since having continuously varying local statistics makes it more challenging.

The flies were presented the same NTSI temporal stimuli over different light intensity levels. The same rig as in (Friederich et al., 2016) was used. It consists mainly of a source of two-converging paths of light controlled by a PC, Fig. 2.4. Linear relationship between the NTSI light pattern stored in the computer and the actual light pattern delivered to the flies was assured by using a LED driver with light feedback (Cairn Research, optoLED) who operated one LED (Seoul, Z-Power LED P4, white 240ml) on each path. Also 5 different

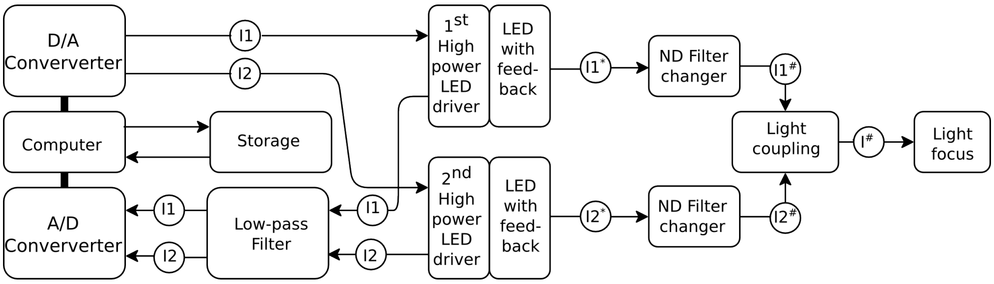

Fig. 2.4 Experimental Rig

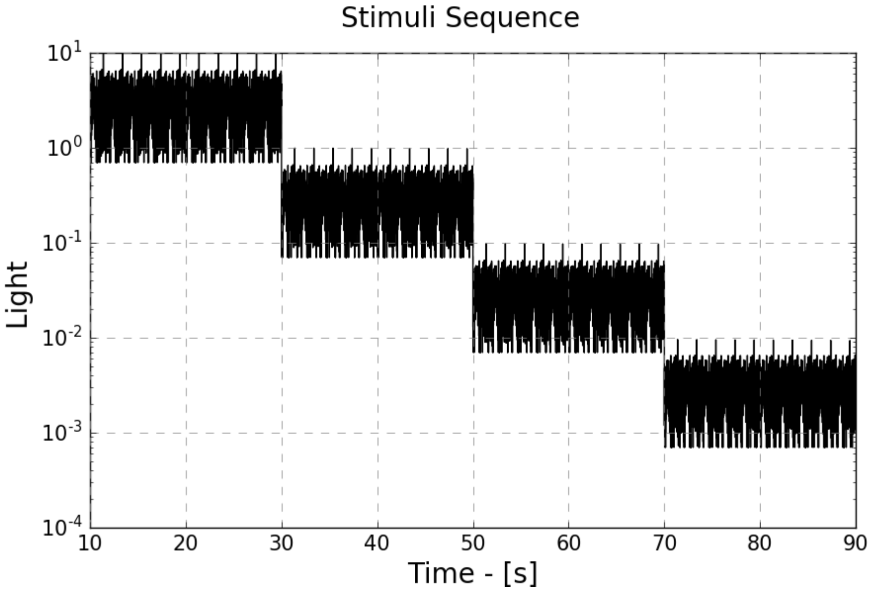

Fig. 2.5 Natural time series of intensities (NTSI). The same pattern with different mean light intensity level.

light intensity levels labelled as L0-L4, L0 the being the brightest and L4 the darkest, were generated using Natural density filters (Kodak Wratten, ND gel filters). The two filters were configured equally so they had produced the same response for a given reference signal. The rig was configured so the paths were active in an alternating fashion, i.e. just one path delivered light stimulation to the fly at the time. This configuration allowed for having sharp(step) changes of light since the configuration of the filter in the inactive path could be changed in real time.

The actual reference signal is shown in Fig. 2.5. In order to resemble what the animals would encounter in their natural habitat, the flies were stimulated with a selection of NTSI with an average power spectrum $S(f) = \frac{1}{f}$ which were taken from (Van Hateren, 1997).

This reference signal stimulates the animal across the entire environmental range of light intensities. The selected stimulus shown in Fig. 2.5 is the result of the concatenation of the selected reference signal with different mean light intensity levels.

2.5 Electrophysiological *in vivo* recordings from photoreceptors of wild and histamine deficient fruit flies

In this thesis, two different types of fruit flies were used. The wild-type (Canton S) flies which were raised in acrylic vials kept at 18°C, in a 12-12 dark-light cycle and having as food source a mixture of dried yeast molasses sugar and cornmeal. The histamine deficient type, i.e. blind flies (hdc$^{\mathrm{JK910}}$) donated from Julius-Maximilians-Universität Würzburg, Germany.

It is well known that lamina interneurones contribute to the observed response of *Drosophila's* outer photoreceptors for a given visual stimuli. By using different *Drosophila's* transgenic mutants, previous studies have shown that (Dau et al., 2016; Hu et al., 2015; Nikolaev et al., 2009; Zheng et al., 2006, 2009) the modulation from lamina plays an important role in preventing the photoreceptors's response to saturate and in increasing the SNR.

In this thesis histamine deficient hdc$^{\mathrm{JK910}}$ *Drosophila* alleles were used to explore the contribution of the network of lamina's interneurones in modulating the response of outer photoreceptors and then to develop empirical models that explicitly reflect this modulation. In hdc$^{\mathrm{JK910}}$ mutant flies, because of their histamine deficiency, the communication between the retina and the lamina does not occur (Hardie, 1987, 1989; Sarthy, 1991), i.e. these fruit flies have been shown through behavioural tests, to be blind. Thus, photoreceptor's responses contain no modulation from lamina.

Mutation can have secondary effects. Because of that, a rescue procedure was carried out in hdc$^{\mathrm{JK910}}$ mutant flies to check that the electrophysiological measuremets of interest were not affected by any unknown effect. The rescue procedure consisted in of a histamine feeding episode, which was done two days before the actual experiment took place. This rescue procedure of feeding histamine was based on previous works (Dau et al., 2016; Friederich et al., 2016) which reported that hdc$^{\mathrm{JK910}}$ can recycle histamine from media if is available.

During the experiments, collected data from both, intra- and extra- cellular experiments suggested that the rescuing protocol was successful.

For the extracellular case, ERG responses to light pulses were collected from wild, mutant and rescued flies. The results depicted in Fig. 2.6 (a) show that recorded data from wild and rescued flies feature a pronounced transient at the moment of the step, however, this same transient is absent in the case of the non-rescued mutant flies.

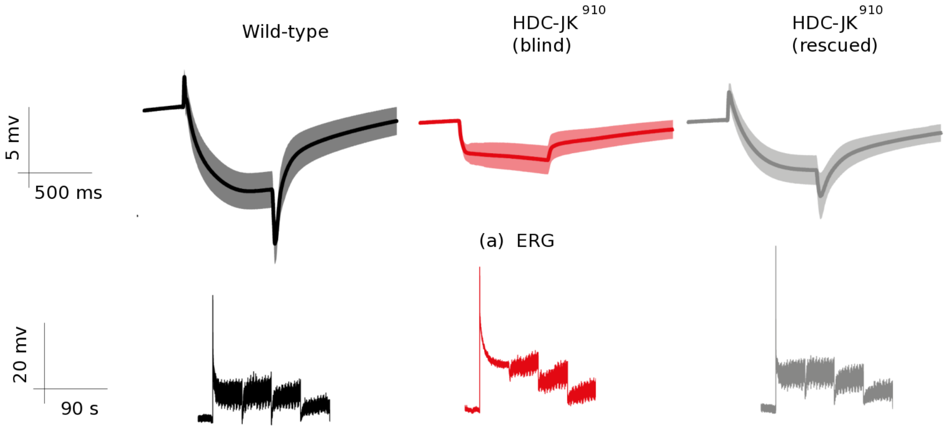

(a) ERG

(b) Voltate Response

Fig. 2.6 ERG and Voltage Response of wild-type, blind and rescue flies. (a) Electro-Retinogram (ERG). (b) *in-vivo* intracellular voltage responses

The successful outcome of the recovery procedure observed when using extracellular recordings was confirmed by the intracellular one, the results are shown in Fig. 2.6 (b). On the one hand, wild and the mutant rescued flies shared similar responses to NTSI stimulation over the entire range of different light intensity levels. On the other hand, the collected data from flies with missing synaptic activity between retina and lamina, showed a clear difference in the response across all light intensity levels, with more emphasis for in L0, the brightest light intensity level. As suggested from previous works(Dau et al., 2016), this could be the result of saturation caused by the lack of modulation coming from lamina.

Finally Fig. 2.7 (a) and Fig. 2.7 (b) show in more detail the *in vivo* intracellular recordings of the wild-type and hdc^{JK910} flies when stimulated using the NTSI presented in Fig. 2.5. These three data sets were used to develop all the models presented in this thesis.

2.6 Discussion

The first part of the Chapter provided an overview of the early visual system of *Drosophila*, focusing on the R1-R6 photoreceptors and their post-synaptic partners. The biophysical mechanisms that photoreceptors use to sample light information were also reviewed.

The second part of the Chapter introduced the materials and methods to generate the experimental data used to develop the models presented in subsequent chapters. The experimental stimuli and the corresponding photoreceptor responses measured *in vivo* were also

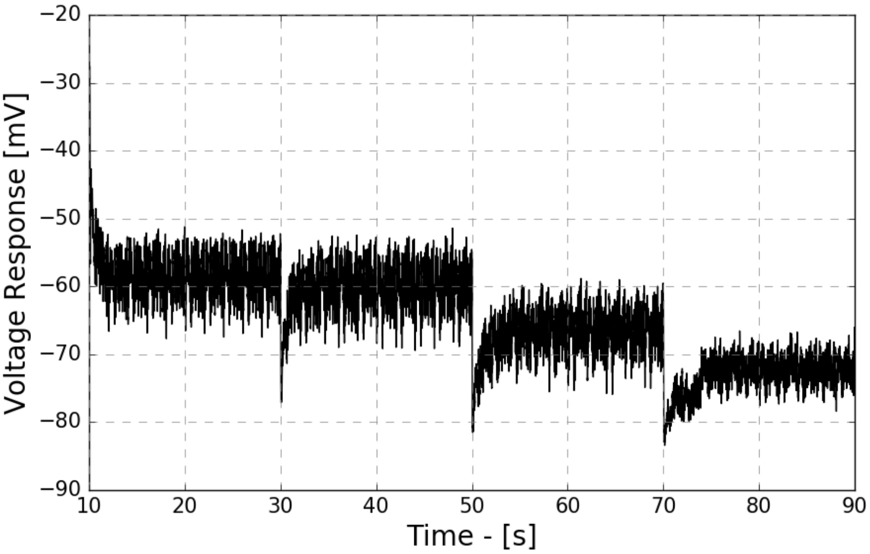

(a)

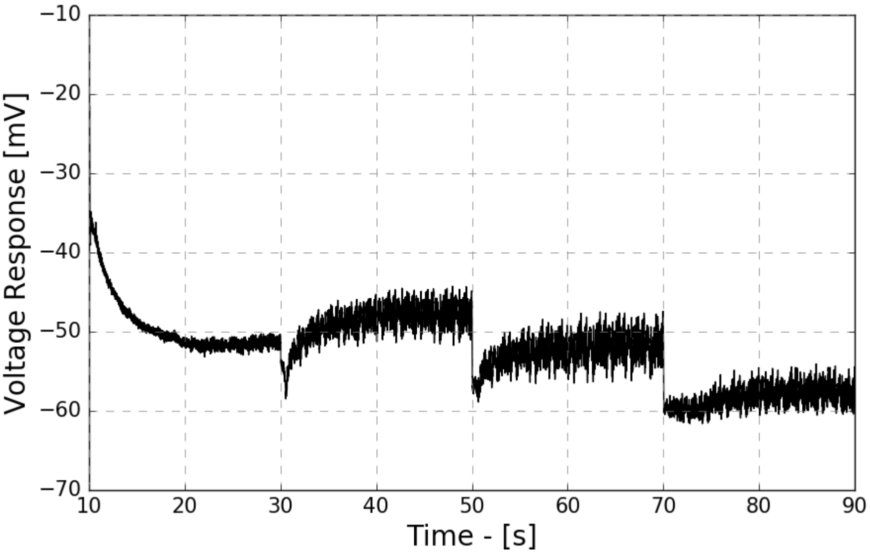

(b)

Fig. 2.7 Voltage response of outer, PR1-PR6, *Drosophila's* photorecetpors. (a) Wild-type fly. (b) hdc$^{\mathrm{JK910}}$ blind fly.

described and illustrated in detail, highlighting the differences between responses measured in wild-type and histamine mutant photoreceptors.

It is important to mention that just one data set from each type of fly, one for the wild and one for the histamine deficient fly, were provided. Thus, these datasets were used for derivation and validation of the model models in this thesis which is a limitation of this work.

Chapter 3

Nonlinear System Identification For Neuroscience

3.1 Introduction

In control engineering, system identification is commonly used to derive mathematical models of dynamical systems from experimental measurements.

System identification consists of the following steps (Ljung, 2009). The first step is data collection. The main goal of this step is to design the experiment that will be conducted in order to collect relevant input/output data. Normally previous knowledge of the system is taken into account to design the experiment. The key factors that need to be taken into account when designing and implementing the experimental data acquisition include the number of system inputs and outputs, signal bandwidth, sampling-rates and signal processing strategies for noise removal and de-trending (Billings, 2013; Lennart, 1999; Marmarelis, 2004). Deriving the model from data involves choosing a model class, defining a set of candidate model structures, selecting the correct model structure, estimating the model parameters and validating the model.

System identification has been successfully applied in different disciplines(Billings, 2013) including space weather (Solares et al., 2016), medical imaging(Vidal-Rosas et al., 2014), synthetic biology (Krishnanathan et al., 2012), economy (Aguirre and Aguirre, 2002), etc.

A particular research area in which system identification has had a big impact is systems/computational neuroscience. Previous studies (Friederich et al., 2016; Kim et al., 2011) have confirmed the feasibility and usefulness of using this approach to model and understand the underlying principles behind the computations performed by the brain of different organisms.

The purpose of this chapter is to introduce the main modelling tools used throughout this thesis, particularly the NARMAX method.

The outline of this chapter is as follows. Section 2 introduces the main concepts of system identification and surveys briefly the main methods used in Neuroscience to derive empirical mathematical models using system identification methods. In section 3 the main concepts and implementation details of NARMAX method are discussed. In the same section, the spectral analysis of the polynomial expansion is explained. Lastly, in section 4 a brief summary of the key aspects of the NARMAX method are outlined.

3.2 System Identification in Neuroscience

System identification in neuroscience presents some challenges. The first challenge is to decide whether the system can be modelled by a linear or nonlinear mathematical model. To this end, there are tests that can help assessing linearity in a system (Berg et al., 2012).If the system can be modelled by a linear model, then there is a vast and mature set of techniques that can be applied, a review of this techniques can be found in (Ljung, 2009, 2010). However, it is known that dynamical processes encountered in neuroscience are nonlinear and thus demand system identification approaches (Marmarelis, 2004). Although the number of techniques for modelling nonlinear systems is not as rich as in the case of linear systems, there exist some options. A brief summary of some of the main strategies will be presented in this chapter. A more in-depth review of these and more strategies can be found in (Marmarelis, 2004) and (Billings, 2013). NARMAX (Billings, 2013; Chen and Billings, 1989a), which is arguably the most comprehensive and effective nonlinear system identification approach available, was adopted and used in this work to develop models of the fly photoreceptor using *in-vivo* experimental recordings of photoreceptor responses to multi-level naturalistic stimuli. Provided that it has been decided to model the system using nonlinear models obtained with NARMAX method then, the second challenge that needs to be addressed is structure selection and parameter estimation. Depending on the level of nonlinearity and data available, the structure can be chosen to be polynomial (Chen and Billings, 1989a), rational (Chen and Billings, 1989a; Zhu and Billings, 1994), wavelet-based (Billings and Coca, 1999), based on radial basis functions (Chen et al., 1990) or hybrid models (Billings and Wei, 2005). Once a structure family has been selected, a suitable approach to estimate the parameters for that expansion is needed. In the case of the polynomial expansion, the problem can be formulated as an optimization problem that is linear in the parameters, so very efficient techniques such as (Chen et al., 1989, 2009) can be used to estimate the parameters. In the case where the expansion is not linear in the parameters, such as radial basis function networks with then approaches based on heuristics (González et al., 2003; Guerra and Coelho, 2008) can be used.

The last step in the process of system identification regardless of the selected method is model validation. In this stage, the model performance is assessed and is either accepted or rejected. In the latter case then a new iteration of the identification process is performed. An in-depth review of all the options is outside the scope of this work but reviews on the topic can be found in (Arlot et al., 2010; Billings et al., 2001; Marmarelis, 2004). Also, model validation for the NARMAX method is explained below.

In the remaining of this section a brief account of the most popular system identification methods used in Neuroscience is given.

3.2.1 Volterra and Wiener Series Models

Volterra/Wiener series is one of the most used system identification techniques for nonlinear systems in neurophysiology. The Volterra series (Volterra, 2005) were introduced to characterise nonlinear systems in a nonlinear fashion.

The Volterra series is defined by

$$y(t) = \sum_{n=0}^{\infty} \int_{\Omega} \cdots \int h_n(\tau_1, \tau_2, ..., \tau_n) \prod_{i=1}^{n} u(t - \tau_i) d\tau_i \tag{3.1}$$

where $u(t)$ and $y(t)$ are the input and output time variables of the system and $h(\cdot)$ are the Volterra kernels.

A practical method to solve the problem of estimating the kernels of the functional series Equation 3.1 was proposed by Norbert Wiener, who used the Gramm-Schmidt orthogonalisation technique to uncouple the Volterra kernels. The resulting series is given by the following equation

$$y(t) = \sum_{n=0}^{\infty} G_n \left[\tilde{h}_n(\tau_1, \tau_2, ..., \tau_n); u(t'), t' \leq t\right] \tag{3.2}$$

In this series, G_n represents the functionals that, for Gaussian white noise stimulus are orthogonal.

A very popular way of empirically obtaining the Wiener kernels, $\tilde{h}_n(\cdot)$ was proposed by Lee and Schetzen (1965). In the proposed cross-correlation method time delay white

Gaussian noise stimulus with P power spectral density is multidimensionally correlated with the system's output to yield

$$\tilde{h}_n(\tau_1, \tau_2, ..., \tau_n) = \frac{1}{n!P^n} E\left[y(t)u(t-\tau_1)u(t-\tau_2), \cdots, u(t-\tau_n)\right] \tag{3.3}$$

where the expected value is denoted as $E[\cdot]$. Although this method has been applied successfully in neuroscience (Sakai, 1992) and (Marmarelis, 2004), this approach has a number of drawbacks. The two main drawbacks are the following: the inability to estimate the diagonal values ($\tau_i = \tau_j, i = j$) of higher order kernels and the experimental generation of Gaussian white noise input (Palm, 1979).

To address this problem, some studies (French, 1976; French and Butz, 1973) have proposed a method to calculate the Volterra Kernels in the frequency domain, in doing so the correlations were replaced by complex multiplications. This approach is faster than the conventional correlation-based and does not require the generation of white noise stimuli. However the method relies on accurate estimates of power and cross power spectra, of the input and input and output respectively.

The most common approach to estimating Volterra and Wiener kernels is through linear regression. In order to apply such techniques, the input/output dataset, i.e. $u(t)$ and $y(t)$, need to be discrete sequences which are normally uniformly sampled. Thus the equation for the Volterra series has summations instead of integrals

$$y(t) = h_0 + \sum_{n=1}^{\infty} \sum_{j_1} \cdots \sum_{j_n} h_n(\tau_{j_1}, \tau_{j_2}, ..., \tau_{j_n}) \prod_{i=1}^{n} u(t-\tau_{j_i}) \tag{3.4}$$

Note that in the above equation t denotes discrete time points, i.e. $t = t_1, t_2, t_3, ...$ Also, the previous equation is linear in the kernel values. Furthermore, if the number of kernels is finite then the Equation 3.4 can be written in matrix form as

$$\mathbf{y} = \mathbf{P}\theta \tag{3.5}$$

where the system's output is represented by $\mathbf{y}$, the matrix $\mathbf{P}$ denotes the regression matrix, which contains the delayed version of the input and its cross products and θ represents the vector of unknown discrete kernel values that need to be estimated. In actual experiments, the relationship between the real, $y(t)$ and the measured, $z(t)$, system's output is given by $z(t) = y(t) + e(t)$ where $e(t)$ denotes an uncorrelated sequence, noise, that contaminates the real output. The kernels are obtained as the solution to the following linear optimisation problem

$$\hat{\theta} = \underset{\theta}{\arg\min}\ \|\mathbf{z} - \mathbf{P}\theta\|_2^2 \tag{3.6}$$

This approach has the advantage that all kernels are estimated in parallel, thus they don't need to be uncoupled which has as a consequence that the need for white noise stimulation is no longer necessary and also the estimation of diagonal values in high order kernels is not an issue anymore.

An orthogonal algorithm for estimating Volterra kernels $h_n(\tau_1, \cdots, \tau_n), n = 1, \cdots, R$ where R is the order of nonlinearity, directly from data was proposed by Korenberg et al. (1988b).

This approach involves orthogonalizing Equation 3.4 over the actual inputs. The main advantages are that the inputs can be arbitrary and that the algorithm does not require long data sets. This algorithm has been reported to be fast and easy to initialise (Korenberg and Paarmann, 1989). One drawback is that the kernels are quite noisy (Marmarelis, 1993).

In order to address the issue of the noisy kernels a study (Marmarelis, 1993) was conducted, where the input is filtered by a set of orthonormal Laguerre functions given by the filter bank (Ogura, 1985)

$$b_n(x) = \alpha^{\frac{x-r}{2}}(1-\alpha)^{\frac{1}{2}} \sum_{n=0}^{r} \binom{x}{n} \binom{r}{n} \alpha^{r-n}(1-\alpha)^n, r = 0, 1, 2, \cdots, R \tag{3.7}$$

where the n^{th} order Laguerre filter is denoted by $b_n(x)$.The filter has an exponential decay regulated by the $\alpha, \in [0,1]$ parameter and is defined discretely at $x = 0, 1, \cdots, X$ discrete interval. With this definition and using a sampling time T_s, the v_n filter bank outputs are obtained by the discrete convolution

$$v_n(x) = T_s \sum_{x=0}^{X-1} b_n u(t-x) \tag{3.8}$$

Using this previous definition, the Laguerre-Volterra series model is defined as

$$y(t) = h_0 + \sum_{n=1}^{R} \sum_{j_1=1}^{L}, \cdots, \sum_{j_n=1}^{L} \tilde{h}_n(j_1, j_2, \cdots, j_n) \prod_{i=1}^{n} v_{j_i}(t) \tag{3.9}$$

So each Volterra kernel is given by

$$y(t) = h_n(\tau_1, \cdots, \tau_n) = \sum_{j_1=1}^{L}, \cdots, \sum_{j_n=1}^{L} \tilde{h}_n(j_1, j_2, \cdots, j_n) \prod_{i=1}^{n} b_{j_i}(\tau_i) \tag{3.10}$$

where L denotes the number of applied basis functions. The Laguerre-Volterra nonlinear model is composed of two stages. The first stage is a linear filter bank that uses the Laguerre basis functions as filters. The outputs of this filter bank are the inputs of the second stage, which is a static nonlinearity. Furthermore, since the model Equation 3.9 is linear in its parameters, it is possible to cast it into a linear regression model, i.e. Equation 3.5.

Using the Laguerre-Volterra series as a model for nonlinear systems has the advantages of being relatively easy to obtain, once it has been completely defined; and providing truncated and smooth kernel estimates (Marmarelis, 1997). However, since the number of basis functions L and the exponential decay parameter α specified and are not linearly related. It is difficult to determine them. In addition, Laguerre-Volterra methods and similar techniques can lead to misinterpretation of the order of nonlinearity of a system (Korenberg and Hunter, 1996). And lastly, it has also been pointed out (Billings, 1980) that these type of models are unsuitable for systems with strong nonlinear behaviour since the number of coefficients increases exponentially with the nonlinear order of the system.

3.2.2 Block Structured Models

Another common approach to modelling systems in Neuroscience is through block structured models. Their popularity is due to their relative simplicity and perhaps even more so, for their potential for physiological interpretations. In this approach, the model is made up one or more blocks each of which perform a linear or a static nonlinear transformation. The blocks(L), that yield an output $y(t)$ as a result of performing a dynamic linear transformation in its input $u(t)$ are described by the following convolution integral

$$y(t) = \int h(t)u(t-\tau)d\tau \tag{3.11}$$

where $h(t)$ is the impulse response of the linear filter. If rather than being linearly filtered the input of a block is processed by a static nonlinearity (N) then the relationship between the temporal input $u(t)$ and the output $y(t)$ is given by

$$y(t) = f_N(u(t)) \tag{3.12}$$

where f_N is a nonlinear mapping which can take the form of a polynomial function, exponential function or some other parametric or nonparametric nonlinearity (Pearson, 1995).

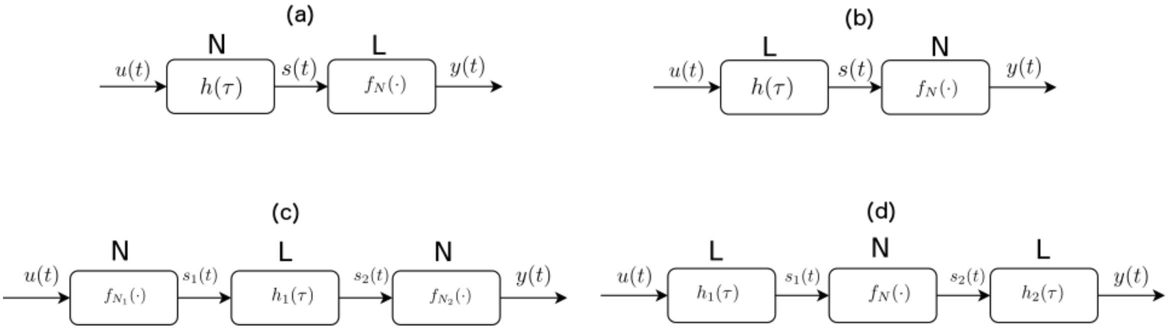

Fig. 3.1 Serial Cascade Block Structured Models. (a) Wiener configuration. (b) Hammerstein configuration, (c) 'Sandwich' L-N-L configuration. (d) 'Sandwich' N-L-N configuration.

According to their configuration, block structured models can be classified in serial cascade, parallel cascade models, and neural models.

In serial cascade models the each block's output is connected to the next block's input, and the input of the first block of the model is the recorded input, whilst the last block's output is the predicted model response. The two most used common models that follow this configuration are the Hammerstein and Wiener models. Both share the same topology, two blocks connected in cascade, however, the Hammerstein, Figure 3.1(a), features an N-L configuration whilst the Wiener, Figure 3.1(b), is an inverted version, i.e. L-N. The estimation of these two models is normally performed in an iterative process where the values of the parameters for the L and N blocks are refined in each iteration, details of the estimation procedures can be found in (Hunter and Korenberg, 1986) and (Giri and Bai, 2010). These type of models have been used to characterise early visual systems of organisms (Ahrens et al., 2008; Gollisch and Meister, 2008; Hunter and Korenberg, 1986).

An extension of the Hammerstein and Wiener models are the so-called 'sandwich' models, where rather than having just two blocks, the system is modelled by either L-N-L, Figure 3.1(c), or N-L-N, Figure 3.1(d), structures. The estimation of the L-N-L models is normally carried out in a two-stage process. In the first stage a linear subsystem is identified and in the second stage a procedure to obtain a Wiener model is used, some examples of this estimation process and application of L-N-L models can be found in (Korenberg and Hunter, 1986). N-L-N models have also been used successfully in neuroscience (French et al., 1993; Juusola et al., 1995b; Niven et al., 2003a). In general, these 'sandwich' models are more flexible than either the Hammerstein or Wiener models. However, issues such as structure detection, access to intermediate signals and nonlinearity in the parameters, which prevents using least squares optimisation techniques to solve the estimation problem, have to be taken into account when using these type of models. Some authors Kibangou and Favier (2010); Korenberg and Hunter (1996); Marmarelis (2004) have studied the relationship between Volterra kernels and cascade systems and have, as a result, provided that the kernels are available, some suggestions regarding the topology of the cascade model can be made.

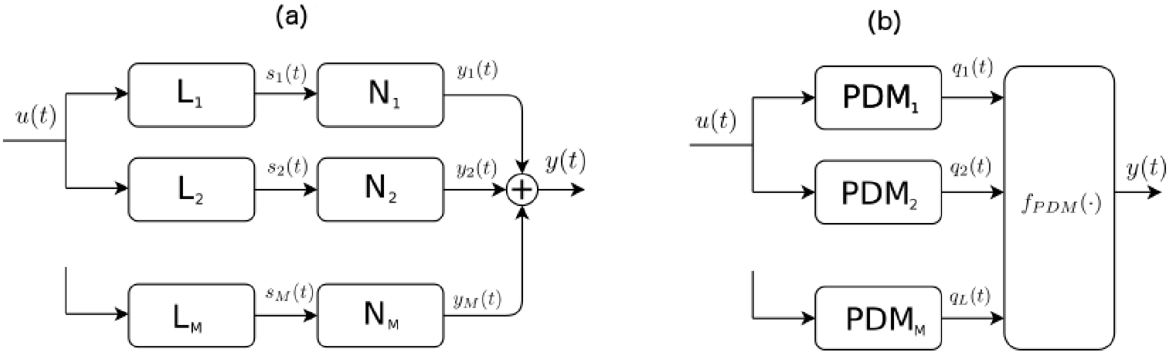

Fig. 3.2 Parallel Cascade and Neural Block Models. (a) Parallel cascade block model. (b) Neural mode model.

In a parallel cascade scenario, Figure 3.2(a) parallel cascade model with M parallel Wiener cascades, rather than having all the blocks one after the other, which means each block has a unique input, in this case, some blocks share the same input which comes from the previous processing stage. It has been shown (Korenberg, 1991), that parallel L-N cascade models can approximate any Volterra or Wiener series to an arbitrary accuracy. These models are defined as

$$s_i(t) = \int h_i(\tau)u(t-\tau)d\tau y_i(t) = \sum_j \alpha_{i,j} s_i^j(t) \tag{3.13}$$

where, as a result of filtering the $u(t)$ input to the system, the previous equations produce the i^{th} output signal $y_i(t)$, and the total predicted output of the model is given by $y(t)$ which is composed of the sum of all $y_i(t), i = 1, \cdots, M$ partial outputs.

Because of its robustness against fitting noise, parallel cascade models have been used to indirectly estimate Volterra kernels (Korenberg, 1991; Korenberg and Hunter, 1996). Parallel cascade models have been shown to be more robust against fitting noise.

Neural mode models, Figure 3.2(b), were introduced in (Marmarelis, 1993, 1997). These models are a block model that builds upon a Laguerre-Volterra series model. In this approach, the output $y(t)$ is given by the quadratic form

$$y(t) = \mathbf{v}^T(t)\mathbf{C}\mathbf{t} \tag{3.14}$$

where $\mathbf{v} = [1, v_1, ..., v_L(t)]$ is the augmented vector of the filter filter bank Equation 3.8, **C** is a symmetric matrix which has the values of zeroth, first and second order kernels.

The symmetric matrix **C** is decomposed as $\mathbf{C} = \mathbf{Q}^T\Lambda\mathbf{Q}$ where the i^{th} eigenvalue is contained in $\Lambda = diag\{\lambda_1, \cdots, \lambda_L\}$. Also the vector $\mathbf{q}(t) = \left[q_1(t), \cdots, q_L(t)\right]$ corresponding to the i^{th} eigenvalue is defined as

$$\mathbf{q}(t) = \mathbf{Q}\mathbf{v}(t) \tag{3.15}$$

where $\mathbf{Q} = [\mathbf{l}_1, \cdots, \mathbf{l}_L]$ is the eigenvector-matrix that corresponds to Λ. The relative contribution to the final filter output, of each individual filter's output, $\|q_i(t)\|^2$ is quantified by each eigenvalue in Λ. Thus, the i^{th} principal dynamic mode (*PDM$_i$*) is given by,

$$PDM_i(x) = \mathbf{l}_i\mathbf{b}(x) \tag{3.16}$$

where $b(x) = [b_1(x), \cdots, b_L(x)]$ is a vector containing the Laguerre filters described by Equation 3.7. Finally the model predicted output $y(t)$ is given by $y(t) = f_{PDM}(\mathbf{q}(t))$, where f_{PDM} represents a static nonlinearity with several inputs. According to (Marmarelis, 2004) a parsimonious neural mode model is achieved by selecting only the PDMs that have a significant contribution to the model output, i.e. $|\lambda_i| > 5\%$, By selecting the PDMs in this way the dimensionality of the model is reduced and the robustness is increased. Despite of the advantages that PDM models offer, since they are build upon an existing Laguerre-Volterra series model, thus all the difficulties regarding the identification of such models are inherited.

3.2.3 Gray Box Models

System identification models can be classified, in terms of the amount of prior knowledge of the system that is incorporated into it, into white, gray and black box Nelles (2013); Sjöberg et al. (1995). With white being the type that incorporates the most prior knowledge into the model, this implies that the underlying biophysical principles that govern the system's behaviour are known and well understood. A good example of this type of models in the field of neuroscience is biophysical models. Black models are on the other end of the spectrum, where very little to none is assumed about the nature of the system and the model is obtained mainly by data-driven approaches that involve collecting input/output data from the system.

Gray box models assume partial knowledge of the theoretical structure of the model, obtained from either the underlying known system's governing principles, known dynamical behaviour from previous experiments or previous models(Van Hateren and Snippe, 2001). And require the identification of the unknown parts from data.

A more granular classification of gray models has been proposed in (Sjöberg et al., 1995). Where the gray models are further divided into physical and semi-physical gray box models.

Using this new subclassification, a physical gray box model is obtained by fitting a defined number of parameters obtained from experimental data in a predefined set of equations that describe the system and have physical grounds. The selected structure is a crucial step in these type of models which plays an important role in the performance of the model.

In contrast to the physical models, where the governing equations or structure of the model is defined by physical principles which are thought to be part of the model, in the semi-physical models, the prior knowledge of the system is used to suggest particular linear or nonlinear combinations of the collected data either from experiments or simulations. After preprocessing the collected signals using the suggestions made taking into account the previous knowledge, the newly generated signals are used to estimate a black-box model of the system.

Because it is possible to implement and test hypothetical models using either physical or semi-physical gray box models, both are commonly applied as a strategy to model single neurons or networks of them. Regarding the visual system, some relevant works include (Brinkworth et al., 2008; Hateren, 1992; Laughlin, 1989b; Pece et al., 1990; Pumir et al., 2008; van Hateren and Snippe, 2001)

3.3 The NARMAX Method

The NARMAX (Nonlinear AutoRegressive Moving Average with eXogenous inputs) model (Billings and Leontaritis, 1981) is a nonlinear extension to the linear ARMAX model and is given by (Billings, 2013)

$$\begin{aligned} y(t) = F[&y(t-1), y(t-2), \cdots, y(t-n_y), \\ &u(t-d), u(t-d-1), \cdots, u(t-d-n_u), \\ &e(t-1), u(t-2), \cdots, e(t-n_e)] + e(t) \end{aligned} \tag{3.17}$$

where the input, output and noise sequences are given by $u(t)$, $y(t)$ and $e(t)$ respectively, also n_u,n_y and n_e represent the maximum lags for input them. $F[\cdot]$ is a nonlinear function, known as the expansion within the NARMAX methodology and d is a time delay which in most cases is set to $d = 1$.

It has been shown that most of the system identification models discussed in the previous sections, including Volterra, Wiener, Hammerstein, block-structured and several neural network architectures, are particular cases of the model Equation 3.17. In addition to being more general than most modelling techniques discussed so far, because NARMAX models are recursive in the outputs, i.e. use explicitly lagged versions of the system's output, the obtained models are parsimonious(Billings, 2013).

Before delving into the NARMAX system identification framework, it is important to mention that in the past some authors (Marmarelis, 2004; Victor and Canel, 1992; Zhao and Marmarelis, 1998) have acknowledged this methodology as a good candidate for obtaining models in neurophysiology. Despite this observation, the number of models for neurophysiological systems using this methodology is not large, however, it has started to be used with great success (Friederich et al., 2016).

As pointed out in (Billings, 2013), the term NARMAX has evolved from being just an acronym for this type of model to an identifier of a well-defined methodology that comprises the following steps

- Structure detection
- Parameter estimation
- Model validation
- Prediction
- Analysis

Structure detection is the first fundamental step of the NARMAX methodology. In this step, the model search space is defined by selecting a functional nonlinear expansion for $F[\cdot]$ and assigning specific values for the lags of the input, output and error sequences.Then, by systematically surveying the candidate M terms, a subset $m << M$ of them are selected to be part of the final parsimonious model that will capture the dynamical behaviour of the system. More details on how to select the terms can be found in (Billings, 2013)

The second step in the NARMAX methodology is parameter estimation. This step involves optimisation algorithms which compute unbiased parameters values for the previously selected model structure. In most algorithms based on orthogonal forward regression (OFR) (Billings et al., 1988), structure selection and parameter estimation are carried out in parallel.More details about this step can be found in (Chen, 2006; Chen et al., 1989; Hong et al., 2008; Orr, 1995).

Once a model has been selected, the next step within the NARMAX methodology is validation. The objective is to check if the selected model is unbiased and to assess how well it represents the real system. There is a full body of knowledge and algorithms that have been developed to validate NARMAX models, some relevant works are (Aguirre and Billings, 1995; Billings and Zhu, 1994, 1995; Coca and Billings, 2002).

After the model has been validated the next step is prediction. Here the obtained system's model is used to predict the output of the real system for a given input. Depending on a variety of factors such as the nature of the system and the application of the model, the predictions can be made using one step ahead, multi-step ahead or model predicted output techniques (Billings, 2013).

The last step of the NARMAX method is analysis. NARMAX models can be used for prediction/forecasting, system analysis and for control applications. For example, NARMAX models have been used to forecast DTS index (Pisoni et al., 2009). Given a polynomial NARMAX model, it is possible to derive analytically the Generalized Frequency Response Functions (Jones and Billings, 1989) and the Output Frequency Response Functions (Lang et al., 2007). These analysis tools were used in (Friederich et al., 2016) to demonstrate that phase-related features contained in temporal stimuli are selectively encoded and enhanced by fly photoreceptors by making use of nonlinear dynamics.

3.3.1 NARMAX Model Expansions

As mentioned before the nonlinear function F that maps one or multiple variables to the output of a system given by Equation 3.17 can be expanded in various forms (Pearson, 1995). A summary of some of these forms, NARMAX expansions, is given below.

Polynomial and Rational Implementations

Perhaps the most mature, applied and well-studied expansion is the polynomial NARMAX expansion. Maybe the fact that polynomials can approximate any given continuous function on an infinite interval (Functions, 1981) has contributed to its popularity. This expansion is defined as

$$\begin{aligned} y(t) = F_{poly} & \\ & \theta_0 + \sum_{i_1=1}^{n} \theta_{i_1} x_{i_1}(t) + \sum_{i_1=1}^{n} \sum_{i_2=i_1}^{n} \theta_{i_1,i_2} x_{i_1}(t) x_{i_2}(t) + \cdots \\ & + \sum_{i_1=1}^{n} \cdots \sum_{i_l=i_{l-1}}^{n} \theta_{i_1 i_2 \cdots i_l} x_{i_1}(t) x_{i_2}(t) \cdots x_{i_l}(t) + e(t) \end{aligned} \tag{3.18}$$

where l is the degree of the polynomial nonlinearity, $\theta_{[\cdot]}$ are the model parameters, $n = n_u + n_y + n_e$ and

$$x_m(t) = \begin{cases} y(t-m) & \text{if } 1 \leq m \leq n_y \\ u(t-(m-n_y)) & \text{if } n_y + 1 \leq m \leq n_y + n_u \\ u(t-(m-n_y-n_y)) & \text{if } n_y + n_u + 1 \leq m \leq n_y + n_u + n_e \end{cases} \tag{3.19}$$

This polynomial expansion includes two particular cases that are commonly used. The first one is the so-called ARMAX model which is achieved by choosing $l = 1$. And the second case is the NARX model which can be obtained when $n_e = 0$. From Equation 3.19 it can be seen that this expansion is linear in its parameters, which makes it suitable for the application of linear optimisation techniques, that is normally carried out within the orthogonal forward regression method, to solve the combined problem of the structure selection and parameter estimation to obtain a model of the system.

Introduced in (Billings and Chen, 1989), the rational expansion is a generalisation of the polynomial case. It is defined as (Billings, 2013)

$$y(t) = \frac{A[y(t-1), \cdots, y(t-n_y), u(t-1), \cdots, u(t-n_u), e(t-1), \cdots, e(t-n_e)] + e(t)}{B[y(t-1), \cdots, y(t-n_y), u(t-1), \cdots, u(t-n_u), e(t-1), \cdots, e(t-n_e)] + e(t)} \tag{3.20}$$

where $y(t)$, $u(t)$, $e(t)$, n_y, n_u, n_e are the same as in the polynomial expansion, $A[\cdot]$ and $B[\cdot]$ are polynomials similar to Equation 3.19. It is clear that by allowing $B[\cdot] = 1$ then model

Equation 3.20 reduces to 3.19. The advantage of this model over the polynomial case is that it can model systems which feature singular or near singular behaviour.

Extended Model Set NARMAX

So far the nonlinear mapping in Equation 3.17 has been using polynomials, but this doesn't need to be the case. The framework allows for the function $F[\cdot]$ to take any form that is convenient for the system that is being modelled. For instance, if a priori knowledge of the system suggest that its dynamical behaviour could be captured by a transcendental function such as the exponential, then this function can be included in the initial model set of the NARMAX methodology. According to (Billings, 2013) the previous description is achieved within the NARMAX method as follows

Let

$$\mathbf{x}(t) = [y(t-1), \cdots, y(t-n_y), u(t-1), \cdots, u(t-n_u), e(t-1), \cdots, e(t-n_e)]^T \tag{3.21}$$

If it is assumed that the nonlinear mapping $F[\cdot]$ in Equation 3.17 can be approximated by M predefined functions, linear or nonlinear, $\phi_1, \phi_2, \cdots, \phi_M$, i.e.

$$y(t) = \sum_{i=1}^{M} \theta_i \phi_i(\mathbf{x}(t)) + e(t) \tag{3.22}$$

where each function $\phi_i \mathbf{x}(t), i = 1, \cdots, M$ can be specified by a combination as many variables as $n = n_y + n_u + n_e$.

This previous definition allows for arbitrary functions such as sinusoids, exponentials or any other to form part of the NARMAX model. More details can be found in (Billings, 2013)

Radial Basis Functions and Wavelets Implementations

A particular case of the Multilayer Perceptron Networks, reviewed in (Haykin and Network, 2004), are Radial Basis Functions (RBFs) which consist of a single hidden and the $y_j(t)$ output of each j node is given by the output of an symmetric activation function that has as input the distance, Euclidean most of the times, between the input $x(t)$ and a fixed center c_j.

Each node's output $y_j(t)$ is given by

$$y_j(t) = g(||x - c_j||; \rho_j) \tag{3.23}$$

the g activation function is normally chosen to be a Gaussian function

$$g(\nu,\rho) = exp(-\nu^2/\rho) \tag{3.24}$$

where ρ is a positive scalar that defines the width of the function.

The Gaussian activation function is not only symmetric but also vanishes away from the center, i.e. $g(\nu,\rho) \rightarrow 0$ when $\nu \rightarrow \pm\infty$

It has been reported RBF model that use the Gaussian activation function have great approximation capabilities (Chen et al., 1991). The result of using RBF expansion to implement a NARMAX (Billings, 2013) model provides a useful system identification. The nonlinear mapping function f for this implementation is given by

$$f(x) = \sum_{j=1}^{m} w_j g(||x - c_j||) \tag{3.25}$$

When allowing the centres c_j to be adjustable parameters, then the Equation 3.25 is nonlinear in the parameters. In order to make the problem linear in the parameters,i.e. just the weights w_j have to be estimated, so its solution is easier and faster to obtain (Chen et al., 1991) the centres c_j are selected in advance using algorithms such as clustering.

For systems that contain severe nonlinear behaviour and fast and slow dynamics, wavelet decomposition techniques are a good alternative. Because of its capability to be localised in time and scale (frequency), the wavelet expansion has been used successfully in previous works (Billings and Coca, 1999; Coca and Billings, 2001). Different wavelet-based NARMAX model expansions have been developed, one example is the one in (Coca and Billings, 2001) which is based on the multiresolution analysis and is given by

$$y(t) = F_{wav}[\mathbf{x}(t)] \sum_i \theta_i \tilde{x}_i(t) + e(t) \tag{3.26}$$

where $\tilde{x}_i(t) = \tilde{x}_{j,k}[y(t-1),\cdots,y(t-n_y),u(t-1),\cdots,u(t-n_u),e(t-1),\cdots,e(t-n_e)]$ represents either a wavelet $\psi_{j,k}(\cdot)$ or scaling $\phi_{j,k}(\cdot)$ function, both obey the following equation

$$\tilde{x}_{j,k} = \begin{cases} 2^{\frac{j}{2}}\phi(2^j x - k) & \text{if } j = j_0 \\ 2^{\frac{j}{2}}\phi(2^j x - k) & \text{if } j > j_0 \end{cases} \tag{3.27}$$

where the dilation and translation indexes are j and k respectively. As reported in (Billings and Coca, 1999; Coca and Billings, 2001) systems that follow the definition given in Equation 3.17 can be decomposed into its functional components. Then, the individual functional components represent the contribution that each individual set of variables or a single variable has towards the total response of the system. This type of models are good at reducing the parameter space of models of systems with dynamics that have large varying dynamics.

Despite the intricate model definition of this expansion, the linearity in the parameters is still preserved, which means that the structure selection and parameter estimation procedures used for other simpler model expansions can still be used in this case.

3.3.2 Structure Selection and Parameter Estimation

Regardless of the specific implementation of the NARMAX model, the key step of the NARMAX system identification approach is model structure selection and parameter estimation which are closely related. Model structure selection is the process by which a subset $m << M$ significant terms of all the M candidate terms are selected to be part of the model.The task of parameter estimation involves finding the unbiased values for the parameters associated to each of the selected terms in the model.A characteristic of the model implementations discussed in Section 3.1 is that their model structure is linear-in-the-parameters such that the parameter estimation problem can be formulated as a linear regression problem.

Provided the selected expansion for the model has been chosen to be linear in the parameters, and a set of N input-output system data samples had been collected, then the general NARMAX model 3.17 can be expressed as a functional expansion described by the regression model by (Chen et al., 1989)

$$z(t) = F[\mathbf{x}(t)] = \sum_{j}^{M} \theta_j p_j(t) + \xi(t), t = 1, \cdots, N \tag{3.28}$$

where the collected output samples of the system, over the time range $t = 1 \cdot T_s, \cdots, N \cdot T_s$, with T_s being the sampling time; are represented by the dependent variable $z(t)$, and θ_j are the unknown parameters that need to be estimated. Also the modelling error, $e_m(t)$ as well as the noise $e(t)$ are represented by $\xi(t) = e_m(t) + e(t)$. Equation 3.28 can be expressed in matrix form as

$$\mathbf{z} = \mathbf{P}\theta + \xi \tag{3.29}$$

where

$$\mathbf{z}=\begin{bmatrix} z(1) \\ \vdots \\ z(N) \end{bmatrix}, \mathbf{P}=\begin{bmatrix} \mathbf{p}_1 & \cdots & \mathbf{p}_M \end{bmatrix}^T, \theta=\begin{bmatrix} \theta_1 \\ \vdots \\ \theta_M \end{bmatrix},$$
$$\xi=\begin{bmatrix} \xi(1) \\ \vdots \\ \xi_(N) \end{bmatrix}, \ and \ , \mathbf{p}_i=\begin{bmatrix} p_i(1) \\ \vdots \\ p_i(N) \end{bmatrix}, for \ i=1\cdots M \tag{3.30}$$

In Equation 3.29 the error sequence $\xi(1),...,\xi(N)$ is unknown and has to be estimated in an iterative manner as part of the parameter estimation routine. To that end, Equation 3.29 is written as

$$\mathbf{z}=\mathbf{P}_p\theta_p+\mathbf{P}_n\theta_n+\xi \tag{3.31}$$

The $\mathbf{P}_n$ matrix is made up of all noise-related regressors whilst the $\mathbf{P}_p$ matrix contains all candidate process (noise-free) terms.

In order to solve the Equation 3.31 approaches such as the one suggested in (Chen et al., 1989) are used. The approach involves estimating the process part first. Once the process model has been estimated, the residuals are used to estimate the noise model. When estimating the noise model, both θ_p and θ_n are iteratively re-estimated until the error sequence ξ converges to an unpredictable sequence, i.e. contains no more information about the dynamics of either the process or the noise. In the following, a very common approach, orthogonal forward regression, for carrying out this estimation process is briefly outlined.

The most common algorithm to perform model structure selection for NARMAX models is the orthogonal forward regression algorithm. In order to use this algorithm the first step is to cast the problem into a linear regression problem, i.e. one that follows Equation 3.29. Once the collected data from the system has been used to construct both the **P** matrix containing the candidate regressors, according to the selected NARMAX expansion and the system's output(s) are contained in **z**, then the combined problem of structure selection and parameter estimation can be solved. As mentioned above, the structure selection problem involves selecting out of all M candidate terms, just $\mathbf{p}_m$ with $m << M$ significant regressors that can represent the dynamical behaviour of the system. At the same time, the parameter estimation involved estimating the θ_m parameter values of each of the $\mathbf{p}_m$ selected terms. This process is done by solving

$$\hat{\theta}=\arg\min_{\theta} ||\mathbf{z}-\mathbf{P}_m\theta_m||_2^2 \tag{3.32}$$

Depending on the selected NARMAX expansion the search space where the relevant regressor should be selected from can be very large and make the search and selection process cumbersome (Chen et al., 1989). In order to address this issue orthogonal forward regression procedures, which allow an informed and efficient search have been developed (Billings et al., 1989, 1988; Korenberg et al., 1988a; Luo and Billings, 1995). The majority of these methods decomposed the **P** regression matrix as an orthogonal projection described by

$$\mathbf{P} = \mathbf{WA} \tag{3.33}$$

where **A** is $M \times M$ upper triangular matrix and $\mathbf{W} = [w_1, \cdots, w_M]$ is a $M \times M$ orthogonal matrix. This decomposition is very similar to the QR decomposition using either Gram-Schmidt, Modified Gram-Schmidt, Housholder (Chen et al., 1989) or Givens transformations(Luo and Billings, 1995).

After expressing the regression matrix in Equation 3.29 as an orthogonal projection given by Equation 3.33 the new problem to solve is described by

$$\mathbf{z} = \mathbf{W}\beta + \xi \tag{3.34}$$

where $\beta = [\beta_1 \cdots \beta_M]^T$ is an auxiliary parameter given by

$$\beta = \mathbf{A}\theta \tag{3.35}$$

Both the auxiliary regressor $\mathbf{w_i}, i = 1, \cdots, M$ and their corresponding β_i parameters are uncoupled, this enables the OFR algorithm to evaluate the individual contribution of each i^{th} regressor w_i towards minimising the distance between the measured and one-step ahead predicted output using Equation 3.32

A flow diagram of the OFR algorithm is shown in Figure 3.3. In that figure it can be seen that the structure selection process is performed in $k = 1, \cdots, m$ consecutive steps. In each step the uncoupled regressor that minimises the selected error criterion the most is selected and its value parameter computed. This procedure continues until the selected stopping criteria, which could be, for example, the final prediction error (FPE), Akaike(AIC) (Akaike, 1974) or Bayesian(BIC)(Schwarz et al., 1978) information criteria, has been met. A review with more stopping options can be found in (Leeb and Pötscher, 2009)

3.3.3 Model Validation

The most basic test to assess the accuracy is by simple inspection of its predicted output. It is common practice to use one-step ahead predictions to carry out this type of inspection.

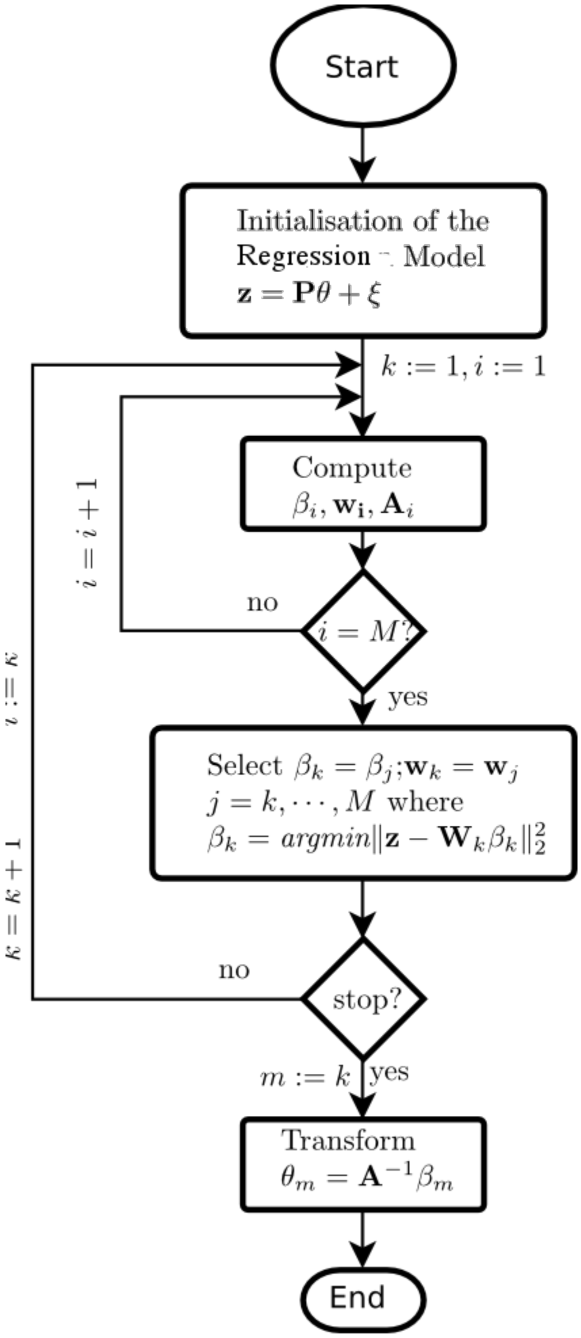

Fig. 3.3 Orthogonal forward regression flow diagram.

However since this way of predicting a system's response does not take into account the accumulation of the prediction errors, using multi-step ahead or pure model predicted output predictions yield a more accurate way of validating the model (van den Bosch and van der Klauw, 1994).

The assessment of the prediction/forecasting capabilities of the identified model can be carried out either by visually comparing the predicted output against the recorded data or by computing prediction error measures such as mean squared prediction error (MSE), root mean squared prediction error (RMSE), which for a data set of N input-output data have the following definitions

$$MSE = \frac{1}{N}\sum_{i=1}^{N}\left(z(i)-y(i)\right)^2, RMSE = \sqrt{\frac{1}{N}\sum_{i=1}^{N}\left(z(i)-y(i)\right)^2} \tag{3.36}$$

where the recorded output and the model predicted output are given by $z(t)$ and $y(t)$ respectively. Given that the measures defined in Equation 3.36 depend on the signal's power, it is common practice to normalise the signal using its variance (French and Marmarelis, 1999)

$$NMSE = \frac{\sum_{i=1}^{N}\left(z(i)-y(i)\right)^2}{N\sigma_z^2} \tag{3.37}$$

where the measured output signal's variance is given by σ_z^2.

When validating a model it is important to test its generalisation capabilities. This refers to the property that a model has to predict not only data that was used to derive the model but also systems output data that was not used in the model estimation process. This generalisation property is an indicator of how well a model has captured the true underlying dynamics of a system, as opposed of just fitting the data used in the estimation process.

In order to test the generalisation properties of a model, the input-output data set is split into training D design and test T data sets. Then the D data set is split again into training R and validation Q data sets. The training data set R is used for model estimation whilst the validation part for providing an estimation of the final generalisation properties of the selected model, this data set is used for selecting values for hyperparameters, the ones used in regularisation techniques (Larsen and Goutte, 1999) for instance, or selecting between different candidate models.

When the amount of available input-output data is not very large or when a more robust validation procedure is needed, techniques which involve splitting the data might not be suitable. One way to address this issues is to use cross-validation methods. These methods promote the efficient use of data by interchanging the validation and estimation data sets.

There are different ways of applying cross-validation techniques (James et al., 2013). Two of the most used ones are leave one-out and K-fold cross-validation (Stone, 1974). In these two approaches, the data set is divided into K subsamples. One of this K subsamples is then kept apart from the remaining K-1 subsamples, which are used to as training data to estimate the model.Then the one subsample which was kept apart is used during the validation stage. In the case of the LOO, K is equal to the number of data samples. More details about different cross validation techniques can be found in (James et al., 2013), and with particular application to NARMAX-based models in (Browne, 2000).

In addition to the prediction and generalisation capabilities of a model, when validating a model it is very useful to take a look at the information contained in the residuals, i.e. the prediction error. An accurately estimated model should have a prediction error which is unpredictable from all linear or nonlinear combinations of previous inputs and outputs (Billings and Voon, 1986; Billings and Zhu, 1994). In order to check that model has this property, correlation tests, auto, and cross, have been introduced. Autocorrelation tests check the correlation using just the residuals, whilst cross correlation tests use both the input and the residuals. Statistical validation of a NARMAX model can be assess by visually inspecting the output of the following statistical tests (Billings and Voon, 1986)

$$\begin{cases} \phi_{\xi,\xi}(\tau) = \delta(\tau) & ,\forall\tau \\ \phi_{u,\xi}(\tau) = 0 & ,\forall\tau \\ \phi_{\xi,(\xi u)}(\tau) = 0 & ,\tau \geq 0 \\ \phi_{(u^2)',\xi}(\tau) = 0 & ,\forall\tau \\ \phi_{(u^2)',(\xi)^2}(\tau) = 0 & ,\forall\tau \end{cases} \tag{3.38}$$

where the input and the residuals are represented by u and ξ respectively, $(\cdot)'$ means that the mean has been removed and the correlation function $\phi_{xy}(\tau)$ is given by

$$\phi_{xy}(\tau) = \frac{\sum_{t=1}^{N-\tau}[x'(t)][y(t-\tau)-\bar{y}]}{\sqrt{\sum_{t=1}^{N} x'(t)}\sqrt{\sum_{t=1}^{N} y'(t)}} \tag{3.39}$$

where $(\bar{\cdot})$ denotes the mean value of the variable, N is the number of data samples in the input-output dataset. If after visually inspecting that the output of the previous correlation test remains within the 95% confidence interval, approximately $\pm 1.96/\sqrt{N}$, then a model can be considered statistically validated.

In addition to the previous tests, the following set of correlation tests (Billings and Zhu, 1994)

$$\begin{cases} \phi_{(\xi^2)',(\mathbf{z}\xi)'}(\tau) = \kappa\delta(\tau) & ,\forall\tau \\ \phi_{(u^2)',(\mathbf{z}\xi)'}(\tau) = 0 & ,\forall\tau \end{cases} \tag{3.40}$$

where $\kappa, \in (0,1)$ is a constant and $\delta(\cdot)$ is the regular delta function, can be used to validate the identified model.

In recent years two new omnidirectional correlation tests have been proposed in (Zhang et al., 2007). According that work those tests have a better performance for models of higher dimensions.

3.3.4 Polynomial NARMAX analysis in the Frequency Domain

The models obtained for systems that evolve in time are normally expressed in the time domain. Once the model has been validated, apart from prediction, models are also used to obtain a physical interpretation of the system. It can be challenging to gain this type of insight by analysing models in the time domain. The main reason for that is the fact that a system in the time domain is very rarely uniquely represented and thus, is a harder to tell what are the relevant system's features by using just one out of the potentially many temporal representations. In order to facilitate the analysis, the model can be represented in the frequency domain, where given two models that represent the same system but have a different specification in the time domain, share very similar features in the frequency domain. This property has made the analysis of systems in the frequency domain a recurrent analysis tool in several engineering branches, for instance, automatic control, civil and mechanical (Lang et al., 2007).

In the case of the NARMAX methodology, there are tools that have been developed to analysed the estimated models in the frequency domain, particularly when for the case of polynomial NARMAX. It has been shown that when disregarding the noise terms of a polynomial NARMAX, under mild assumptions the model can be expanded as a Volterra functional polynomial (Diaz and Desrochers, 1988). This is very important since the tools developed for Volterra series in the frequency domain can thus be applied to the polynomial NARMAX. To elaborate briefly this argument recall that the Volterra series can be expressed as

$$y(t) = \sum_{n=1}^{\infty} y_n(t) \tag{3.41}$$

where the n^{th} order system output is given by

$$y_n(t) = \sum_{0}^{t} \cdots \sum_{0}^{t} h_n(\tau_1, \cdots, \tau_n) \tag{3.42}$$

with $h_n(\tau_1, \cdots, \tau_n)$ representing the Volterra kernel of order n. In order to obtain a frequency domain representation of the Volterra series, the multidimensional Fourier transform of each of the n^{th} kernels is obtained to yield the generalised frequency response functions (GFRF) defined as

$$H_n(j\omega_1, j\omega_2, \cdots, j\omega_n) = \sum_{\omega_1=-\infty}^{\infty} \cdots \sum_{j\omega_n-\infty}^{\infty} h_n(\tau_1, \cdots, \tau_n) e^{-j(\omega_1\tau_1, \omega_2\tau_2, \cdots, \omega_n\tau_n)} \tag{3.43}$$

Linear effects of the system can be studied by analysing the first order frequency response function $H_1(j\omega)$.The rest of the frequency response functions, i.e. for $n > 1$, are used to characterise all the nonlinear phenomena shown by the nonlinearity of the system. These phenomena include harmonics, intermodulation, gain compression and expansion, desensitisation (Billings et al., 1990; Chua and Ng, 1979; Zhang and Billings, 1993).

To obtain the GFRFs of a polynomial NARMAX efficient algorithms have been developed (Jones, 2007; Jones and Billings, 1989; Jones and Choudhary, 2012). These algorithms compute the first order frequency response function and then use it in a recursive fashion to efficiently compute the higher order frequency response functions. To show the basic idea, the polynomial NARMAX model Equation 3.19 can be expressed as

$$y(t) = \sum_{m=l}^{l} \sum_{p=0}^{m} \sum_{\tau_1, \tau_{p+q}=1}^{K} c_{p,q}(\tau_1, \cdots, \tau_{p+q}) \prod_{i=1}^{p} y(t-\tau_i) \prod_{i=p+1}^{p+q} u(t-\tau_i) \tag{3.44}$$

where the lagged input terms $u(t-\tau_i)$ and lagged output terms $y(t-\tau_i)$ of orders q and p respectively, form part of each term, such that the nonlinear dimension of each term is given by $p+q$. Each of these terms has a coefficient $c_{p,q}(\tau_1, \cdots, \tau_{p+q})$ which either depends on the θ_i, according to Equation 3.19 parameter or is zero because the term is not part of the model. All the possible permutations of lags that are part of the model are then generated by the multiple summation over τ_i, i.e. $\tau_i = 1, \cdots, K; i = 1, \cdots, p+q$. Using these notation and according to (Jones and Billings, 1989) the GFRFs of a NARX model can be obtained as

$$
\begin{aligned}
&\Big(1-\sum_{\tau_1}^{K} c_{1,0}(\tau_1)e^{-j(\omega_1+\cdots+\omega_n)\tau_1}\Big)H_n^{asym}(j\omega_1,\cdots,j\omega_n) = \\
&\quad \sum_{\tau_1,\tau_n=1}^{K} c_{0,1}(\tau_1,\cdots,\tau_n)e^{-j(\omega_1\tau_1+\cdots+\omega_n\tau_n)} + \\
&\quad \sum_{q=1}^{n-1}\sum_{p=1}^{n-q}\sum_{\tau_1,\tau_n=1}^{K} c_{p,q}(\tau_1,\cdots,\tau_{p+q})e^{-j(\omega_{n-q+1}\tau_{n-q+1}+,\cdots,+\omega_{p+q}\tau_{p+q}}H_{n-q,p}(j\omega_1,\cdots,j\omega_{n-q}) + \\
&\quad \sum_{p=1}^{n-q}\sum_{\tau_1,\tau_n=1}^{K} c_{p,0}(\tau_1,\cdots,\tau_p)H_{n,p}(j\omega_1,\cdots,j\omega_n) \qquad (3.45)
\end{aligned}
$$

where the contribution of the n^{th} order GFRF, which is generated by the nonlinearity of p^{th} degree in the recursive output, is given by $H_{n,p}(j\omega_1,\cdots,\omega_n)$. In the previous equation, $H(\cdot)$ is recursively computed as

$$
H_{n,p}^{asym}(j\omega_1,\cdots,j\omega_n) = \sum_{i=1}^{n-p+1} H_i(j\omega_1,\cdots,j\omega_i)H_{n-i,p-1}(j\omega_{i+1},\cdots,j\omega n)e^{-j(\omega_1+,\cdots,+\omega_n)\tau_p} \qquad (3.46)
$$

where $H_{n,1}(j\omega_1,\cdots,j\omega_i) = H(j\omega_1,\cdots,j\omega_n)e^{-j(\omega_1+\cdots+\omega_i)\tau_1}$

As reported in (Jones and Billings, 1989) the n^{th} GFRF is not unique, due to the fact that depending on the constellation of the ω_i arguments, different functions can produce the same frequency response function. In order to address this issue a symmetric GFRF $H_n^{sym}(\cdot)$, which value doesn't depend on the arrangement or its argument, was introduced. The actual value of this symmetric frequency response function is given by

$$
H_n^{sym}(j\omega_1,\cdots,j\omega_n) = \frac{1}{n!}\sum_{all\, permutations of\{\omega_1,\cdots,\omega_n\}} H_n^{asym}(j\omega_1,\cdots,j\omega_n) \qquad (3.47)
$$

The obtained GFRFs are given as an algebraic relationship between the coefficients of the NARMAX model and the ones in the GFRFs. An extension for systems with multiple-inputs and multiple outputs can be found in (Swain and Billings, 2001). This technique has been used successfully to analyse different systems (Boaghe et al., 1999, 2002; Li and Billings*, 2005; Peng et al., 2007)

Despite being a great tool to analyse systems in the frequency domain and gain insight, its interpretation is sometimes challenging because they are multidimensional functions (Yue et al., 2005).In order to address this issue a new concept, output frequency response functions, has been recently introduced (Lang et al., 2007). In contrast of GFRFs, this are one-dimensional functions of in the frequency domain that depend on the GFRFs and a given input for a Volterra or equivalent NARMAX model. The fact that they are one dimensional functions makes their interpretation and visualisation much easier than using the multidimensional GFRF functions. The output frequency response functions not only provide insight into which particular input frequencies contribute the output frequency spectrum but also how these frequencies affect the response of the system (Lang * and Billings, 2005; Peng et al., 2007).

According to (Lang et al., 2007), the output spectrum of a NARMAX can be expressed as

$$Y(j\omega) = \sum_{n=1}^{N} Y_n(j\omega)\forall\omega, \tag{3.48}$$

with

$$Y_n(j\omega) = \frac{1/\sqrt{n}}{(2\pi)^{n-1}} \int_{\omega_1+\cdots+\omega_n=\omega} H_n(j\omega_1,\cdots,j\omega_n)\prod_{i=1}^{n} U(j\omega_i)d\sigma_{n\omega} \tag{3.49}$$

where H_n and Y_n represent the n^{th} order GFRF and NOFRF of the system. It is important to notice that in practice the integral is replaced by a summation if the spectrum was obtained using the discrete Fourier transform.

An example of how to the NOFRF of a SISO system can be computed from data and then used to analysed that system can be found in (Lang * and Billings, 2005). The concept of NOFRFs has also been generalised for MIMO systems by Peng et al. (2007).

3.4 Discussion

This chapter provided an overview of system identification approaches and their applications to neuroscience. The state-of-the-art, NARMAX system identification methodology, which includes efficient model structure selection, parameter estimation, and model validation methods, was presented in more detail. The main advantages of the NARMAX method can be summarized as follows

- NARMAX models can describe a wide range of nonlinear systems
- It can be used to derive both SISO as well as MIMO systems

- It produces parsimonious model representations
- NARMAX models can be derived even from relatively small data sets (a few hundred data points)
- The noise is modelled explicitly ensuring unbiased parameter estimates
- The resulting models can be interpreted and analysed to provide insight into the properties of the underlying system

The NARMAX modelling approach is used to derive the photoreceptor and retinal network models described in later Chapters.

Chapter 4

A Unifying Empirical Model of R1-R6 Photoreceptors in Wild-type and Histamine-deficient *Drosophila* Flies

4.1 Introduction

State-of-The-art empirical photoreceptor models (Friederich et al., 2016, 2012) predict very accurately its response. A major limitation with these models is that these do not distinguish between the processing taking place at photoreceptor level and the contribution from the neurons in the lamina to the shaping of the photoreceptor responses. Specifically, these models do not take into account the actual connectivity between photoreceptors and the lamina. As consequence, these models can not be used to build a model of the whole retina, which reflects the actual connectivity between retina and lamina neurons. Another limitation of the existing models is that they cannot be tuned to reproduce the photoreceptor responses to multi-level naturalistic stimuli, measured in histamine deficient flies.

This Chapter introduces a new model of R1-R6 photoreceptors in *Drosophila*, which can be tuned to reproduce the photoreceptor responses of wild as well as histamine deficient flies for arbitrary stimuli, over the entire environmental range.

To address the above limitations, a previous model of the fly photoreceptor, developed and validated using recordings in wild-type (Friederich et al., 2016, 2009), was modified. The modified model incorporates separate gain control mechanisms for stimulus mean and contrast which allow adapting the model to capture the dynamics of photoreceptors in blind histamine deficient fruit flies. To derive the model, separate mean and contrast gain functions are estimated by solving the corresponding nonlinear inverse problem using optimisation techniques. The estimated gains are used to derive separate dynamic gain control models for wild-type and mutant flies. The models are validated using experimental recordings.

The Chapter is organised as follows. Section 2 provides an overview of the previous modelling approaches and models used to characterise photoreceptor responses.

of the approaches used to model drosophila photoreceptors of the current state-of-the art models.

Section 3 explains the limitations of the previous state-of-the-art model of R1-R6 photoreceptors (Friederich et al., 2016), in modelling the histamine deficient mutants hdc$^{\mathrm{JK910}}$.

Section 4 introduces the new gain control architecture incorporating separate mean and contrast gain variables. Experimental recordings from both wild-type and hdc$^{\mathrm{JK910}}$ flies are used to estimate the gain functions that are then used to derive the final gain control models.

Section 5 presents the derivation and validation of the new models using experimental data recorded for both wild-type and mutant flies.

Section 6 provides a summary of the model and its relevance, as well as the conclusions for this Chapter.

4.2 An Overview of Existing Photoreceptor Models

There have been two main approaches to model fly photoreceptors. The first approach takes into account the molecular interactions that take place during the phototransduction cascade and the propagation of electrical signals along the membrane (Peretz et al., 1998; Pumir et al., 2008; Song et al., 2009, 2012).

The second approach involves using system identification approaches to derive empirical, black-box models that predict photoreceptor responses to arbitrary stimuli (Friederich et al., 2009; Hateren and Snippe, 2006).

The biological models aim to characterise the processes and mechanisms of phototransduction at a molecular level. Such models allow biologists to understand how photoreceptors process visual information. In contrast, empirical models reveal what photoreceptors actually compute (Carandini et al., 2005).

This characteristic makes this type of models very attractive for biologists and neuroscientists. Examples of these models can be found in (Hardie and Postma, 2008c; Nikolic et al., 2010; Niven et al., 2003c; Song et al., 2012)

The study presented in (Niven et al., 2003c) uses the responses of photoreceptors from wild-type and Shaker *ShKS133* flies. These two types of flies were stimulated with a white-noise current signal. Using intracellular recordings of the experiments the authors concluded that losing K+ conductances produced a marked reduction in signal-to-noise ratio of photoreceptors. This decrease of signal-to-noise ratio led to a 50% information capacity loss. These results were used in conjunction with the Hodgkin-Huxley equations to produce a photoreceptor model.

Although not presenting a photoreceptor model, the work in (Hardie and Postma, 2008c) describes the mechanisms that participate in the phototransduction cascade. In this work, a new hypothesis regarding important mechanisms in the activation stage of the phototransduction cascade is introduced.

A quantitative phototransduction cascade model is presented in (Nikolic et al., 2010). The model consists of 4 stages: light absorption, signal amplification, regulation of the ionic current of the cell and positive and negative feedback calcium mechanisms. The model is stochastic and capable of simulating single photoreceptor responses, quantum bump.

Arguably the most advanced biophysical model of the fruit fly photoreceptor is the stochastic four-stage model which was developed in (Song et al., 2012). The reported model has quantitative models light-sensitive and light-insensitive parts of the photoreceptor. The model is composed of two sections. The Rhabdomere section, which is divided into 3 stages: photon absorption model, phototransduction cascade, and bump summation model. The Soma section which uses a Huxley-Hodgkin to model the cell body. This model represents an improvement of the previous model not only because it uses the insights provided by previous works (Hardie and Postma, 2008c; Nikolic et al., 2010) to model the molecular mechanisms of the phototransduction cascade, but also is a more comprehensive that has been validated experimentally using naturalistic stimuli as opposed to white noise stimuli used in (Nikolic et al., 2010). The use of naturalistic stimuli to develop and validate photoreceptor models is crucial since it is known (Simoncelli and Olshausen, 2001; van Hateren, 1997) that photoreceptors respond nonlinearly to such stimuli.

The biophysical models reveal the underlying mechanisms but are not as accurate when trying to understand the underlying molecular mechanisms of that take place in the photoreceptor. However, when the aim of the study is to understand the signal processing algorithms and computations carried out by the sensory neurons, the complexity of biophysical models, reflected by the number of parameters and the nature of the equations plus the assumptions made, make these models unsuitable for this purpose (Badoual et al., 2006).

To understand what photoreceptors compute, one needs to rely on simple, empirical models that can predict accurately photoreceptor responses to arbitrary stimuli. A review of black box models used in system identification can be found in (Billings, 2013) and (Marmarelis, 2004). These models do not reveal the underlying biophysical mechanisms(i.e. how photoreceptors compute) but can be analysed mathematically to determine the computations performed by photoreceptors.

The crucial step in the process of deriving a model directly from experimental data using system identification is to determine the model structure. In the first instance, the modeller has to decide if the dynamics can be capture by a simpler linear model or requires fitting a more complex nonlinear model. In the case of fly photoreceptors, it has been shown that, under naturalistic estimulation, the photoreceptor response is nonlinear (Simoncelli and Olshausen, 2001; van Hateren, 1997).

Some of the models derived in the past include the Volterra and Hammerstein models of the photoreceptor of the blue bottle fly (*Calliphora vicina*) developed in (French et al., 1993). Specifically, the first- and second-order Volterra kernels were estimated from data using a sequence of combined step responses which were used in a light-adapted and dark-adapted setup.

In this case, the linear filter was the previously obtained first-order Volterra kernel and the nonlinearity was a sixth-order polynomial series, obtained using the Gram-Schmidt procedure. The performance of this second model was better than the one using the just the Volterra kernels. However, the authors developed a third model consisting of a NLN cascade. The rationale behind this model was, according to the authors, that there are nonlinearities at the end of the phototransduction cascade. This third model was able to predict the response with a mean square error of 1.55%.

Although the last model presented in this work had great accuracy the following points should be considered. The model organism used was not *Drosophila* which makes it easier in practical terms since the fly is bigger which facilitates the experiments. However, it has the drawback that is not possible to take advantage of the genetic 'toolbox' available for *Drosophila*, which is useful in understanding the effect that other neural layers have in modulating the photoreceptor response. Another limitation of the model is the stimuli used to obtain the response. The sequence of steps does not provide stimulation to the one the fly is likely to encounter in its natural environment, which is crucial in obtaining a more realistic model.

In a more recent study (van Hateren and Snippe, 2001) the authors have used blowfly as a model organism to obtain models of photoreceptors. The study used natural time series of intensities as stimuli to obtain the models. The purpose of this type of stimulation was to excite the photoreceptor in conditions similar to the ones the fly encounters in its natural environment. As mentioned before this is a crucial step to obtain more accurate models of photoreceptors. In great part, this is due to the nonlinearities that are elicited by the photoreceptor when this type of stimulation is used. Different model architectures were tested. The simpler architectures consisted of linear Wiener filters. More sophisticated architectures added static nonlinearities, such a square root operator, to the linear filter. The most sophisticated architectures presented in this work included low-pass filters, feedback loops, static and dynamic nonlinearities. The most accurate model reported in this work was a cascade of a low-pass filter with two loops with low-pass filters followed by a static nonlinearity. In this case the performance of the models was assessed by a coherence function obtained using information theoretical techniques. The models presented in this study, in particular the last one, was an improvement with respect to the previous model, mainly because the type of stimulation used. However the nonlinearities used to capture the photoreceptor's response were selected somehow ad-hoc.

The empirical photoreceptor model derived by (Friederich et al., 2016) is arguably the most accurate and thoroughly validated fly photoreceptor model. The model was developed using *in vivo* single-electrode recordings of intracellular voltage responses of *Drosophila* photoreceptors intensities experienced by the fly in its natural environment. This model that captures both the transient and the steady state response of the photoreceptor very accurately, was derived from data using the NARMAX (Billings, 2013; Chen and Billings, 1989b) system identification methodology. In this context, it is worth noting that both the Wiener and Hammerstein models can be regarded as particular cases of the NARMAX models.

4.3 Adaptive Model of the Fly Photoreceptor

The photoreceptor model consists of a polynomial discrete-time NARMAX model, depicted in Fig. 4.1, with variable input gain and a dynamic gain control model that adapts the input gain according to the mean light intensity (Friederich et al., 2016). The gain control model contains three branches, each of which accounts for three different adaptation time-scales. These three different time scales can be related to 1) the plateau in calcium concentration that the rhabdomere reaches after a light step. This plateau is achieved in the order of milliseconds. 2) The pupil mechanism that reduces the Ca^{2+} and has a time scale of seconds and 3) slow adaptation mechanisms such as translocations of signalling proteins in the cell membrane. This last mechanism can take from minutes to hours.

In particular each branch of the gain controls is composed of three blocks: a linear filter, a nonlinear divisive exponential transformation, and a saturation function. The linear filter accounts for the first order system dynamics which are common in neural systems and are related to capacitances and conductances in cells. The nonlinear divisive gain was introduced to relate the mean light intensity level and the observed gain control in steady state. Finally, a saturation block was included to prevent the previous nonlinear divisive gain to reach very large values which are biologically infeasible. A more detailed explanation of each block of the model can be found in (Friederich et al., 2012).

This model was validated using data from six different animals by using the techniques presented in Chapter 3. The normalised mean squared error of the model in steady state was of less than 1% for all the mean light level intensities. This model is not only more accurate than the previously developed models but also it has been extensively validated using experimental recordings from photoreceptors in different flies.

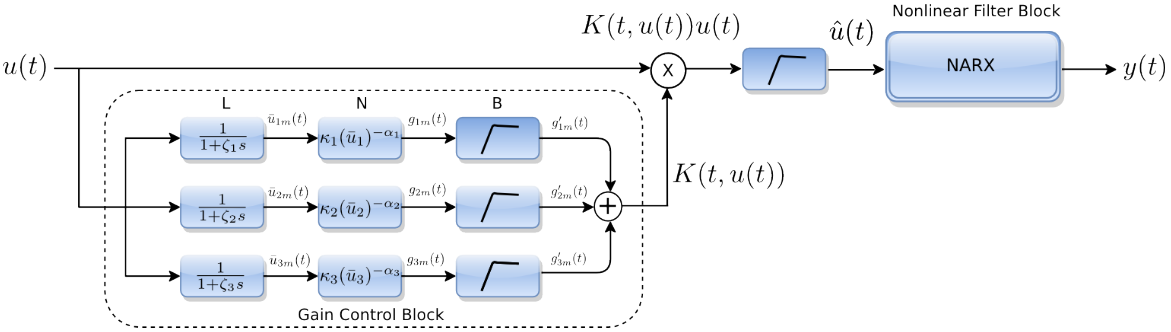

Fig. 4.1 Block diagram of the empirical model proposed in (Friederich et al., 2009).

The NARX model is described by the following equation,

$$\begin{aligned} y(t) = {} & \theta_1 y(t-1) + \theta_2 y(t-3) + \theta_3 \hat{u}(t-5)\hat{u}(t-4) \\ & + \theta_4 + \theta_5 \hat{u}(t-6) + \theta_6 \hat{u}(t-4) y(t-6) \\ & + \theta_7 \hat{u}(t-7) + \theta_8 \hat{u}(t-7)\hat{u}(t-6) \\ & + \theta_9 y(t-4) + \theta_{10} y(t-5) + \theta_{11} \hat{u}(t-4) y(t-5) \\ & + \theta_{12} \hat{u}(t-4) y(t-2) + \theta_{13} \hat{u}(t-7)\hat{u}(t-3) + \theta_{14} \hat{u}(t-5) \\ & + \theta_{15} \hat{u}(t-4) \end{aligned} \tag{4.1}$$

$\hat{u} = Ku(t)$ where u is the input and K is the input gain given Equation 4.2. $y(t)$ is the voltage response of the photoreceptor. The specific values for the θ parameters of the model can be found in (Friederich et al., 2013). This model was derived for a sampling frequency of $f_s = 400Hz$.

In Equation 4.2 $K(t,u(t))$ is defined as a superposition of three input gains

$$K(t,u(t)) = \sum_{i=1}^{3} K_i(t,u(t)) \tag{4.2}$$

where each K_i gain is the output of a cascade linear-nonlinear model having the photoreceptor stimulus as the input. Each K_i is composed of

(L) A linear dynamical system which approximates the local mean light intensity level, $\bar{u}(t)_i$, for a particular time-scale which is described by the constant ζ in the following Equation

$$\zeta_i \frac{d\bar{u}_i(t)}{dt} + \bar{u}_i(t) = u(t) \tag{4.3}$$

(N) A nonlinear divisive exponential transformation which describes the relationship between the static gain(g_i), obtain as the mean of the $K_i(t)$ during the last 4 seconds, and the light intensity stimulus. This relationship is given by the equation

$$g_i(t, u(t)) = \kappa_i \bar{u}(t)^{-\alpha_i} \tag{4.4}$$

Then by combining the static gain response given in Equation 5.12 with time scale processing, its corresponding linear filter, Equation 4.3 the equation for $g_i(t)$ is

$$g_i(t, u(t)) = \kappa_i \left(g_{0,i} e^{-t/\zeta_i} + \frac{1}{\zeta_i} \int_0^t e^{-(t-\tau)/\zeta_i} u(\tau) d\tau \right)^{-\alpha_i} \tag{4.5}$$

(B) Lastly, a saturation function $g'(t, u(t))$, that takes into account the physiological limitations of the system is defined as

$$g'(g, \beta) = \beta + \frac{g(t) - \beta}{1 + e^{(g(t) - \beta)}} \tag{4.6}$$

The adaptive model has been tested using experimental data collected from 6 different wild-type fruit flies. Overall, the relative prediction error was below 4% (Friederich et al., 2016).

As seen in Fig. 4.2 the model predicts well photoreceptor responses in wild-type flies but fails to predict the response of photoreceptors of histamine deficient fruit flies. Particularly for L-0 intensity level. At this bright light intensity level whilst the mean response of the histamine deficient fly photoreceptor is similar to the wild-type, the variance of the response is significantly compressed. Given that $K(t, u(t))$, Equation 4.2, controls only the mean response of the photoreceptor model, by adjusting this parameter alone, this model can not be tuned to reproduce the responses of photoreceptors of histamine deficient flies.

In order to address this issue a new model structure which involves two separate gain parameters for mean and contrast and two corresponding gain control loops is introduced in the next section.

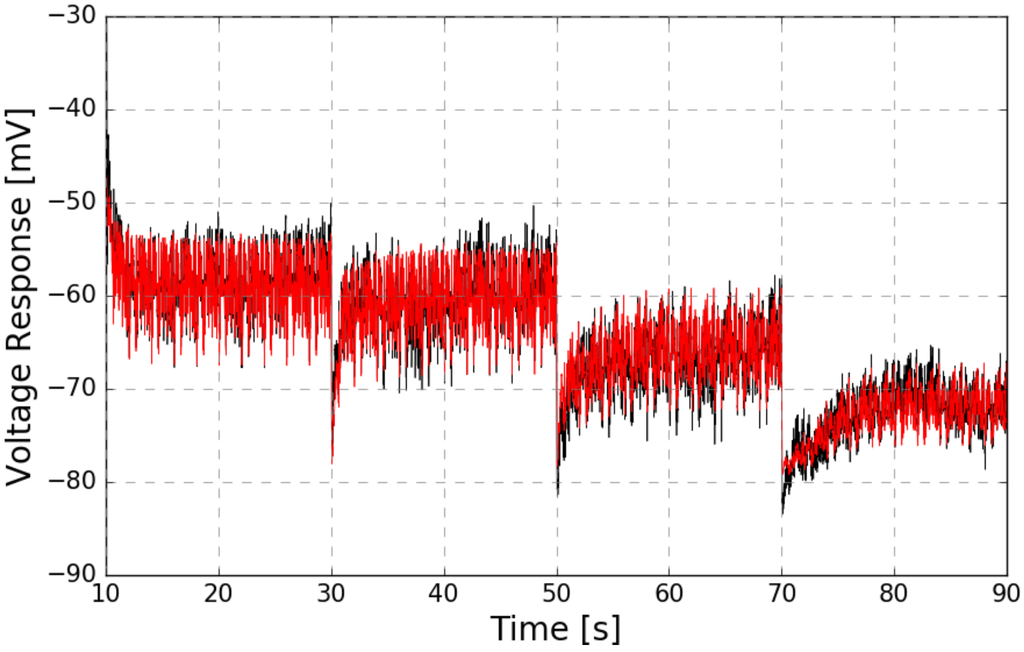

(a)

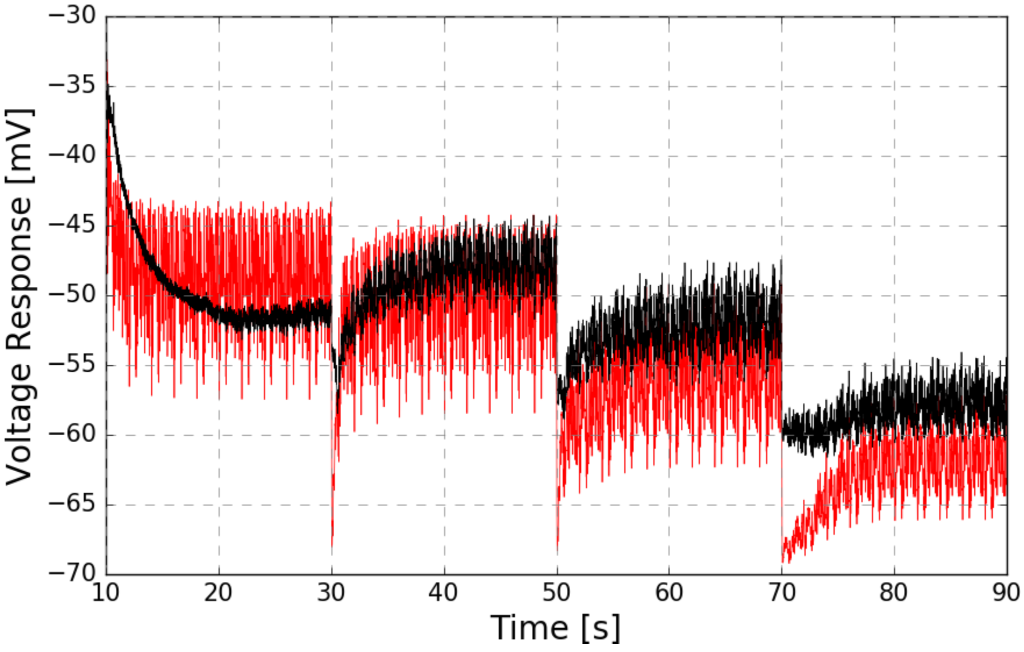

(b)

Fig. 4.2 Photoreceptor response to naturalistic stimuli shown in Fig. 2.5. (a) Comparison between recorded data and model response of the wild fly. The comparison for the mutant fly is shown in (b). Recorded data is shown in black and model responses are shown in red.

4.4 Mean and Contrast Adaptation in Drosohpila's Photoreceptor

The model described in the previous section processes data in two stages:

1. The gain adaptation stage which adapts the input gain according to the mean intensity level. This model describes both the transient dynamics during gain adaptation as well as the steady state gain for different mean intensity levels. In this stage, the model adapts the input according to the mean intensity level, so the next stage can function as required. It should be mentioned that whenever there is a change in mean intensity level, the gain adaptation mechanism has a major contribution to the response. That is to say, the transient response of the system to large changes in the input is mainly captured by this part of the model.
2. The nonlinear NARX filter characterises the nonlinear transformations/encoding of the input signal at photoreceptor level.

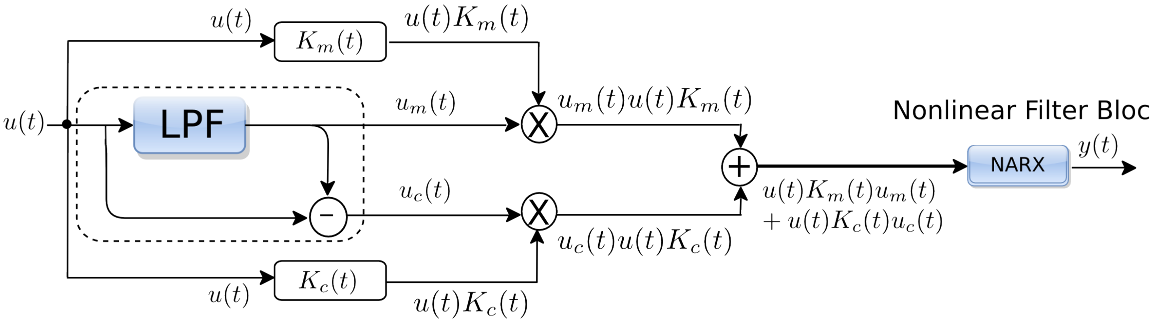

Fig. 4.3 Block diagram of the new photoreceptor model.

Specifically, the model can not predict neither the transient dynamics or steady state response over the entire environmental range as illustrated in Fig. 4.2(b).

As described in the previous section, this model fails to predict the response of histamine deficient fly photoreceptors. There are discrepancies in transient and steady state. The greater discrepancy between the predictions and the recorded data is in steady state for the stimuli that correspond to the brightest light. In addition, it has been reported (Friederich et al., 2016) that histamine deficient and wild-type fly photoreceptors have a very similar response to light adapted naturalistic stimulation is very similar. These facts suggest that the NARX filter of the current model could be used for both wild-type and mutant fly photoreceptors. However, some changes are needed for the gain adaptation stage.

To address this issue, in this thesis a model with a structure that adapts the mean and contrast of the input using two separate mechanisms is introduced. The proposed model structure is shown in Fig. 4.3

In this new model's structure the main novelty is the introduction of separate control gains, $K_m(t, u_m(t))$ and $K_c(t, u_c(t))$ for mean, $u_m(t)$ and variance, $u_c(t)$, components of the stimulus. This strategy provides an extra degree of freedom so the mean and the contrast of the input stimuli can be adapted separately.

The estimated mean and contrast components of the stimulus were computed by approximating the stimulus mean by smooth-filtering the stimulus. Moving average filters of different window sizes and digital versions of simple 1st order linear filters were tested. After testing the output of different filters the one with the best performance when solving the optimization problem Equation 4.21 was a simple first order filter described in the Laplace domain by the following equation

$$U_m(s) = \frac{K_{ss}}{1+\tau s} U(s) \tag{4.7}$$

The implementation of the filter in digital form was carried out by using the Tustin transformation (Ogata, 1995)

$$s = \frac{2}{T}\frac{z-1}{z+1} z = e^{sT} \tag{4.8}$$

After algebraic manipulations the equation of the filter is given by

$$u_m(k) = A[u(k) + u(k-1)] - Bu(k-1) \tag{4.9}$$

where

$$A = \frac{K_{ss}}{a} \tag{4.10}$$

$$B = \frac{b}{a} \tag{4.11}$$

$$a = 1 + 2f_s\tau \tag{4.12}$$

$$b = 1 - 2f_s\tau \tag{4.13}$$

The sampling frequency was selected $f_s = 400$. And constants $K_{ss} = 1, \tau = 1$. Using these values the selected filter is given by

$$u_m(t) = 0.0012[u(t) + u(t-1)] + 0.9975u_m(t-1) \tag{4.14}$$

And then, remove the approximated mean from the original stimulus to obtained the variance of the signal, u_c. This process is described by the following equation

$$u_c(t) = u(t) - u_m(t) \tag{4.15}$$

A block diagram of the decomposition algorithm is presented in Fig. 4.4

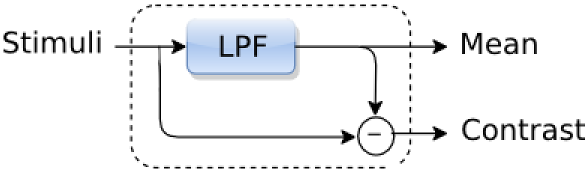

Fig. 4.4 Block Diagram illustrating the implementation of the mean, $u_m(t)$, and the mean-removed stimuli, $u_c(t)$.

The result of applying the decomposition algorithm to the stimuli that were used in the wild and mutant flies is shown in figure 4.5.

4.4.1 A New Photoreceptor Model Structure Incorporating Mean and Contrast Gain Control

The new model structure with separate mean and contrast gain control is described by the following definitions and equations

$$u(t) = u_m(t) + u_c(t) \tag{4.16}$$

It is assumed that given a function

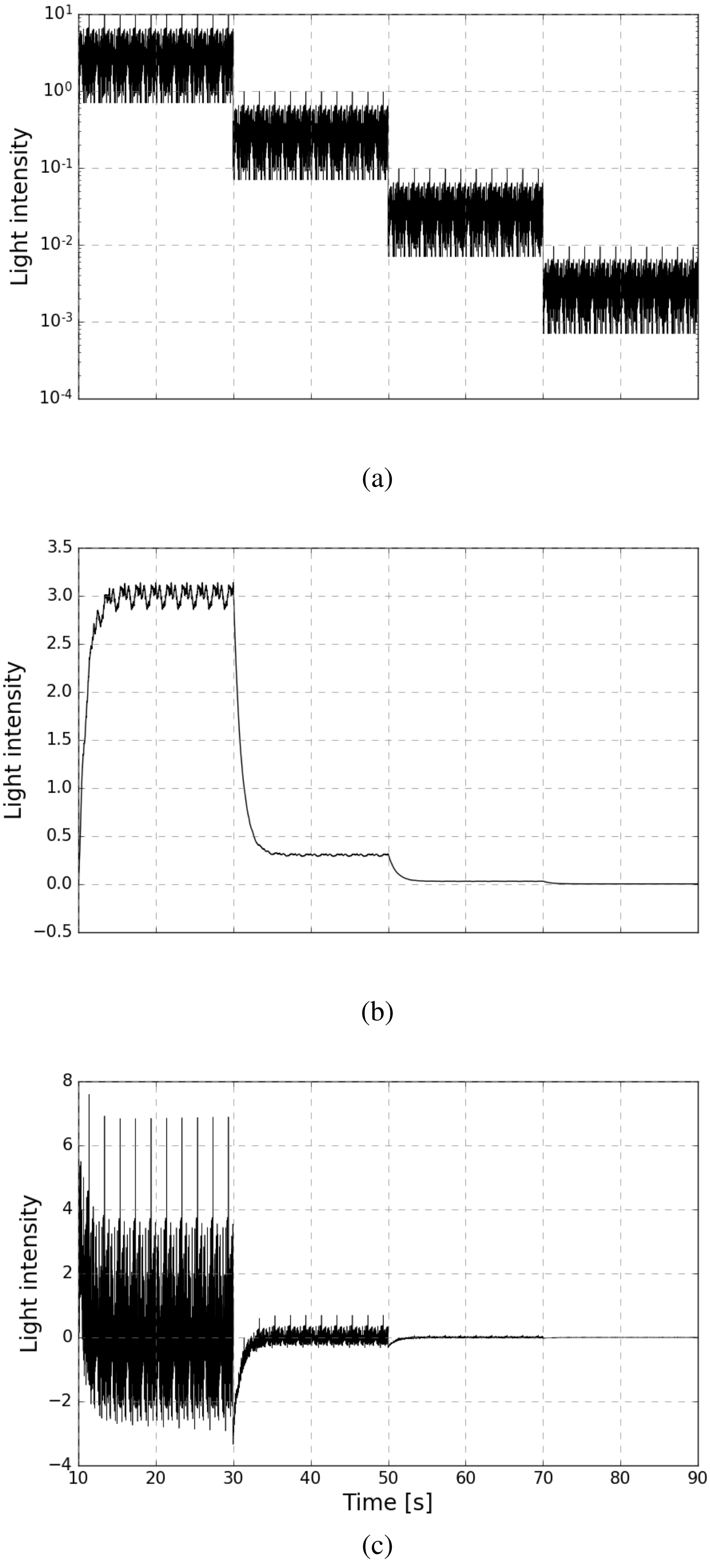

Fig. 4.5 Wild and mutant light stimuli decomposition into their mean and contrast components. (a) naturalistic stimuli for the wild-type fly. Its mean and mean-removed components are shown in (b) and (c) respectively.

$$
\begin{aligned}
y(t) = NARX\big(&y(t-1),\cdots,y(t-6), \\
&[K_m(t,u(t))u_m(t)+K_c(t,u(t))u_c(t)]u(t-1),\cdots \\
&[K_m(t,u(t))u_m(t)+K_c(t,u(t))u_c(t)]u(t-7)\big) \qquad (4.17)
\end{aligned}
$$

where

$$K_m(t,u(t)) \in L^2(\Delta_t) \qquad (4.18)$$

$$K_c(t,u(t)) \in L^2(\Delta_t) \qquad (4.19)$$

where $\Delta_t = [t_{min}, t_{max}]$ denotes a given time interval and L^2 is the infinite-dimensional function space of square integrable functions.

The hypothesis of the proposed model is that given the experimental input/output data obtained from either wild-type or mutant fly photoreceptors. There exists two functions $K_m(t)$ and $K_c(t)$, which help adapting the mean and contrast components of the stimulus, such that the model prediction error $e(t) = y(t) - \hat{y}(t)$ satisfies $||e(t)||_2^2 < \rho, t \in [t_{min} t_{max}]$, where ρ is a given error tolerance. The estimation of the gain functions from data is detailed in the following section.

4.4.2 Estimation of the Mean and Contrast Gain Control Functions for Wild-type and hdc$^{\mathrm{JK910}}$ Photoreceptors

The estimation of the adaptation functions for the proposed photoreceptor model, described in Equation 4.17, is formulated as an optimisation problem on an infinite-dimensional function space. The numerical solution to the nonlinear optimisation problem, is obtained by solving a finite-dimensional approximation of the infinite-dimensional optimisation problem.

The infinite dimensional nonlinear optimisation problem is as follows

$$\mathsf{minimize}_{K_m(t),K_c(t)\in L^2(\Delta_t)} \sum_{\Delta_t} |y(t) - z(t)|^2 \qquad (4.20)$$

where $y(t)$ is the model described in Equation 4.17 and $z(t)$ is the recorded response of the photoreceptor for the stimulus $u(t)$

To solve Equation 4.20 the following finite-dimensional approximations of the gain functions $K_m(t)$ and $K_c(t)$ are introduced.

$$\mathbf{\hat{c}_{j_g}} = \arg\min_{\hat{c}_{jg}} \sum_{\Delta_t} \Big| NARX\big(y(t-1),\cdots,y(t-6), K_m(t)u_m(t) + K_c(t)u_c(t)u(t-1),\cdots \\ K_m(t)u_m(t) + K_c(t)u_c(t)u(t-7)\big) - z(t)\Big|^2 \tag{4.21}$$

where

$$K_m(t) = \sum_{k_m} c_{k_m} \phi_{m_{jg,k^m}}(t) \tag{4.22}$$

$$K_c(t) = \sum_{k_c} c_{k_c} \phi_{c_{jg,k^c}}(t) \tag{4.23}$$

where

j_g is the resolution level that will will be used in 'dictionaries' of scaling functions. And $\phi_{m_{jg,k^m}}(t) = \phi_{m_{jg,k^m}}(2^{j_g}t + k^m)$. Similarly $\phi_{c_{jg,k^c}}(t) = \phi_{c_{jg,k^c}}(2^{j_g}t + k^c)$ are two 'dictionaries' of third order Battle(Battle, 1987)-Lemarie(Lemarié, 1988) scaling basis functions and the coefficients $c_{k_m}, c_{k_c} \in \mathbb{R}$. These scaling functions were selected as suggested in (Friederich, 2011). This scaling function is shown in Fig. 4.6. A Battle-Lemarie Scaling function of order n is defined as follows

$$\phi^{(n)}(t) = \sum_{k\in\mathbb{Z}} \alpha_k^{(n)} B^{(n)}(t-k) \tag{4.24}$$

where the $\alpha_k^{(n)}$ coefficients were calculated as in (Leu et al., 1998). The numerical values of the coefficients are shown in Table 4.1

$$B^{(n)}(t) = \frac{1}{(n+1)!} \sum_{i=0}^{n+1} (-1)^i \binom{n+1}{i} (t-i)_+^n \tag{4.25}$$

Also $(t-i)_+^n$ indicates $(t-i)^n$ if $t-1>0$ and 0 otherwise.

Using the definition of the Battle-Lemarie scaling function, a 'dictionary' $\mathscr{O}$ of such scaling functions is defined as

$$\mathscr{O}_{j_g} = \left\{ P_{V_{jmax}} \phi_{j_g,k}(t) | j_g > j_{max}; j,k \in \mathbb{Z} \right\} \tag{4.26}$$

where $P_{V_{jmax}} \phi_{j_g,k}(t)$ denotes the projection of $\phi_{j_g,k}(t)$ into the space V_{jmax}

Table 4.1 Coefficients for the generation of Battle-Lemarie scaling functions

Coefficient number	Numeric Value
1	0.541736
2	0.30683
3	-0.035498
4	-0.0778079
5	0.0226846
6	0.0297468
7	-0.0121455
8	-0.0127154
9	0.00614143
10	0.00579932
11	-0.00307863
12	-0.00274529
13	0.00154624
14	0.001333086
15	-0.000780468
16	-0.00065562
17	0.000395946
18	0.000326749
19	-0.000201818
20	-0.000164264
21	0.000103307

Solving the optimisation problem Equation 4.21 is computationally expensive given the potentially large number of unknown parameters. To address this issue, a sliding window optimisation approach proposed in (Friederich, 2011) was adopted. The optimisation procedure is summarised below.

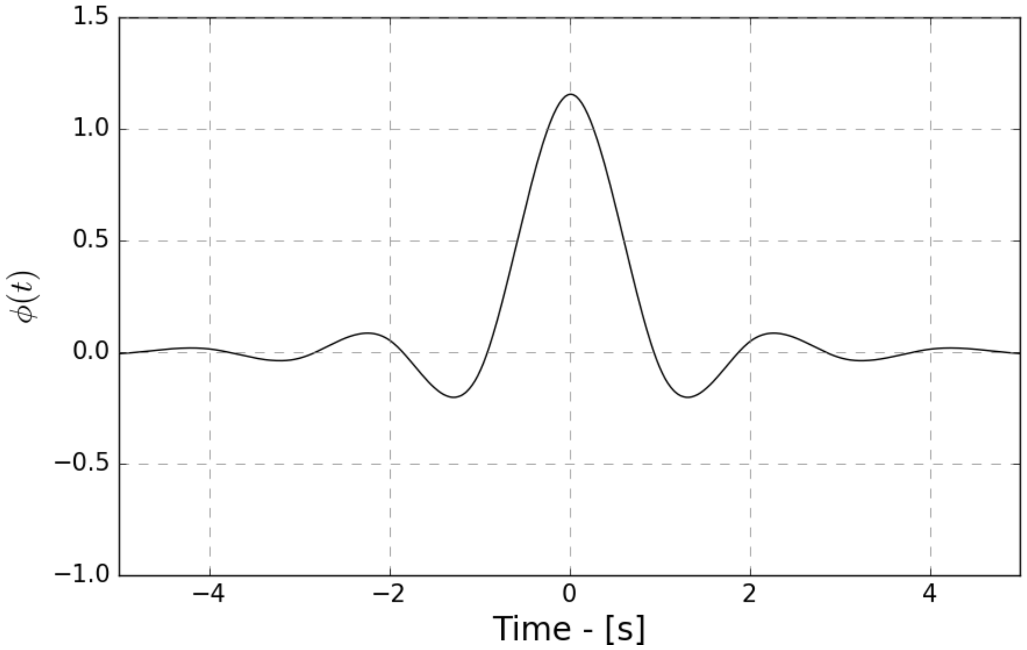

Fig. 4.6 Battle-Lemarie 3rd Order Scaling Function.

The estimation algorithm consist of the following main steps

- Step 1
    - Select the resolution level j_g, i.e. the exponent in the equation $\phi_{m_{j_g,k^m}}(t) = \phi_{m_{j_g,k^m}}(2^{j_g}t + k^m)$, and obtain the distance j_d to the maximum resolution, defined as $j_{max} = 2^{-jd} f_s$ where f_s is the sampling frequency.
    - Heuristically select the b_d optimisation interval, the overlap between the sliding window and the signal being approximated, i.e. $z(t)$
    - Provide initial guesses for $\hat{K}_m^{[0]}(t)$ and $\hat{K}_c^{[0]}(t)$
    - Initialise $k = 1$ the translation parameter, i.e. the distance between the lower end of the optimisation window in the first and second iterations, which is used to slide the window across the entire optimisation range.

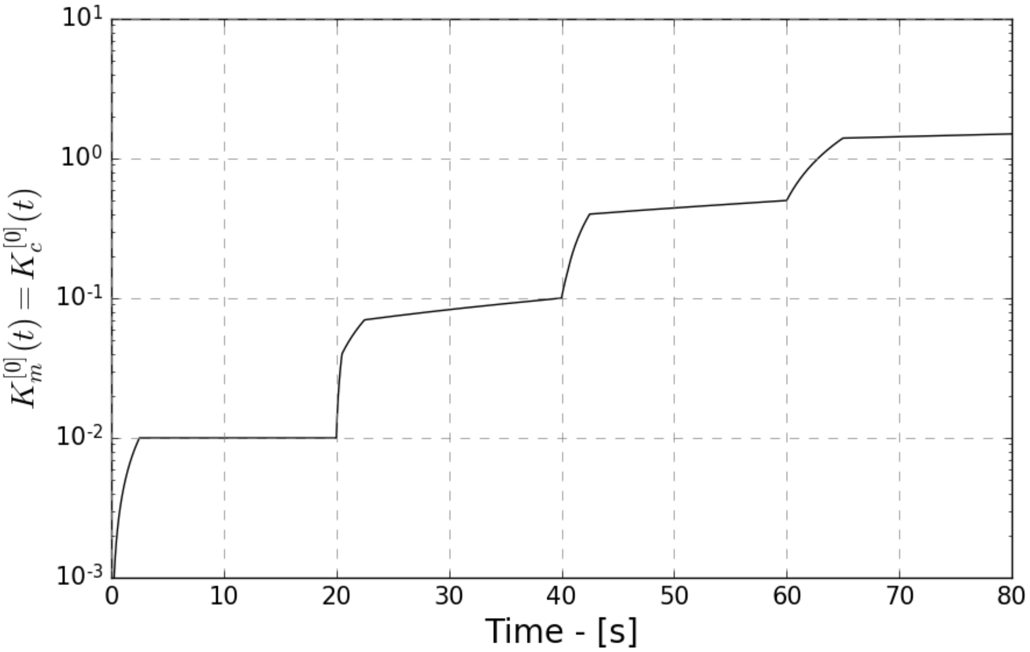

Fig. 4.7 Initial Guess for Mean and Contrast Adaptation Gains.

- Calculate the extended time interval $\hat{\Delta}_t$ using the following formula

$$\hat{\Delta}_t = \big[t_{2^{j_d}\frac{n_\phi-1}{2}+1}, t_{2^{j_d}\frac{n_\phi-1}{2}}, \dots, \\ t_2, t_1, t_2, \dots, t_N, t_{N-1}, \dots, t_{N-(N'-N)}, \dots, t_{2^{j_d}\frac{n_\phi-1}{2}-1}\big] \tag{4.27}$$

  where N is the number of samples of the input stimuli, n_ϕ is the number of filter coefficients part of the impulse response of the scaling function. And N' is given by

$$N' = 2^{j_d}\left(\left\lfloor \frac{N}{2^{j_d}} \right\rfloor + n_\phi - 1\right) + 1$$

- Set k_{max} as the maximum number of steps that the sliding window needs to be slided to cover $\hat{\Delta}_t$ entirely.

• Step 2

- Compute the ’dictionaries’ $\mathscr{O}_{j_d,\hat{\Delta}_t}$ and $\mathscr{P}_{j_d,\hat{\Delta}_t}$ of scaling functions and store them in matrix form $\mathbf{M}_{j_d,\hat{\Delta}_t}$ and $\mathbf{C}_{j_d,\hat{\Delta}_t}$ respectively
- Compute the initial coefficient vectors

$\hat{c}^{[0]}_{m_{j_d}} = \left(\mathbf{M}^T_{j_d,\hat{\Delta}_t}\mathbf{M}_{j_d,\hat{\Delta}_t}\right)^{-1}\mathbf{M}^T_{j_d,\hat{\Delta}_t}\hat{f}^{[0]}_m$ and
$\hat{c}^{[0]}_{c_{j_d}} = \left(\mathbf{C}^T_{j_d,\hat{\Delta}_t}\mathbf{C}_{j_d,\hat{\Delta}_t}\right)^{-1}\mathbf{C}^T_{j_d,\hat{\Delta}_t}\hat{f}^{[0]}_c$

- Step 3
  - Calculate optimisation window sizes $\Delta_{\phi_{j,k}}$ taking into account the extended time interval $\hat{\Delta}_t$
  - Fix $\hat{c}^{k_c}_{j_g}$ and obtain the optimal solution $\hat{c}^{k_m}_{j_g}$ by solving the nonlinear least-squares problem using the Levenberg-Marquadrant algorithm.
- Step 4
  - Update the translation parameter k. If $k \leq k_{max}$, set $k = k + 1$ and repeat step 3. Otherwise proceed to the next step.
- Step 5
  - Restart the sliding window position by setting $k = 1$
- Step 6
  - Fix $\hat{c}^{k_m}_{j_g}$ and obtain the optimal solution $\hat{c}^{k_c}_{j_g}$ by solving the nonlinear least-squares problem using the Levenberg-Marquadrant algorithm.
- Step 7
  - Update the translation parameter k. If $k \leq k_{max}$, set $k = k + 1$ and repeat step 3. Otherwise proceed to the next step.
- Finalisation
  - Recover the estimated gains in the original time interval Δ_t by deleting the extensions in $\hat{K}_m = \mathbf{M}_{j_g,\hat{\Delta}_t}\hat{c}_{m_{j_g}}$ and $\hat{K}_c = \mathbf{M}_{j_g,\hat{\Delta}_t}\hat{c}_{c_{j_g}}$ and

The algorithm was applied to recover the approximations of the gain functions of $K_m(t)$ and $K_c(t)$ using the following parameters in Step1, which correspond to the parameters used to obtain the adaptation gain for wild-type fly photoreceptors reported in (Friederich, 2011):

- Selected resolution level $j_d = 7$
- Optimisation interval $b_d = 385$ samples, 0.9625 seconds.

Table 4.2 Model Prediction Error(%) by Light Intensity Level Using Estimated Mean and Contrast Gains

Light Intensity	Estimated Gains	
	wild-type	hdcJK910
L_0	0.72022	0.61121
L_1	0.55867	0.55338
L_2	0.61479	0.34932
L_3	0.63848	0.37174

- Selected initial guesses $K_m^{[0]}(t) = K_c^{[0]}(t)$ shown in Fig. 4.7
- Function to build the 'dictionaries': Battle-Lemarie Scaling function of 3^{rd} order shown in Fig. 4.6

The estimated mean and contrast gain functions for wild and mutant flies are shown in Fig. 4.8, this Fig. reveals that there are clear differences between the mean and contrast gains of the wild-type fly and the mutant. In the case of the mutant fly, the mean gain adapts the stimulus slower than its wild counterpart. Also in the case of the contrast gain, the mutant fly is clearly lower for bright intensities, when compared to the contrast gain of the wild fly.

A comparison of the recorded experimental data against the model predicted output using the estimated mean and contrast gains is shown in Fig. 4.9. The prediction error by light intensity level in shown in Table 4.2.

4.4.3 Mean and Contrast Gain Control Model

This section introduces a two dynamic gain control model that continuously predict the mean and contrast gains $K_m(t)$ and $K_c(t)$ given the stimulus $u(t)$.

Each gain control model has the same structure as the gain control model presented in Fig. 4.1. Specifically, each gain control model has three parallel forward loops consisting of a linear filter block, a static nonlinearity and a saturation block as shown in Fig. 4.1.As a result the controller structure features dynamics on three different timescales which has been suggested (Friederich et al., 2016) that they could be related to adaptation mechanisms corresponding to calcium dynamics in the photoreceptor's rhabdomere (Hardie et al., 1993), pupil mechanism (Kirschfeld and Franceschini, 1969) and translocation of signalling proteins (Frechter and Minke, 2006).

The mean and contrast gains $K_m(t)$ and $K_c(t)$ are given by

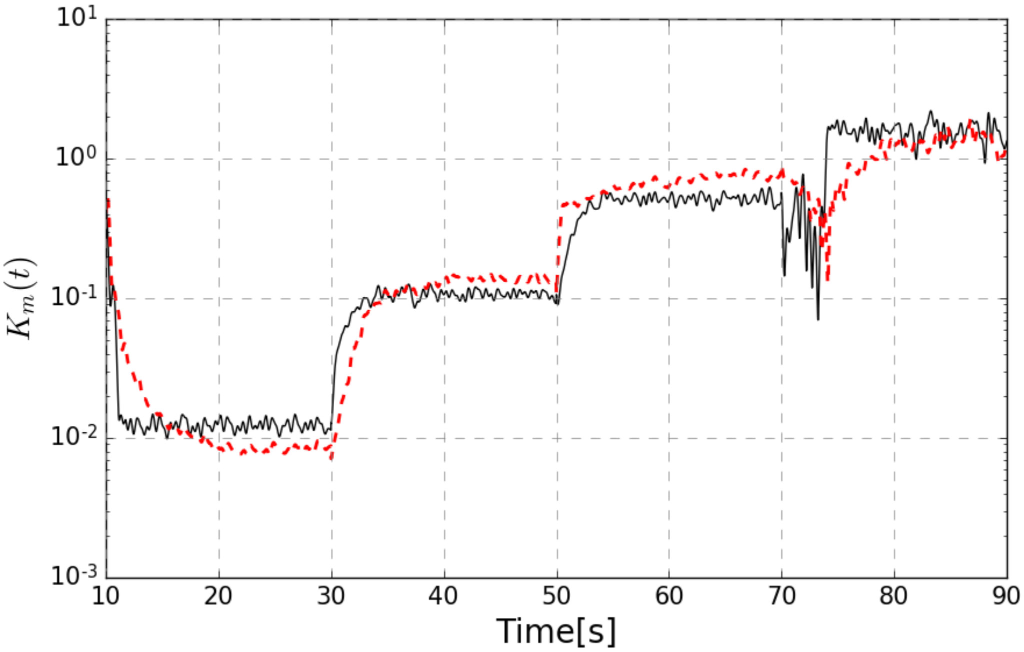

(a)

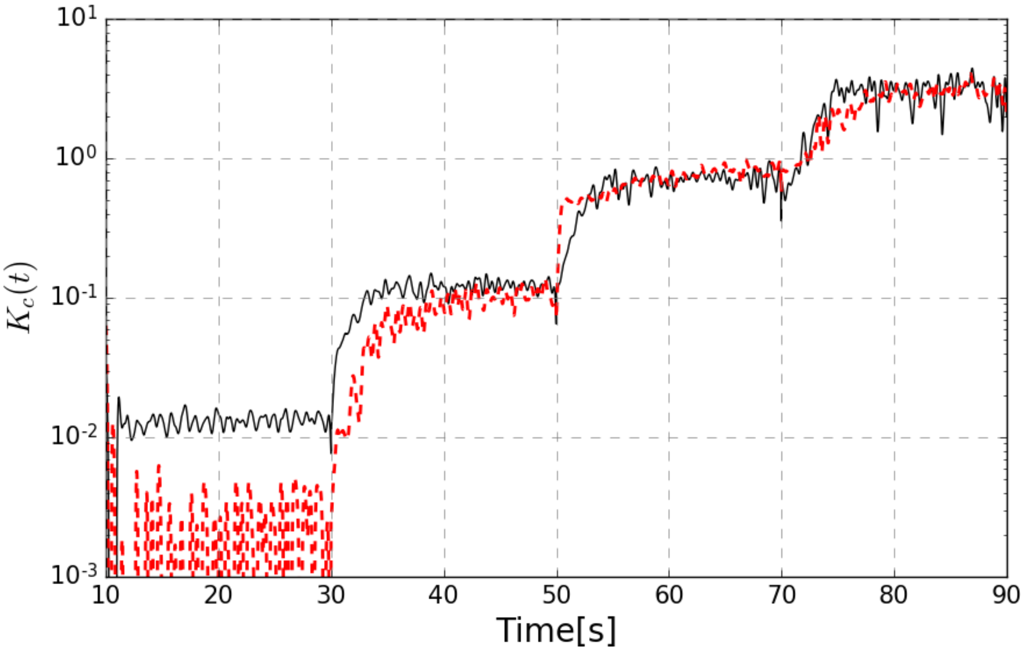

(b)

Fig. 4.8 Estimated (a) mean and (b) contrast gain functions for wild-type and mutant photoreceptors.

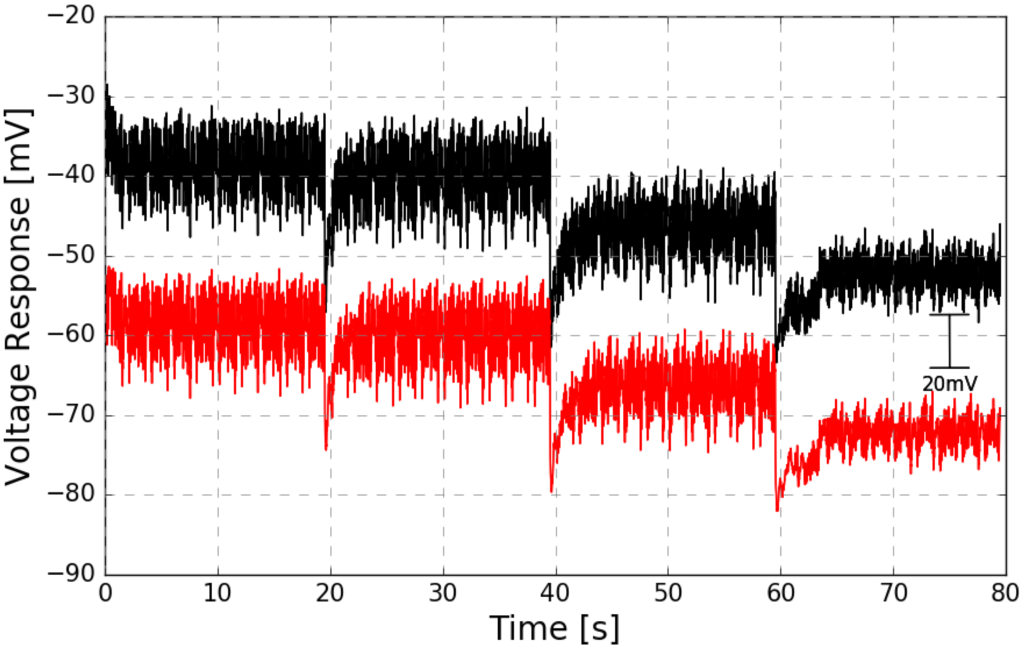

(a)

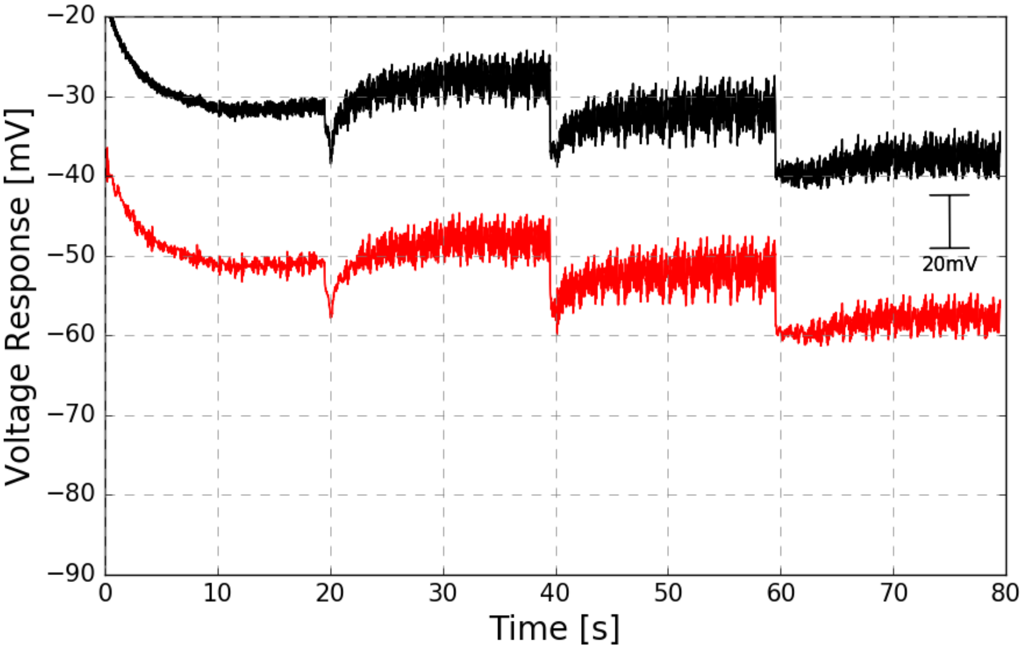

(b)

Fig. 4.9 Model validation, using the estimated mean and contrast adaptation gains, of wild and mutant photoreceptor responses to naturalistic stimuli. Fig. 4.9a shows the comparison between the *in vivo* photoreceptor recorded data (black) and the model prediction (red) for the wild fly. A similar comparison for the mutant fly is shown in Fig. 4.9b. Model predictions have been added an offset of -20mv.

$$K_m(t,u(t)) = \sum_{i=1}^{3} K_i^m(t,u(t)) \tag{4.28}$$

$$K_c(t,u(t)) = \sum_{i=1}^{3} K_i^c(t,u(t)) \tag{4.29}$$

where each $K_i^{m/c}(t,u(t))$ is composed of a cascade of the following three blocks:

- (L) A linear filter described as

$$\zeta_i \frac{d\bar{u}_i(t)}{dt} + \bar{u}_i(t) = u(t) \tag{4.30}$$

- (N) An inverting static nonlinearity defined by

$$g_i(t,u(t)) = \kappa_i \bar{u}(t)^{-\alpha_i} \tag{4.31}$$

The equation for $g_i(t)$ is

$$g_i(t,u(t)) = \kappa_i \big(\bar{g_0}_{,i} e^{-t/\zeta_i} + \frac{1}{\zeta_i}\int_0^t e^{-(t-\tau)/\zeta_i} u(\tau)d\tau\big)^{-\alpha_i} \tag{4.32}$$

- (B) And a saturation block

$$g'(t,u(t)) = \beta + \frac{g(t)-\beta}{1+e^{g(t)-\beta}} \tag{4.33}$$

Specifically the following parameter sets have to be estimated for the mean and contrast gain control models Explicitly for f_m the parameter set that needs to be estimated is defined as

$$\theta_i^m = [\zeta_{i_m}, \kappa_{i_m}, \alpha_{i_m}, \beta_{i_m}] \tag{4.34}$$

Similarly for f_c the parameter set that needs to be estimated is defined as

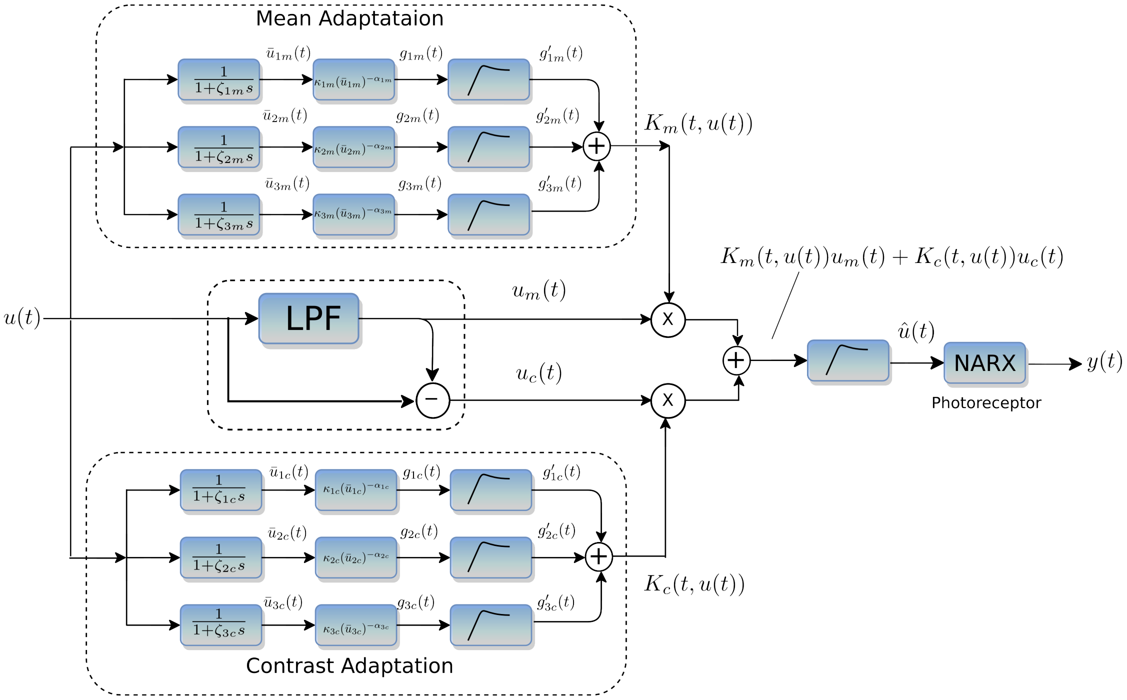

Fig. 4.10 Block diagram of the photoreceptor model incorporating separate mean and contrast gain control

$$\theta_i^c = [\zeta_{i_c}, \kappa_{i_c}, \alpha_{i_c}, \beta_{i_c}] \tag{4.35}$$

with $i = 1,2,3$

A global saturation function, (B) block

$$\hat{u}(t) = \beta_G + \frac{K_m(t,u(t))u_m(t) + K_c(t,u(t))u_c(t) - \beta_G}{1 + e^{K_m(t,u(t))u_m(t) + K_c(t,u(t))u_c(t) - \beta_G}} \tag{4.36}$$

Also is included to ensure the range of the input applied to the NARX model remains within the operating range of the model. This reflects the fact the signalling adaptation mechanisms in biological organisms have saturation limits.

The block diagram of the new model of the fly photoreceptor is illustrated in Fig. 4.10.

The complete parameter set

$$\theta = [\theta_i^m, \theta_i^c, \beta_G] \qquad i = 1, 2, 3 \tag{4.37}$$

Is determined by solving the following nonlinear optimisation problem

$$\hat{\theta} = \underset{\hat{\theta} \in \mathbb{R}}{\arg\min} \, \|z(t) - y(t)\|_2^2 \tag{4.38}$$

where $z(t)$ is the measured photoreceptor response, shown in Fig. 2.7(a), to the stimulus sequence $u(t)$, shown in Fig. 2.5. This optimisation problem was solved using the Levenberg(Levenberg, 1944)-Marquardt(Marquardt, 1963) algorithm.

The initial parameter vector,$\hat{\theta}$, was chosen to match the parameter reported in (Friederich, 2011) for the model of wild-type photoreceptor. The values are shown below

$$\theta_1^m(0) = \begin{bmatrix} \zeta_{1m} \\ K_{1m} \\ \alpha_{1m} \\ \beta_{1m} \end{bmatrix} = \begin{bmatrix} \zeta_{1c} \\ K_{1c} \\ \alpha_{1c} \\ \beta_{1c} \end{bmatrix} = \begin{bmatrix} 0.2175 \\ 3.3058 \\ 0.9328 \\ 45.2488 \end{bmatrix} \tag{4.39}$$

$$\theta_2^m(0) = \begin{bmatrix} \zeta_{2m} \\ K_{2m} \\ \alpha_{2m} \\ \beta_{2m} \end{bmatrix} = \begin{bmatrix} \zeta_{2c} \\ K_{2c} \\ \alpha_{2c} \\ \beta_{2c} \end{bmatrix} = \begin{bmatrix} 1.5774 \\ 0.7877 \\ 1.0256 \\ 490.42 \end{bmatrix} \tag{4.40}$$

$$\theta_3^m(0) = \begin{bmatrix} \zeta_{3m} \\ K_{3m} \\ \alpha_{3m} \\ \beta_{3m} \end{bmatrix} = \begin{bmatrix} \zeta_{3c} \\ K_{3c} \\ \alpha_{3c} \\ \beta_{3c} \end{bmatrix} = \begin{bmatrix} 14.6906 \\ 0.0195 \\ -1.7811 \\ 10000 \end{bmatrix} \tag{4.41}$$

$$\beta_G(0) = 13.2572 \tag{4.42}$$

Table 4.3 Parameters for the Mean and Contrast Gain Controllers of Wild-type and hdc^{JK910} Flies

Block		Mean		Contrast	
	Parameter	wild	hdcJK910	wild	hdcJK910
L_1	ζ	0.0787	8.2362	0.0316	1.0401
N_1	κ	0.0566	0.0074	0.000072309	0.000001
	α	4.6632	1.6953	6.5608	2.2093
B_1	β	27.0750	56.7017	29.5498	7000.0
L_2	ζ	0.7827	0.6017	1.1662	0.5000
N_2	κ	0.0292	0.0223	0.0302	0.0174
	α	0.8479	1.2385	1.0001	1.3445
B_2	β	1487.0	416.1900	4897.9	496.1481
L_3	ζ	18.3408	3.7080	0.5	1.7320
N_3	κ	0.00045623	0.0066	0.0000074097	0.00053922
	α	1.7907	1.1661	5.3591	1.7943
B_3	β	10000.0	2000.0	10000.0	3100.0

Table 4.4 Estimated Parameters of the Global Saturation Function for Wild and hdcJK910 Flies' Models.

Block	Parameter	Wild	hdcJK910
B	β_G	3.99	540

The values of the final parameter set, obtained after 50 iterations of the L-M algorithm are listed in tables 4.3 and 4.4.

The mean and contrast gains predicted by the estimated gain controllers are shown in Fig. 4.11 and 4.12 respectively.

Although the outputs of the gain controllers do not fit perfectly, the ultimate validation is provided by comparing the output of the complete photoreceptor model with experimental data.

4.5 Validation of the New Photoreceptor Models of Wild Type and Mutant Fruit Flies

The new photoreceptor models, derived for the wild- and mutant-type photoreceptors in the previous sections, are evaluated by comparing the model responses to the stimulus in Fig. 2.5.

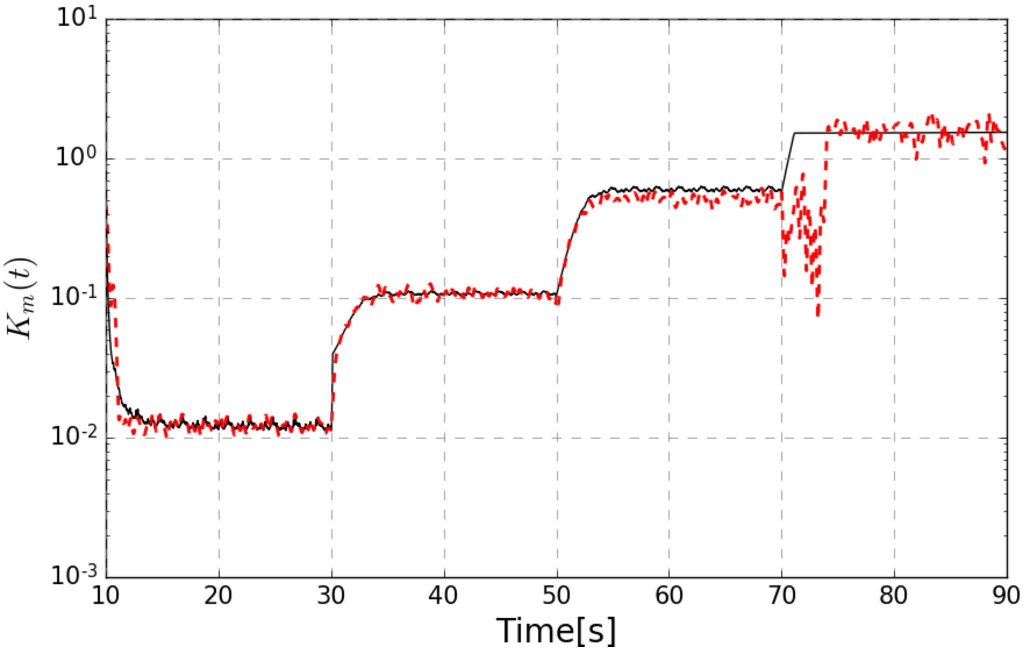

(a)

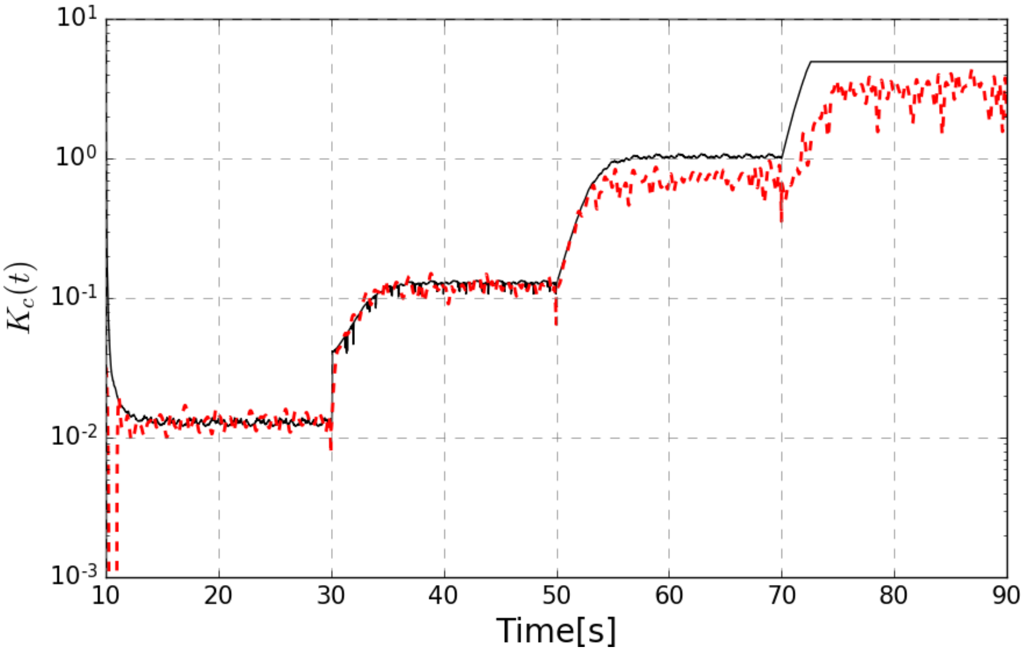

(b)

Fig. 4.11 Wild-type photoreceptor (a) mean and (b) contrast gain functions predicted by the gain control model (solid line) and estimated (dashed line) from data, corresponding to the input shown in Fig. 2.5.

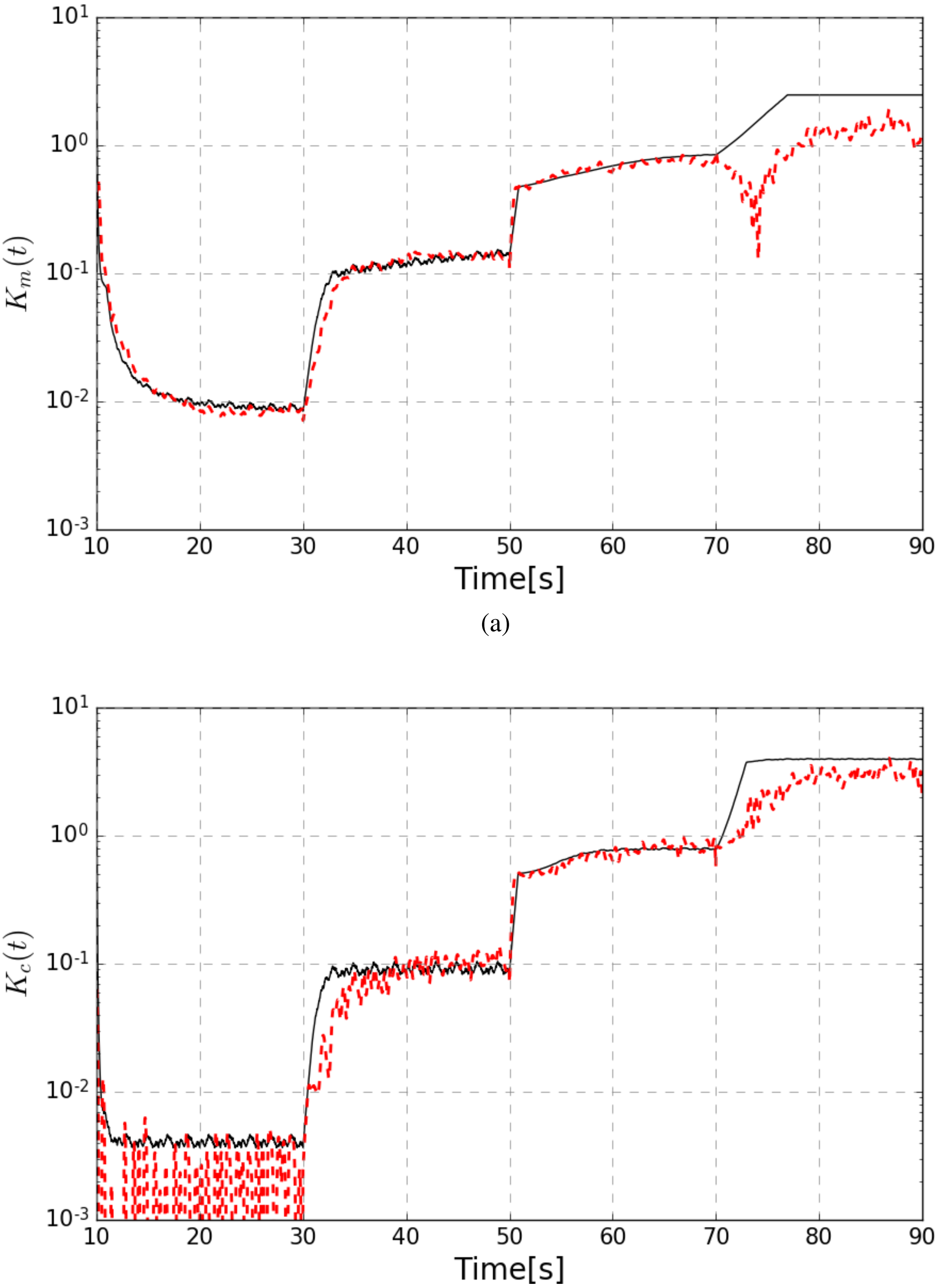

(a)

(b)

Fig. 4.12 Wild-type photoreceptor (a) mean and (b) contrast gain functions predicted by the gain control model (solid line) and estimated (dashed line) from data, corresponding to the input shown in Fig. 2.5.

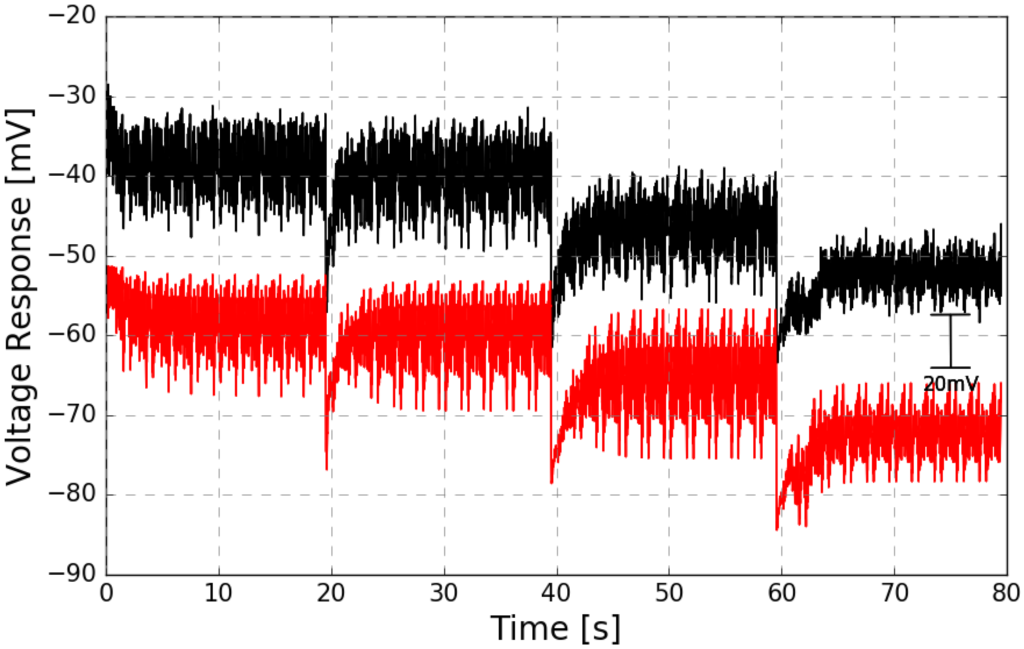

(a)

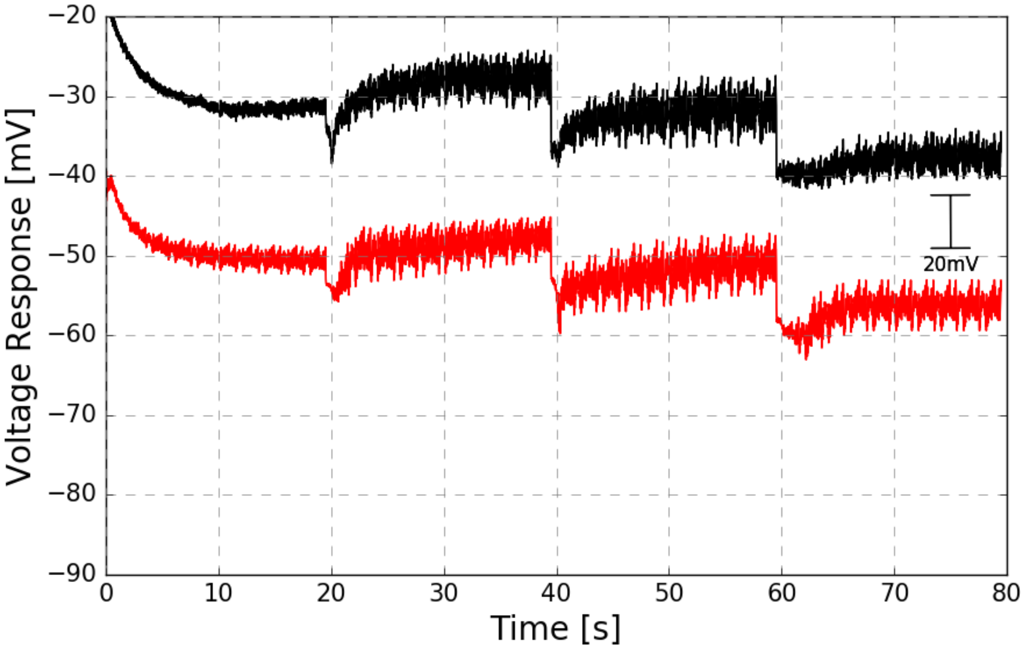

(b)

Fig. 4.13 Model validation, using the mean and contrast adaptation gains implemented with controller structure proposed in figure 4.10, of wild and mutant photoreceptor responses to naturalistic stimuli. Fig. 4.9a shows the comparison between the *in vivo* photoreceptor recorded data (black) and the model prediction (red) for the wild fly. A similar comparison for the mutant fly is shown in Fig. 4.9b. Model prediction has been added an offset of -20mv.

Table 4.5 Model Prediction Error(%) by Light Intensity Level

Light Intensity	Using Estimated Gains		Using Controller Gains	
	wild	hdcJK910	wild	hdcJK910
L_0	0.72022	0.61121	0.96558	1.22069
L_1	0.55867	0.55338	0.76480	0.93779
L_2	0.61479	0.34932	1.21488	0.60528
L_3	0.63848	0.37174	1.10665	1.47950

The response of the complete photoreceptor model, including the mean and contrast gain control model, is shown in Fig. 4.13.

Fig. 4.13a shows the comparison between experimental data and model predicted output for the case of the wild fly. The comparison for the mutant fly is shown in Fig. 4.13b. The model responses are in very good agreement with the experimental data.

Table 4.5 shows a summary of the model predictions using estimated and predicted gains. The results demonstrate that the new model of wild-type photoreceptor incorporating separate mean and contrast gains predicts photoreceptor responses to arbitrary stimuli as well as the original model incorporating a single gain parameter developed in (Friederich et al., 2016).

In addition, the new photoreceptor model structure allowed the estimation of a model for the mutant photoreceptor that achieves a similar level of accuracy.

4.6 Discussion

In this chapter the limitations of the previously developed empirical photoreceptor model (Friederich et al., 2016) in predicting the responses of histamine-deficient mutants were addressed by introducing a new model structure incorporating separate adaptation mechanisms for mean and contrast part of the stimuli. A comparative analysis of the model predicted mean and contrast gains for wild-type and histamine deficient flies, in response to a multilevel stimulus covering the entire environmental range suggested the role of the lamina in shaping the photoreceptor responses. The results showed that the brighter the stimuli the more important the role that the network of interneurons plays in shaping the response of the photoreceptors. Specifically, the comparison suggested that the LMC would help in speeding up the adaptation mechanism for adapting the mean of the stimulus and also it would also increase the amplitude of the contrast part of the stimulus.

The wild type model was validated using experimental data from 6 different flies. However, due to the data availability the model for the histamine deficient fly was estimated and validated using data only from one fly. Although this model could not be tested using other data sets as in the case of the wild-type model, the same model development approach was used which gives confidence that the mutant model is accurate. However, should more experimental data be available, the proposed methodology can be used to refine the model.

A limitation of the proposed model structure is that the feedback from the lamina is not modelled explicitly. For the wild-type model, this makes it difficult to discriminate between the signal processing at photoreceptor level and the contribution from the neurons in the lamina. Furthermore, the model does not capture explicitly between the photoreceptor and the lamina neuron making it impossible to use it to build a complete retinal circuit model of six photoreceptors and their post-synaptic neuron targets in the lamina and ultimately a complete retina model.

Chapter 5

An Empirical Model of Drosophila R1-6/LMC Retinal Network

5.1 Introduction

The interconnection between the lamina and retina in Drosophila has been studied in great detail. For instance, the electron-micrographs obtained in (Rivera-Alba et al., 2011) allowed the reconstruction of the photoreceptor-lamina network.

A schematic of the 'wiring' diagram is shown in Fig. 5.1(a) shows that there are feedforward and feedback connections between the photoreceptors in the retina and the network of interneurons hosted in the lamina. In the forward direction the information flows from PR1-PR6 of neighbouring ommatidia, which sample light information from the same point in space, mainly to large monopolar cells L1-L3 and amacrine cells α. There are also feedback connections from large monopolar cells L2, L4 and α amacrine to photoreceptors. The inhibitory feedforward pathway from the retina to the lamina is driven solely by histamine (Hardie, 1987, 1989; Sarthy, 1991). Whilst the excitatory feedback from lamina to the retina is glutamatergic and cholinergic (Hu et al., 2015; Kolodziejczyk et al., 2008; Raghu and Borst, 2011; Takemura et al., 2011).

Thanks to the genetic 'toolbox' available for Drosophila, it is possible to study the role of the network of interneurons in shaping the response of the photoreceptors. Suitable fly alleles have been used to study the effect of interrupting partially and enhancing communication from lamina to retina (Hu et al., 2015; Nikolaev et al., 2009; Zheng et al., 2006, 2009) as well as from retina to lamina (Dau et al., 2016). The outcome of those studies has demonstrated that the feedback from lamina to retina adjust the photoreceptor output actively by preventing saturation and increasing its SNR. Also, Dau et al. (2016) have shown that despite the fact that histamine deficient mutants hdc^{JK910}, i.e. blind flies, sample similar amounts of information when compared to their wild counterparts, there exists an overload in the interneurons which causes a tonic excitation that drives photoreceptors to high potentials and as a final consequence the operational range of photoreceptors is reduced.

Although the aforementioned studies have provided insight as to what is the role of interneurons in shaping the photoreceptor response, an explicit model that captures the dynamical behaviour of this interaction is not available. Having such a model would be very useful for at least two reasons. First, having a model that characterises explicitly the interconnection between retina and lamina can be coupled to existing models of neighbouring layers, retina, and medulla, would enable assembling in the long run a complete model of the early visual system of the fruit fly. Secondly, from a systems engineering point of view, such model would provide a basis for the role played by the interneurons in shaping the photoreceptor response.

This chapter introduces a new model that explicitly models the contribution of the network of interneurons, hosted in the lamina, in shaping the photoreceptor response.

The model exploits the dual, mean and contrast gain control architecture introduced in Chapter 4, which allows capturing with a single model architecture, the dynamic responses of mutant and wild-type photoreceptors. One limitation of the model developed in Chapter 4 is that the feedforward-feedback signalling between the photoreceptor and the lamina is not characterized explicitly. This means that the model cannot be used as a building block of a retina network model that involves interconnecting groups of six photoreceptors with LMC's and amacrine cells.

The Chapter is organised as follows. Section 1 revisits the model developed in the previous chapter and shows that in its current form that model is not suitable for explicitly modelling the lamina contribution towards the photoreceptor response. In section 2, by using a data-driven approach, a novel empirical model is introduced. This model explicitly exposes the contribution from the network of interneurons in the lamina to the photoreceptor. Section 3 the proposed model is validated using the collected electrophysiological data. Discussion and concluding remarks regarding the developed photoreceptor-LMC given in section 4.

5.2 Comparative analysis of photoreceptor models

The model introduced in Chapter 4 Section 4.1 with parameters tuned appropriately, can predict the response of photoreceptors to naturalistic stimuli over the entire environmental range, in wild-type as well as hdc^{JK910} mutant flies. However, neither the excitatory feedback

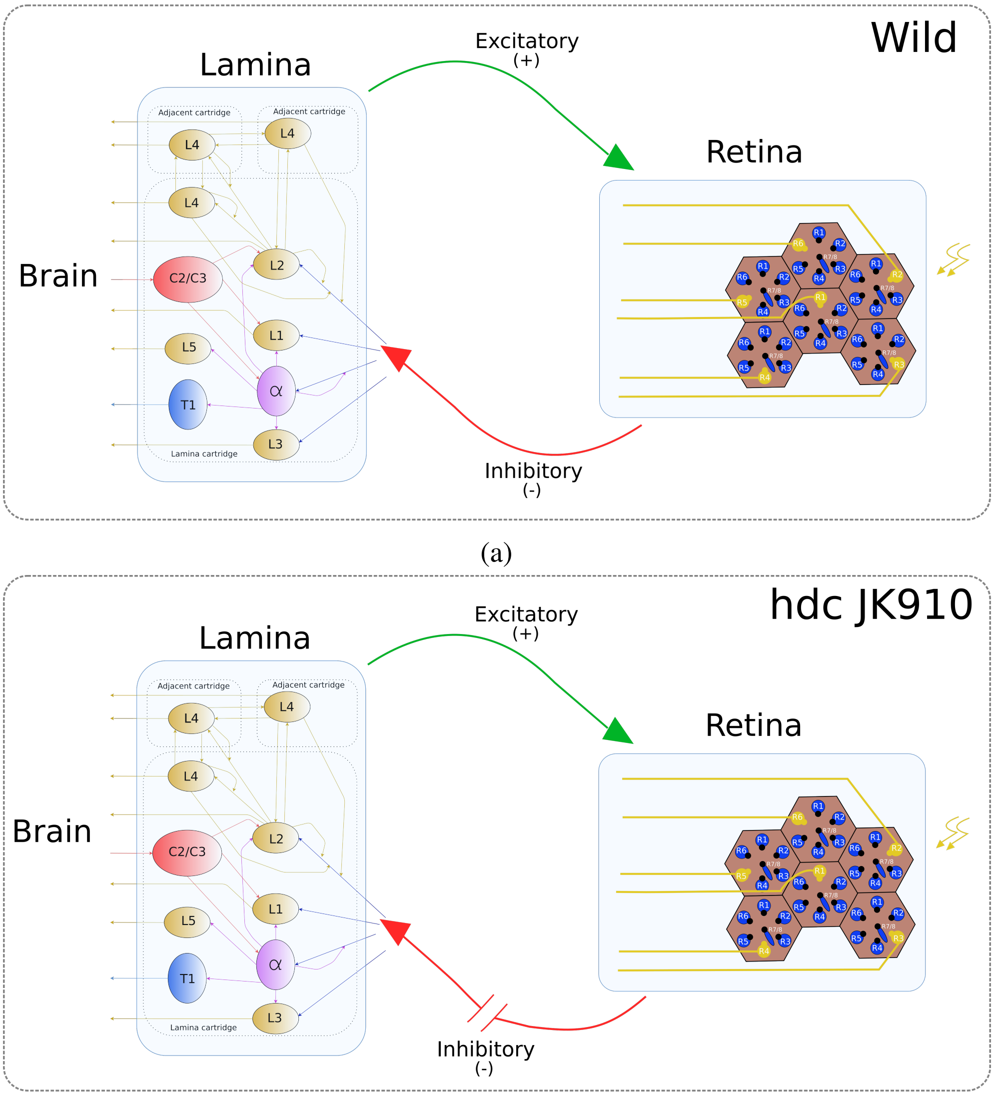

(a)

(b)

Fig. 5.1 Schematic of the connectome between the retina and lamina in Drosophila flies.

from lamina to retina nor the inhibitory feedforward from retina to lamina are modelled explicitly. This level of modelling detail is required to derive a retinal network model.

In this section, an analysis is carried out to compare the common and distinct components of the photoreceptor models of wild-type and mutant fruit flies derived in Chapter 4 Section 4.1, as a basis for modifying the structure of the model such that it accounts explicitly for the loss of connectivity with the lamina.

The NARX filter used to model the wild-type and hdcJK910 photoreceptor in the previous chapter share the same structure but with different parameter values, as shown in Tables 4.3 and 4.4. As a matter of fact, NARX/NARMAX models with different parameters could exhibit very similar dynamical behaviour.

One way to investigate dynamical equivalence of two NARX models is by comparing the model predicted responses of the two NARX models to a naturalistic stimulus sequence.

The two models were simulated using the naturalistic sequence shown in Fig. 2.5. Model predicted responses are shown in Fig. 5.2(a) and the difference between the predictions is shown in Fig. 5.2(b). The computed Normalised Mean Squared Error($NMSE(e(t))$), given by Equation 3.37 and where $e(t) = y(t)_{wild} - y(t)_{mutant}$, between the two different simulations is $NMSE(e) = 0.00175$. These results show that despite the difference in parameters, for a given naturalistic stimulus the predictions of the two NARX model are very similar.

An alternative way to compare the two photoreceptor models is by mapping them into the frequency domain. This comparison if the frequency domain is performed by computing the Generalised Frequency Response Functions (GFRFs) of each model. In order to show that the nonlinear transformations performed by the NARX filters of wild and hdcJK910 are very similar, the first and second order Generalised Frequency Response Functions (Billings and Peyton Jones, 1990; Billings and Tsang, 1989; Jones and Billings, 1989; Peyton Jones and Choudhary, 2012) were computed and compared. Since both NARX filters have the same structure so do their GFRFs. The analytical expressions that describe the first and second order GRFRs for both NARX filters are given by Equation 5.1 and Equation 5.2 respectively.

$$H_1(\Theta_1, \omega) = \frac{\theta_{15} e^{-j4\omega} + \theta_{14} e^{-j5\omega} + \theta_5 e^{-j6\omega} + \theta_7 e^{-j7\omega}}{1 - (\theta_1 e^{-j\omega} + \theta_2 e^{-j3\omega} \theta_9 e^{-j4\omega} \theta_{10} e^{-j5\omega})} \tag{5.1}$$

where $\Theta_1 = \{\theta_1, \theta_2, \theta_5, \theta_7, \theta_9, \theta_{10}, \theta_{14}, \theta_{15}\}$.

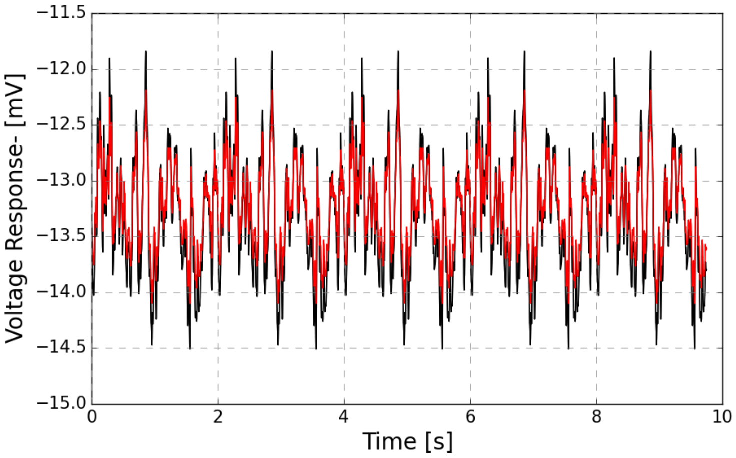

(a)

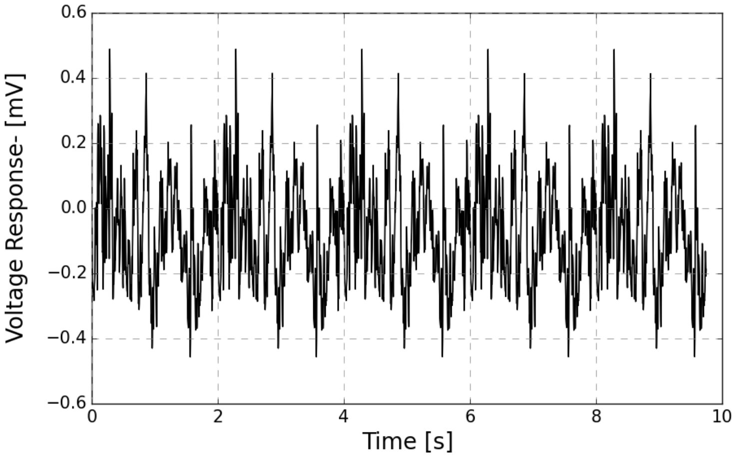

(b)

Fig. 5.2 (a) Comparison between predicted response of wild-type (black) and $\mathrm{hdc}^{\mathrm{JK910}}$(red) for a given naturalistic stimulus sequence, (b) difference between both model's prediction.

$$H_2(\theta_1,\cdots,\theta_{15},\omega_1,\omega_2) = \frac{1}{2}\frac{1}{\theta_1 e^{-j(\omega_1+\omega_2)} + \theta_2 e^{-j3(\omega_1+\omega_2)} + \theta_9 e^{-j4(\omega_1+\omega_2)} + \theta_{10} e^{-j5(\omega_1+\omega_2)}} \cdots$$

$$\cdots \begin{pmatrix} \theta_{13}\left(e^{-j(7\omega_1+3\omega_2)} + e^{-j(7\omega_2+3\omega_1)}\right) \\ \theta_3\left(e^{-j(5\omega_1+4\omega_2)} + e^{-j(5\omega_2+4\omega_1)}\right) \\ \theta_8\left(e^{-j(7\omega_1+6\omega_2)} + e^{-j(7\omega_2+6\omega_1)}\right) \\ \left(\theta_{12} e^{-j2\omega_1} + \theta_{11} e^{-j5\omega_1} + \theta_6 e^{-j6\omega_1}\right) H_1(\Theta_1,\omega_2) e^{-j4\omega_2} \\ \left(\theta_{12} e^{-j2\omega_2} + \theta_{11} e^{-j5\omega_2} + \theta_6 e^{-j6\omega_2}\right) H_1(\Theta_1,\omega_1) e^{-j4\omega_1} \end{pmatrix} \tag{5.2}$$

Table 5.1 Parameters of the NARX filters for Wild and hdc$^{\mathrm{JK910}}$ Photoreceptors

Terms	Parameter	wild-type	hdc$^{\mathrm{JK910}}$
$y(t-1)$	θ_1	0.876843	0.866998
$y(t-3)$	θ_2	0.026093	0.0675079
$u(t-4)u(t-5)$	θ_3	-175.143562	-91.284261
1	θ_4	-2.638715	0.024890
$u(t-6)$	θ_5	33.383327	8.174820
$y(t-6)u(t-4)$	θ_6	0.047841	-0.84112
$u(t-7)$	θ_7	21.277399	-1.290357
$u(t-6)u(t-7)$	θ_8	-318.269652	-77.972185
$y(t-4)$	θ_9	-0.169338	-0.098469
$y(t-5)$	θ_{10}	0.094975	0.023526
$y(t-4)u(t-4)$	θ_{11}	-0.159067	1.746027
$y(t-2)u(t-4)$	θ_{12}	-1.201824	-4.317250
$u(t-3)u(t-7)$	θ_{13}	-6.107486	222.325254
$u(t-5)$	θ_{14}	27.388775	15.975744
$u(t-4)$	θ_{15}	19.084409	55.934696

The computed magnitude and phase for the linear Generalised Frequency Response Functions of the two NARX photoreceptor are shown in Fig. 5.3. The parameters used in the models are shown in Table 5.1.

The first order Frequency Response Function is shown in Fig. 5.3. The magnitude is shown in Fig. 5.3(a). In order to compare the difference of the first order Frequency Response Functions the following measure was computed $\Delta_M H_1^{w,m} = ||H_1(\Theta_w,\omega) - H_1(\Theta_m,\omega)|| = 0.486$. Where Θ_w and Θ_m correspond to $\{\theta_1 \cdots, \theta_{15}\}$ for the wild and mutant NARX models respectively. This result quantifies a clear numeric difference between the two Frequency Response Functions, however Fig. 5.3 shows that the magnitude of wild and mutant first order

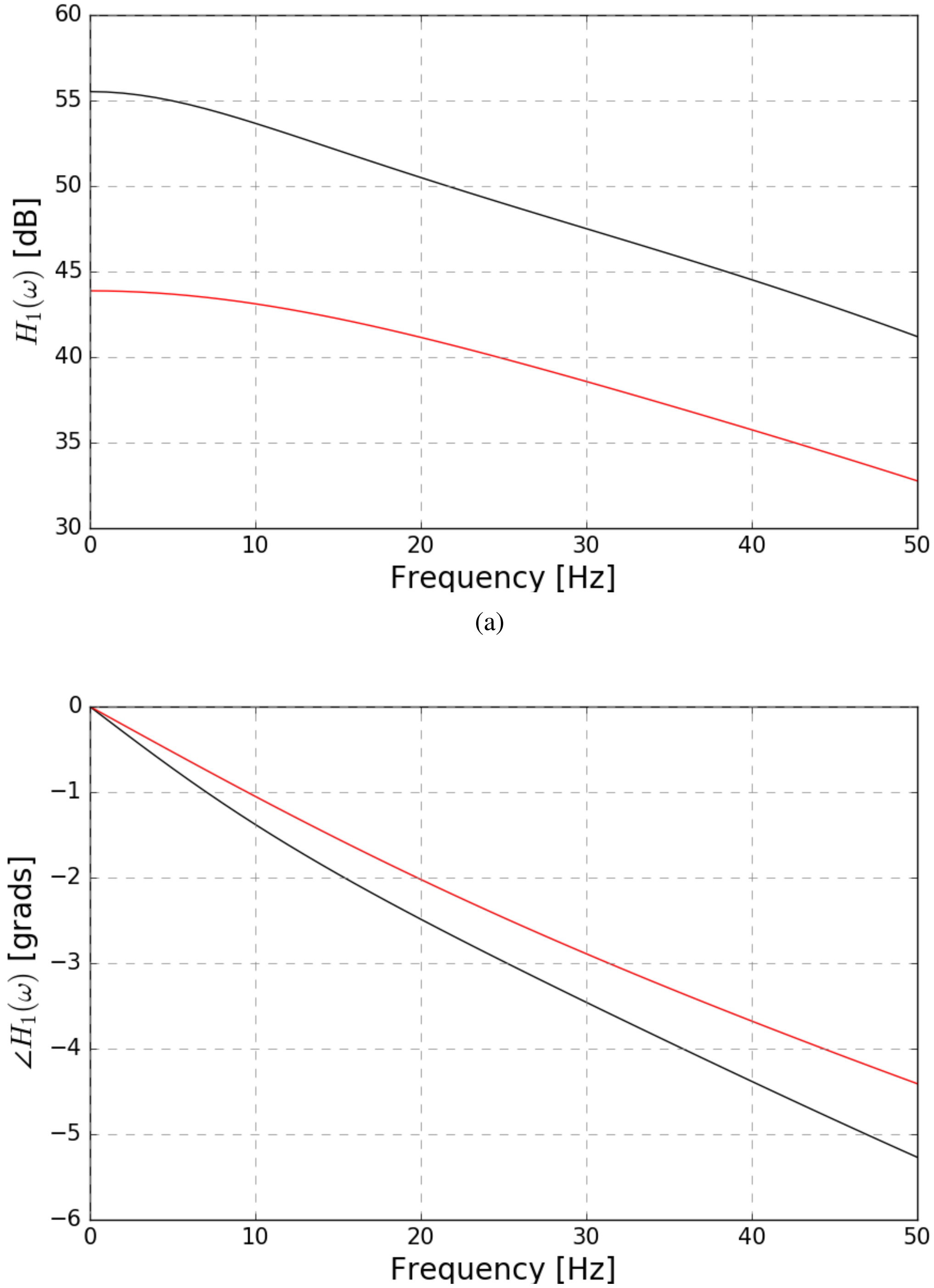

(a)

(b)

Fig. 5.3 First Order Generalised Frequency Response Functions. (a) Comparison between the magnitude of the wild-type (black) and mutant (red) NARX filters. (b) Comparison of the phase profile for the same two filters.

GFRF have a low-pass response. Also, their phases are shown in Fig. 5.3(b). To quantify the numeric difference between the phase of the two first order Frequency Response Functions the following quantity was computed $\Delta_P H_1^{w,m} = ||\angle H_1(\Theta_w, \omega) - \angle H_1(\Theta_m, \omega)|| = 0.02839$. This result indicates that there is a small difference between the two. These previous observations suggest that, whilst not having exactly the same magnitude and phase, the two filters have similar dynamical behaviour.

The surfaces corresponding to the second order GFRFs for wild-type and hdc$^{\mathrm{JK910}}$ NARX filters are shown in Fig. 5.4 and 5.5. Despite having a different magnitude surface, $\Delta_M H_2^{w,m} = ||H_2(\Theta_w, \omega_1, \omega_2) - H_2(\Theta_m, \omega_1, \omega_2)|| = 0.4023$, Fig. 5.4, show that wild and mutant NARX filters have a similar shape. This similarity in shape suggests a similarity in behaviour as well. The most important point, however, is the similarity, $\Delta_P H_2^{w,m} = ||\angle H_2(\Theta_w, \omega_1, \omega_2) - \angle H_2(\Theta_m, \omega_1, \omega_2)|| = 0.3667$, between the wild-type and mutant NARX filter phase surface. It is clear that the filters are sensitive to signals with structure in their phase. To have help assessing the similarities between the second order GRGF surfaces of wild and mutant NARX filter, the intersection between those surfaces and the planes $\omega_1 + \omega_2 = 1Hz$ and $\omega_1 + \omega_2 = 46Hz$ were computed and are shown in Fig. 5.6 in panels (a), (b) and (c), (d) respectively.

The comparative temporal and spectral analysis carried out indicates that the mutation has little effect on the NARX filter block and that, as noted in (Friederich et al., 2016), this block describes processes that take place at photoreceptor level, independently of contribution from the network of interneurons in the lamina. From a modelling point of view, this suggests that the architecture of the contrast and mean gain controllers needs to be modified in order to separate and characterize explicitly the adaptation processes that take place at photoreceptor level from those driven by the lamina.

5.3 A model of R1-6/LMC network

In this section a empirical model that explicitly exposes the contribution from the network of interneurons to the photoreceptors is introduced. The output of the model is defined as

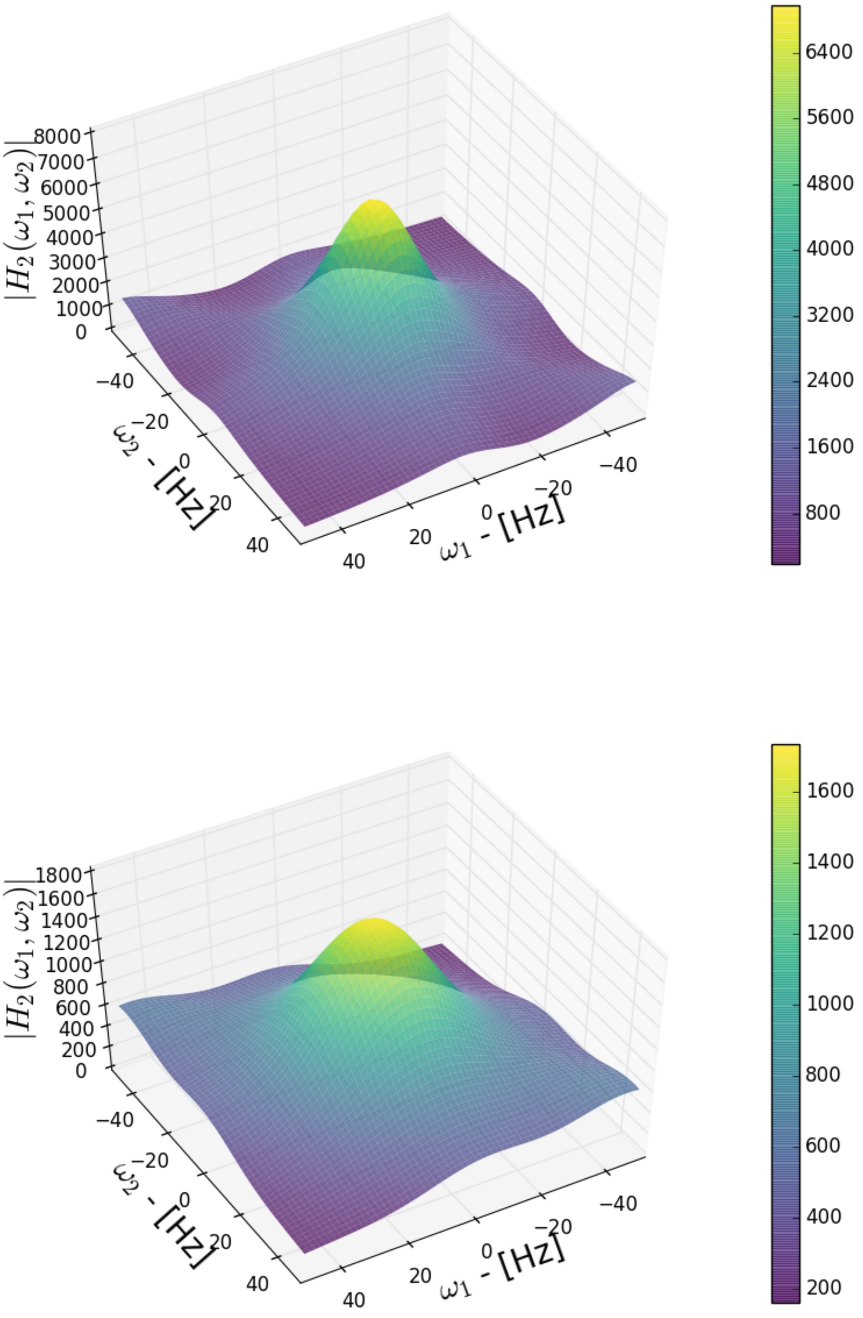

Fig. 5.4 Magnitude of the second-order GFRF of the (a) wild-type and (b) hdc^{JK910} NARX filters.

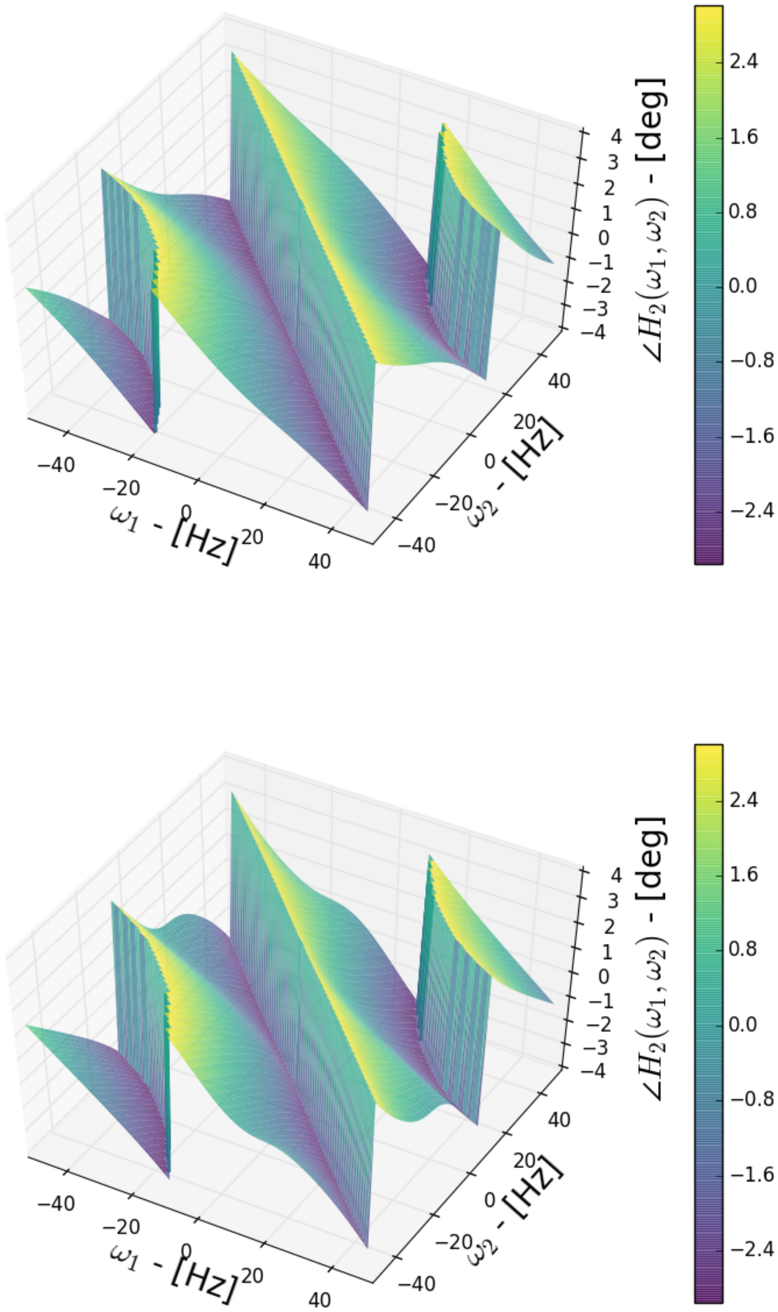

Fig. 5.5 Phase of the second-order GFRF of (a) the wild-type and (b) hdc$^{\mathrm{JK910}}$ NARX filters

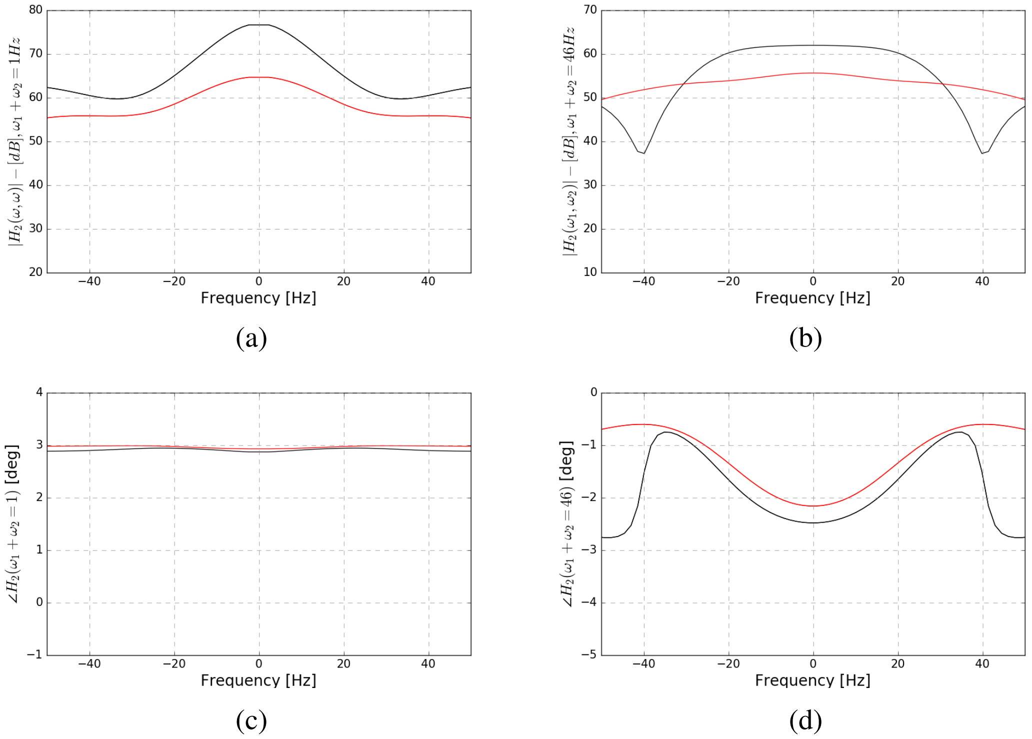

(a) (b)

(c) (d)

Fig. 5.6 Second-order GFRF along the planes $\omega_1 + \omega_2 = 1Hz$ (a) magnitude and (c) phase; and $\omega_1 + \omega_2 = 46Hz$ (b) magnitude and (d) phase. Wild- (black) and mutant-type(red) NARX models.

$$\begin{aligned} y_1(t) = {} & \theta_1 y_1(t-1) + \theta_2 y_1(t-3) + \theta_3 \hat{u}'_L(t-5)\hat{u}'_L(t-4) \\ & + \theta_4 + \theta_5 \hat{u}'_L(t-6) + \theta_6 \hat{u}'_L(t-4) y_1(t-6) \\ & + \theta_7 \hat{u}'_L(t-7) + \theta_8 \hat{u}'_L(t-7)\hat{u}'_L(t-6) \\ & + \theta_9 y_1(t-4) + \theta_{10} y_1(t-5) + \theta_{11} \hat{u}'_L(t-4) y_1(t-5) \\ & + \theta_{12} \hat{u}'_L(t-4) y_1(t-2) + \theta_{13} \hat{u}'_L(t-7)\hat{u}'_L(t-3) + \theta_{14} \hat{u}'_L(t-5) \\ & + \theta_{15} \hat{u}'_L(t-4) \end{aligned} \tag{5.3}$$

where $y_1(t)$ is the predicted voltage response of photoreceptor 1. And $\hat{u}'_L$ is given by

$$\hat{u}'_L(t, u(t)) = \beta + \frac{\hat{u}(t) - \beta}{1 + e^{\hat{u}(t) - \beta}} \tag{5.4}$$

with $\hat{u}$ described by the equation

$$\hat{u}(t, u(t)) = K_m(t, u(t)) u_m(t) L_m(t) + K_c(t, u(t)) u_c(t) L_c(t) \tag{5.5}$$

In the previous equation the $u_m(t)$ represents the mean component of the input stimulus sequence $u(t)$, and is defined by the equation

$$u_m(t) = 0.0011[u(t) + u(t-1)] + 0.8877 u_m(t-1) \tag{5.6}$$

The contrast component of the input stimulus sequence is given by

$$u_c(t) = u(t) - u_m(t) \tag{5.7}$$

where the adapted version of the mean part of the visual stimuli is given by

$$K_m(t, u(t)) = \sum_{i=1}^{3} K_i^m(t, u(t)) \tag{5.8}$$

Similarly the adapted version of the mean-removed visual stimuli is given by

$$K_c(t,u(t)) = \sum_{i=1}^{3} K_i^c(t,u(t)) \tag{5.9}$$

Similarly to the model in Chapter 4, each of the previous $K_i^{(\cdot)}$ is composed of a cascade of the next three blocks

- (L) A linear filter described as

$$\zeta_i \frac{d\bar{u}_i(t)}{dt} + \bar{u}_i(t) = u(t) \tag{5.10}$$

- (N) An inverting static nonlinearity defined by

$$g_i(t,u(t)) = \kappa_i \bar{u}(t)^{-\alpha_i} \tag{5.11}$$

The equation for $g_i(t)$ is

$$g_i(t,u(t)) = \kappa_i \big(\bar{g_{0,i}} e^{-t/\zeta_i} + \frac{1}{\zeta_i}\int_0^t e^{-(t-\tau)/\zeta_i} u(\tau) d\tau\big)^{-\alpha_i} \tag{5.12}$$

- (B) And a saturation block

$$g'(t,u(t)) = \beta + \frac{g(t)-\beta}{1+e^{g(t)-\beta}} \tag{5.13}$$

The Lamina contribution is given by the identified models $L_m(t)$ and $L_c(t)$. These models were obtained from experimental data using the NARMAX framework as described in the following section. $L_m(t)$ and $L_c(t)$ are described by the equations

$$\begin{aligned} L_m(t) = \theta_0^{L_m} + \theta_1^{L_m} L_m(t-1) + \theta_2^{L_m} L_m(t-2) \\ \theta_3^{L_m} y_{PR}(t-1) + \theta_4^{L_m} y_{PR}(t-2) \end{aligned} \tag{5.14}$$

And

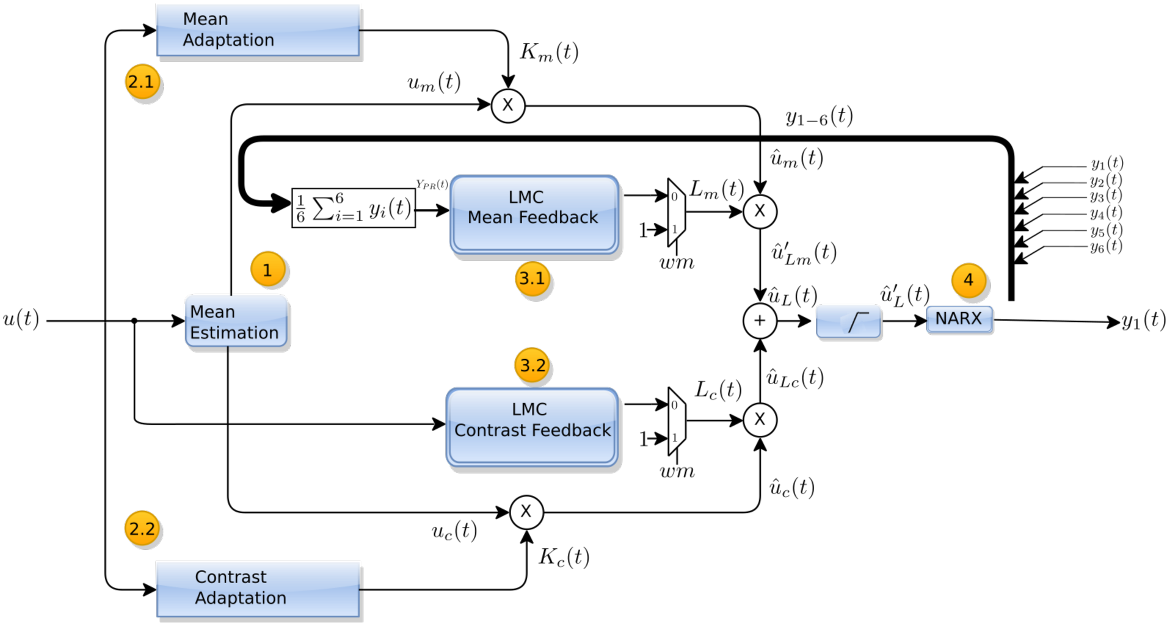

Fig. 5.7 Block diagram of the PR1-6/LMC model. The model structure is divided into four different stages.

$$\begin{aligned} L_c(t) = \theta_0^{L_c} + \theta_1^{L_c} L_c(t-1) + \theta_2^{L_c} L_c(t-2) \\ \theta_3^{L_c} u(t-1) + \theta_4^{L_c} u(t-2) \end{aligned} \tag{5.15}$$

respectively.

In equation 5.14, y_{PR} is defined as

$$y_{PR} = \frac{1}{6} \sum_{i=1}^{6} y_i(t) \tag{5.16}$$

A schematic of the previously introduced model is shown in Fig. 5.7

5.3.1 Empirical model of LMC

The previously introduced R1-6/LMC model is very similar to the model in Chapter 4, however, the key difference is that the contribution from the network of interneurones has been made explicit. The mathematical description of the proposed LMC model is given by Equations 5.14 and 5.15 which were obtained using the NARMAX framework, the details are given in the following paragraphs.

Both models $L_m(t)$ and $L_c(t)$ were obtained by solving a SISO system identification problem. After trying different combinations of possible inputs to estimate models for $L_m(t)$ and $L_c(t)$, $y_{PR}(t)$ and $u(t)$ were chosen. In particular, for $L_m(t)$ the selected input was $y_{PR}(t)$, shown in Fig. 5.8a, which was defined in Equation 5.16. Since the target sequence $L_m(t)$ was not known in advance, in this case it was defined as

$$L_m(t) := \frac{K_m(t)_{wild}}{K_m(t)_{mutant}} \tag{5.17}$$

where $K_m(t)_{wild}$ and $K_m(t)_{mutant}$ are the adaptation gains for the mean component of the stimulus for wild-type and mutant drosophila photoreceptors obtained in the Chapter 4 and which are described by Equation 4.28. A graphical representation of $L_m(t)$ is shown in Fig. 5.8c. The definition of $L_m(t)$ was made such that it would incorporate the difference in the mean adaptation gain between wild-type and mutant photoreceptors.

In the case of $L_c(t)$ the sequence used as input to solve the system identification problem is the full visual stimuli $u(t)$, shown in Fig. 5.8b. And the output, similarly to the previous case, was defined making use of the previously obtained adaptation gains of the mean-removed component of the wild-type and mutant photoreceptor models. Thus $L_c(t)$ is defined as

$$L_c(t) := \frac{K_c(t)_{wild}}{K_c(t)_{mutant}} \tag{5.18}$$

where $K_c(t)_{(\cdot)}$ is defined by equation 4.29. A graphical representation of $L_m(t)$ is shown in Fig. 5.8d. The definition of $L_c(t)$ is similar to Equation 5.17. This choice was made so that the difference in contrast adaptation gain between the wild and mutant photoreceptor models could be used as part of the new model.

The NARMAX methodology was used to solve both system identification problems. A polynomial expansion was chosen. After trying different parameters to run the system identification algorithm, the most suitable models for both $L_m(t)$ and $L_c(t)$ were simple ARX linear filters. The details for each model are given in Table 5.2 for $L_m(t)$ and 5.3 for $L_c(t)$.

The model predicted output of $L_m(t)$ and $L_c(t)$ when using as input naturalistic stimulation shown in Fig. 5.8b, are shown in Figs. 5.9a and 5.9c respectively. In the case of $L_c(t)$ the model predicted output is very close to $L_c(t)$ defined in equation 5.18. On the other hand, the model predicted output generated by the obtained empirical model of $L_m(t)$ shows a clear discrepancy when compared with the target $L_m(t)$ given by equation 5.17. Increasing the model complexity by obtaining models of higher order and including regressors with

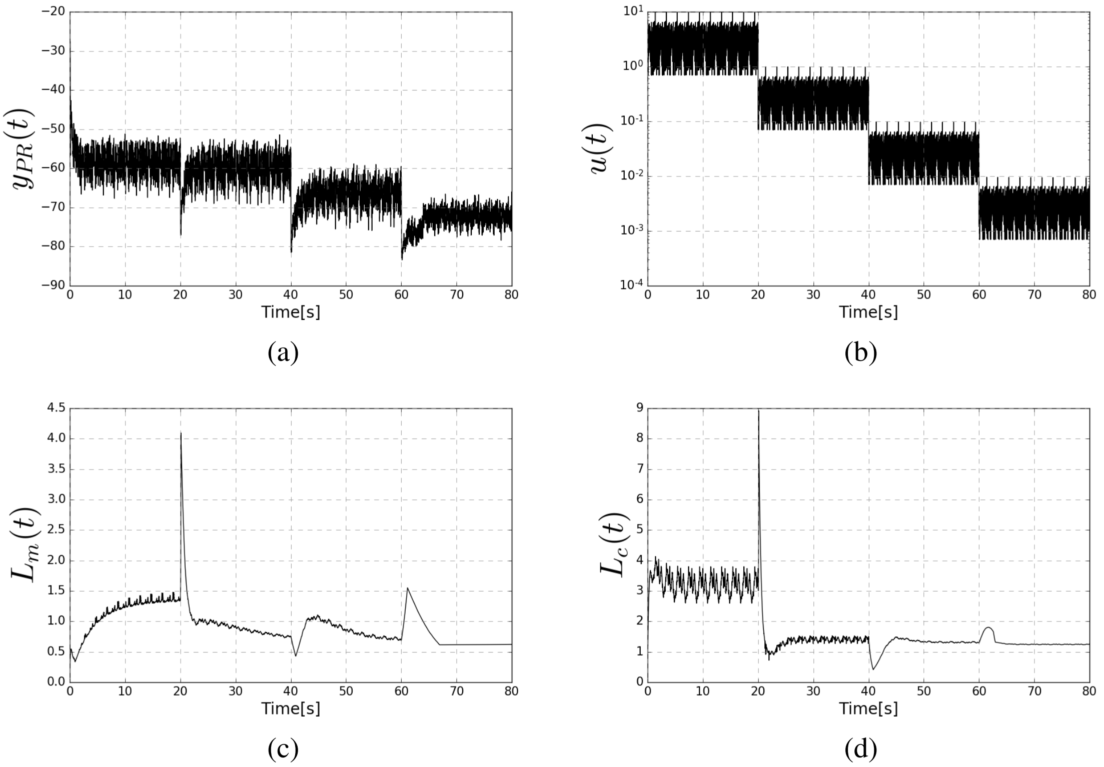

(a) (b)

(c) (d)

Fig. 5.8 Regressors used to obtain empirical models of $L_m(t)$ and $L_c(t)$. Input (a) and output (c) used as regressors for $L_m(t)$. Similarly panels (b) and (d) contain the input and output used as regressors for $L_c(t)$.

Table 5.2 Model of $L_m(t)$

Term	Parameter	Parameter value
constant	$\theta_0^{L_m}$	0.000267
$L_m(t-1)$	$\theta_1^{L_m}$	1.505937
$L_m(t-2)$	$\theta_2^{L_m}$	-0.506209
$y_{PR}(t-1)$	$\theta_3^{L_m}$	0.000301
$y_{PR}(t-2)$	$\theta_4^{L_m}$	-0.000302

more delays did not improve the model performance. However, notice that what is important for modelling the lamina contribution empirically, is the ability to compute $K_{(\cdot)}(t)_{wild}$ from $K_{(\cdot)}(t)_{mutant}$. Both can be obtained by using the definitions given in Equations 5.17 and 5.18 and the model predicted outputs obtained with the empirical models of the lamina, $L_m(t)$ and $L_c(t)$ given by Equations 5.14 and 5.15 it is possible to compute the wild-type adaptation gains $K_m(t)_{wild}$ and $K_c(t)_{wild}$ by computing $K_m(t)_{wild}L_m(t)$ and $K_c(t)_{wild}L_c(t)$ respectively. Fig. 5.9 shows the result of these computations, (b) $K_m(t)$ and (d) $K_c(t)$. In the Fig. 5.9 it can

Table 5.3 Model of $L_c(t)$

Term	Parameter	Parameter value
constant	$\theta_0^{L_c}$	0.003208
$L_c(t-1)$	$\theta_1^{L_c}$	1.469836
$L_c(t-2)$	$\theta_2^{L_c}$	-0.472435
$u(t-1)$	$\theta_3^{L_c}$	0.003669
$u(t-2)$	$\theta_4^{L_c}$	-0.001828

be seen that for high intensity levels which correspond to the first 20 seconds, both adapting gains were computed acceptably. For dimmer intensities $K_c(t)$ has a very good match in steady state. In the case of $K_m(t)$ there are discrepancies between desired and computed, both transient and steady state, nevertheless the main tendency is similar and acceptable in this case.

5.3.2 Numerical validation of the new photoreceptor model

The photoreceptor model was simulated and validated under two different scenarios. A complete model of retinal network in wild-type flies, incorporating the LMC feedback, and a model of the retinal network of histamine deficient mutants were simulated using the naturalistic input sequence in Fig. 5.8b and the results were compared with the respective experimental recordings.

In order to obtain the prediction of both the wild-type and mutant photoreceptors, the following configuration was selected. All the parameters used for the mutant photoreceptor model of chapter 4 were used in stages 1, 2 and 4 of the PR1-6/LMC model shown in Fig. 5.7. The only difference in the model configuration to obtain the wild-type or mutant is the value of the binary parameter wm, which controls the output of the two multiplexors shown in figure 5.7. In particular, to obtain the prediction for the mutant photoreceptor $wm = 0$ and to configure the model for the wild-type predictions then $wm = 1$.

Fig. 5.10 shows the comparison between the mutant photoreceptor experimental data and the model predicted output using the PR1-6/LMC model with $wm = 1$. The results demonstrate that the prediction is similar to the recorded data. In particular in this case, the prediction of the model PR1-6/LMC is identical to the one produced by the model in chapter 4 since the selected configuration performs the stimulus input adaptation without using the LMC empirical models. The comparison between the wild-type experimental data and the PR1-6/LMC model predicted output is also shown in panels (b) and (d) of the same figure. Although, the prediction is not perfectly matching the response is acceptable. Particularly

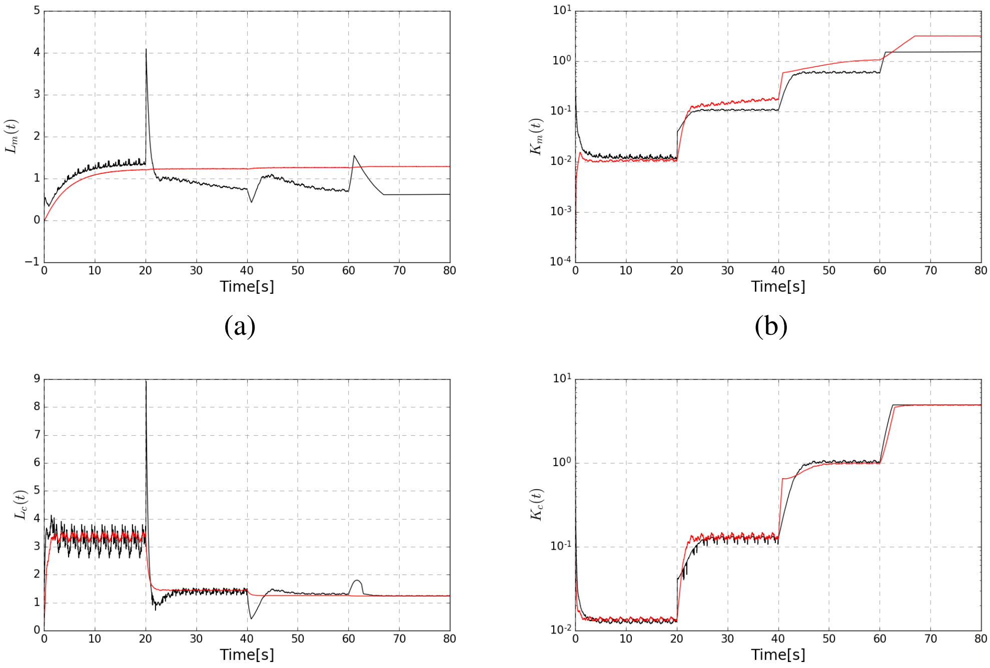

(a) (b)

(c) (d)

Fig. 5.9 LMC model predicted outputs. (a) comparison between the desired (black) and model predicted output (red) of $L_m(t)$. (c) comparison between desired (black) and model predicted(red) $L_c(t)$. (b) comparison between $K_m(t)$ obtained from definition (black) and computed(red), using LMC model. (d) comparison between $K_c(t)$ obtained from definition (black) and computed, using LMC model(red).

when taking into account that the greatest difference was shown in the first 20 seconds which correspond tor bright intensity light level, and the model shows a great improvement in that scenario.

5.4 Discussion and concluding remarks

In this chapter an empirical model that explicitly models the contribution of the lamina network of interneurons to photoreceptors was developed based on experimental intracellular recordings in wild-type and mutant hdc^{JK910}. In this model, the lamina plays the role of an additional gain compensator that helps the photoreceptor to adapt.

The model predicts the response of hdc^{JK910} and wild-type photoreceptors. In order to switch between wild- or mutant- type predictions only a single binary parameter *wm*, part of the model needs to be changed from 0 to 1 respectively.

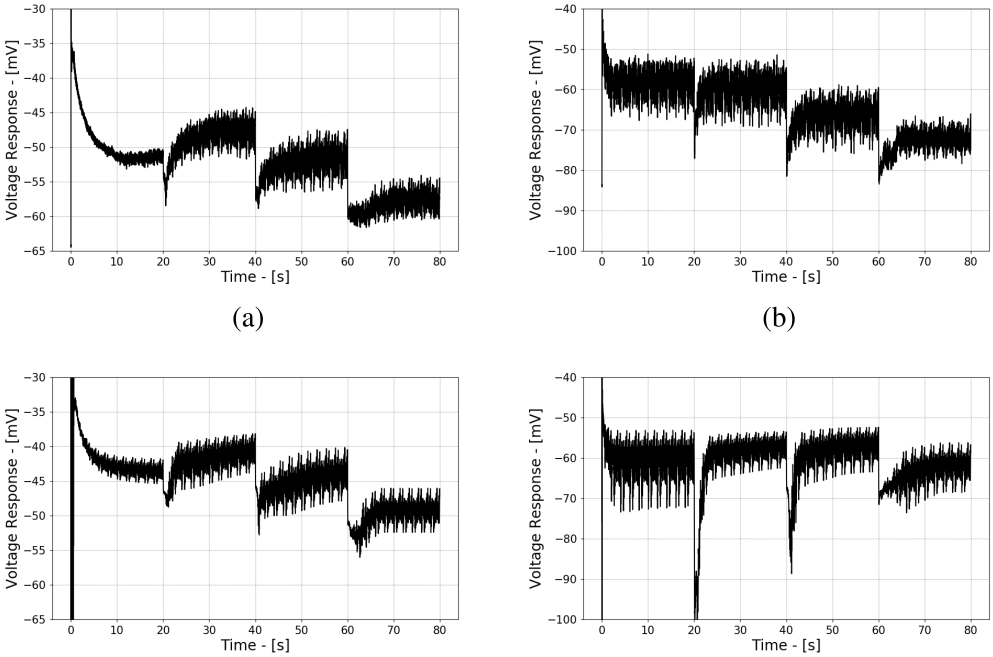

(a) (b)

(c) (d)

Fig. 5.10 PR1-6/LMC numerical validation for hdc$^{\mathrm{JK910}}$ photoreceptors. (a) Intracellular experimental data and (c) model predicted output from mutant hdc$^{\mathrm{JK910}}$ flies to naturalistic stimulation. Similarly, (b) intracellular experimental data and (d) model predicted output for wild-type flies to naturalistic stimulation.

This LMC model was estimated using the NARMAX methodology. The input-output data was derived from the experimental recordings in both mutant and wild flies. The mean and contrast adaptation gains were estimated from these data sets.

Also, the structure of the model developed in this chapter builds upon the structure used in the model presented in the previous chapter. The PR1-6/LMC model is capable of predicting the response of hdcJK910 and wild photoreceptors by just changing the value of the *wm* configuration 'knob' from $wm = 0$ to $wm = 1$.

While the developed model gives some insight into what the role of the network of interneurons might be in shaping the response at photoreceptor level, when using this model the following considerations need to be taken into account:

- PR1-6/LMC model validation. The contribution coming from the network of interneurons, $L_m(t)$ and $L_c(t)$, was modelled as two filters using the NARMAX methodology. Fig. 5.9 indicate that there is still some room for improvement in the model, this model refinement would require collecting additional data from more flies and perhaps lamina, which is out of the scope for this thesis.

- The model presented in this chapter does not separate the contribution of each interneuron in the lamina, but rather lump them all into a single entity. In the future the model could be refined by modelling the contribution of each interneuron hosted in the lamina cartridges individually.
- There is not a one-to-one relationship between the inhibitory-excitatory feedback suggested by the connectome and shown in Fig. 5.1 and the structure of the PR1-6/LMC model.

Despite these limitations the PR1-6/LMC model has a structure that explicitly explores the lamina contribution towards shaping the photoreceptor response. This fact enables the possibility of building up a model of the wiring diagram found in the actual animal which is composed of neighbouring ommatidia. These clusters, in turn, could be used as building blocks for a model of the full retina.

Chapter 6

The Role of Nonlinearity in Coding Biologically Relevant Features in Visual Stimuli

6.1 Introduction

It has been postulated that selectively detecting and enhancing biologically relevant features of stimuli is how sensory neurons process environmental information (Barlow, 2001, 1961). Recently Friederich et al. (2016), have demonstrated that fly photoreceptors exploit nonlinearity to enhance and encode local phase congruency information that could help the brain identify edges in visual scenes. They argue that nonlinear encoding in fly photoreceptors is optimised to maximise sensitivity to phase-aligned frequency components of visual stimuli and minimise the sensitivity to random phase signals. As shown in (Friederich et al., 2016), by simple thresholding of the nonlinear components of the responses of a photoreceptor to a naturalistic stimulus it is possible to reliably identify the edges in that stimulus even in the presence of noise.

This chapter uses information theory to characterise quantitatively the efficiency and robustness of the nonlinear coding scheme implemented by fly photoreceptors. The efficiency and robustness of linear and nonlinear photoreceptor coding of temporal edges is quantified by computing the rate-distortion functions, corresponding to linear and nonlinear components of the response, for a binary source using Hamming as the distortion measure.

The remaining of the chapter is organised as follows. In section two, the higher-order frequency response functions derived analytically from the photoreceptor model operating under constant mean/contrast gains are used to characterize quantitatively the nonlinear transformations that underpin encoding of phase aligned or coupled spectral components of temporal stimuli.

Section three presents a rate-distortion analysis of linear and nonlinear transformations implemented by photoreceptors given a binary source and a Hamming distortion measure.

The Conclusion section provides a summary of the results and their interpretation.

6.2 Analysis of linear and nonlinear transformations implemented by fly photoreceptors

It is well known that the response of sensory neurons to naturalistic stimuli is markedly different from the response to Gaussian white noise stimuli. Specifically, it has been shown (Juusola et al., 1994) that fly photoreceptors respond linearly to white noise stimuli and nonlinearly (Van Hateren and Snippe, 2001) to naturalistic stimuli.

Despite having a different parameter set, the photoreceptor models, i.e. the NARX filters, used in this thesis share the same structure as the model in (Friederich et al., 2016). In the following, it will be shown that the phase congruency detection properties of the photoreceptor model are preserved in the NARX filter used in this thesis.

The NARX models derived for wild-type and mutant flies at the light intensity level L-2, share the same model structure (have the same polynomial model terms) but different parameters.

The new photoreceptor model derived in Chapter 4, Section 5 employs the NARX model derived from electrophysiological recordings in mutant fruit flies.

In (Friederich et al., 2016) it is argued that the nonlinear mechanisms that are sensitive to phase correlations operate at the photoreceptor level and are captured by the NARX model block of the photoreceptor models for mutant and wild-type flies. To demonstrate this, the nonlinear coding properties of the two models are compared. This comparison is made by using the higher order frequency response functions of each model. These functions were derived analytically using Equation 3.43. In addition to using these functions, a spectral and temporal decomposition of the photoreceptor response to different synthetic stimuli was used. This decomposition was done using Equation 3.43 and Equation 3.49

Most of the analysis performed in this chapter uses the response of the full response of the photoreceptor model, as well as the linear and nonlinear, parts of the response.

In order to decompose the complete photoreceptor model response $y(t)$, for a given stimuli $u(t)$, into its linear $y_1(t)$ and nonlinear $y_2(t)$ parts the following procedure was followed.

1. Define the input sequence $u(t)$ used to drive the photoreceptor model. The photoreceptor response to this input will be decomposed into linear and nonlinear components.

2. Compute the Fourier Transform $U(j\omega)$ of $u(t)$.

3. Compute the linear frequency response as

   $Y_1(j\omega) = H_1(j\omega)U(j\omega)$, where $H_1(j\omega)$ is the first order Generalised Frequency Response Function defined in Equation 5.1.

4. Compute the time domain linear response $y_1(t)$ by applying the inverse Fourier Transform to $Y_1(j\omega)$.

5. Compute the frequency domain representation of the nonlinear response $Y2(j\omega)$ by computing

   $Y_2(j\omega) = \frac{1/\sqrt{(2)}}{2\pi} \int_{\omega_1+\omega_2=\omega} H_2(j\omega_1)(j\omega_2)U(j\omega_1)U(j\omega_2)d\sigma_{2\omega}$,

   where $H_2(j\omega_1)(j\omega_2)$ is the second order Generalised Frequency Response Function defined in Equation 5.2. In order to evaluate this integral properly a spectral characterisation of the input was performed and the frequencies of the input were then used to compute the frequency range of $Y_2(j\omega)$ using the algorithm presented in (Wei et al., 2007).

6. Compute the time domain second order response $y_2(t)$ by applying the inverse Fourier Transform to $Y_2(j\omega)$.

It is important to note here the photoreceptor response is approximated only in terms of the first- and second-order response since the contributions from higher-order components are negligible (Friederich, 2011). Thus higher order nonlinearities play no role in this model. Due to this assumption in all the discussion related to model responses second order response and nonlinear response are equivalent.

A stimulus sequence $u_{QPC}(t)$, a synthetically generated signal with 10Hz quadratically phase coupling (QPC), i.e. phase(f1) + phase(f2)=phase(f3), was used to compare the role played by nonlinearity in encoding global phase correlations. As reported in (Friederich et al., 2016) the $u_{QPC}(t)$ stimuli was constructed taking the inverse Fourier transform of a Gaussian white noise that had its spectrum modified such that it would satisfy the conditions for phase coupling at 10Hz, whilst maintaining the same magnitude of the unaltered Gaussian white noise.

The relevant time and frequency features of u_{QPC} are shown in Fig. 6.1. By inspecting panel (c) is clear that there is a phase coupling at 10Hz.

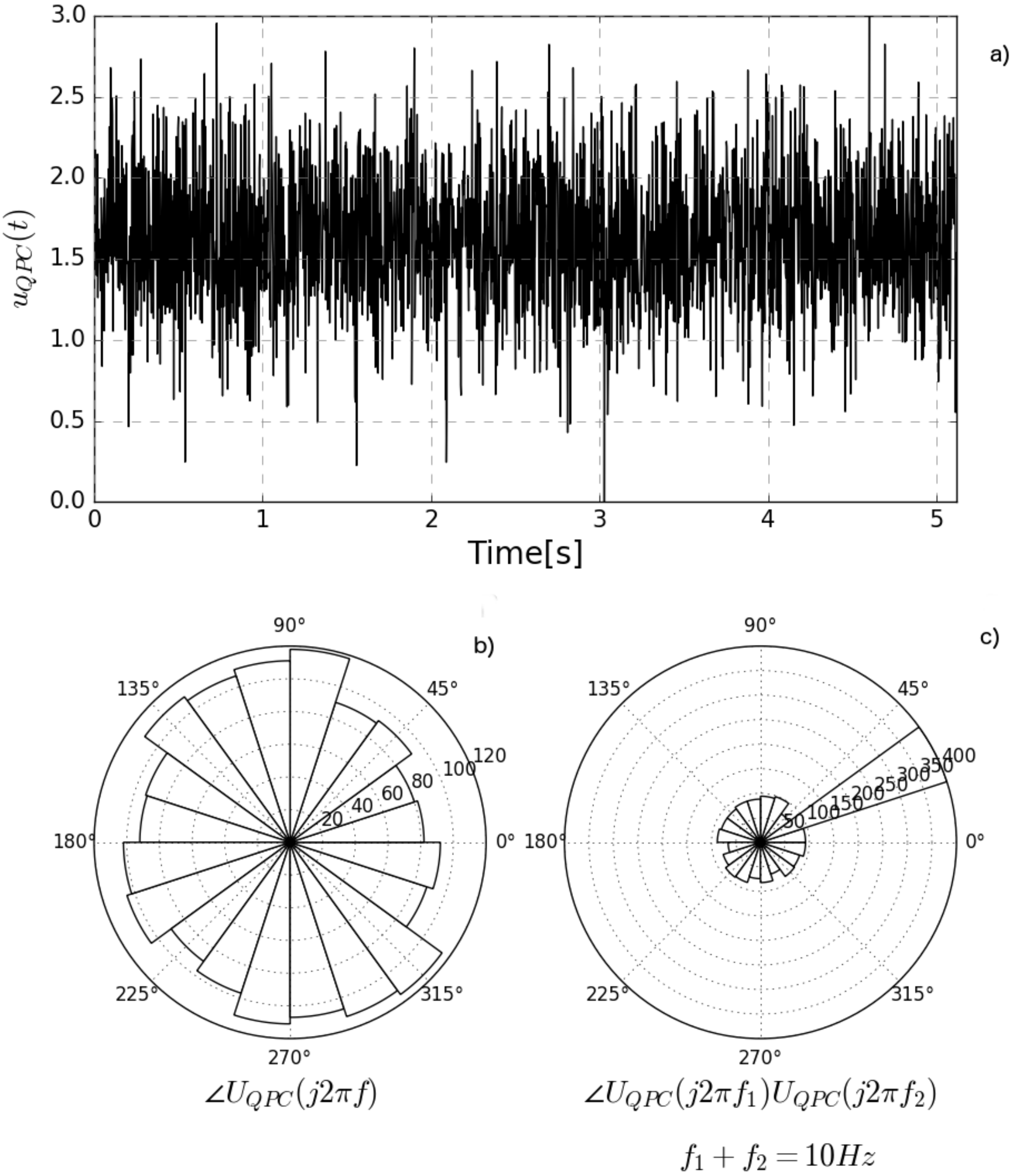

Fig. 6.1 Quadratically Phase Coupled Stimulus. Panel (a) contains the phase modified Gaussian noise stimulus $u_{QPC}(t)$, which exhibits quadratic phase coupling at 10Hz. . Panels (b) and (c), show the phase angle histograms of $U_{QPC}(j\omega)$.

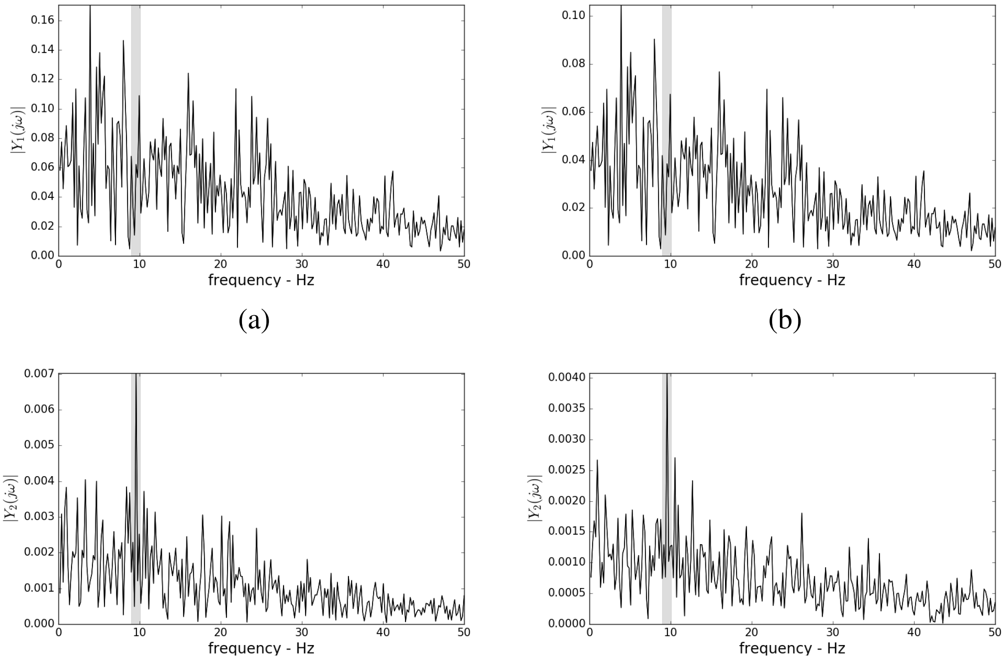

(a) (b)

(c) (d)

Fig. 6.2 Quadratic phase coupling detecting by wild- and mutant- type fly photoreceptor hdcJK910 photoreceptors. Magnitude spectra of wild- and mutant- type flies is shown in (a) and (b) for the linear response and (c) and (d) for the second-order response respectively.

The predicted response of the wild and mutant NARX photoreceptors's filters to u_{QPC} stimulus, were used to obtain their linear and nonlinear(second-order) responses in the frequency domain. The linear and nonlinear responses were obtained applying Equation 3.49. The result of this decomposition is shown in Fig. 6.2. Panels (a) and (b) show the spectrum of the linear response of the wild and mutant NARX filters respectively. As expected, there is no indication of the presence of a signal with QPC at 10Hz. On the other hand, the spectrum of the second-order response, for the wild and mutant, panels (c) and (d) respectively; clearly show a component with a large magnitude around the 10Hz frequency, which indicates the sensitivity to the phase structure of the stimulus.

In order to compare the role played by nonlinearity in encoding local phase congruency, the stimulus sequence consisting of a sequence of pulses superimposed in Gaussian white noise with mean L-0, (Friederich et al., 2016) was used in the analysis. A fixed bright stimulus was used so the gain control remains constant and adaptation plays no role.

Panel (a) of Fig. 6.3 show the stimulus to test local phase congruency. The predicted photoreceptors responses for wild- and mutant- type flies were computed and decomposed into their linear panels (b) and (c) and nonlinear panels (d) and (e) components, using Equations 3.43 and 3.49. From the figures it is clear that using the nonlinear response of either the wild- or mutant- type photoreceptors would be far easier to identify the location of the sequence of pulses that were embedded in noise, than using their linear response.

From the results presented in this section, it can be concluded that the NARX filters used in the models of photoreceptors in wild-type and mutant flies, described in Chapter 4, section 4.1 implement very similar linear and nonlinear transformations of the stimuli. This suggests that the phase congruency detection properties reported in (Friederich et al., 2016) take place entirely at photoreceptor level, i.e. the feedback from the network of interneurons plays no role for this purpose.

6.3 Rate-Distortion Analysis of R1-R6 Photoreceptors

Previous studies have characterised information processing in fly photoreceptors using algorithms based on information theoretical tools and concepts. In (Van Steveninck and Laughlin, 1996) an algorithm that allows the computation of the rate of information transfer between the photoreceptors in the retina and the large monopolar cell in the lamina of blowfly *Calliphora* was introduced. The algorithm is the first one in being able to compute the transfer rate of graded-potential synapses. This algorithm has the limitation that assumes Gaussian stimulation with additive Gaussian noise. A more recent study (Juusola and de Polavieja, 2003) introduced a new way of measuring the information transfer rate which does not make

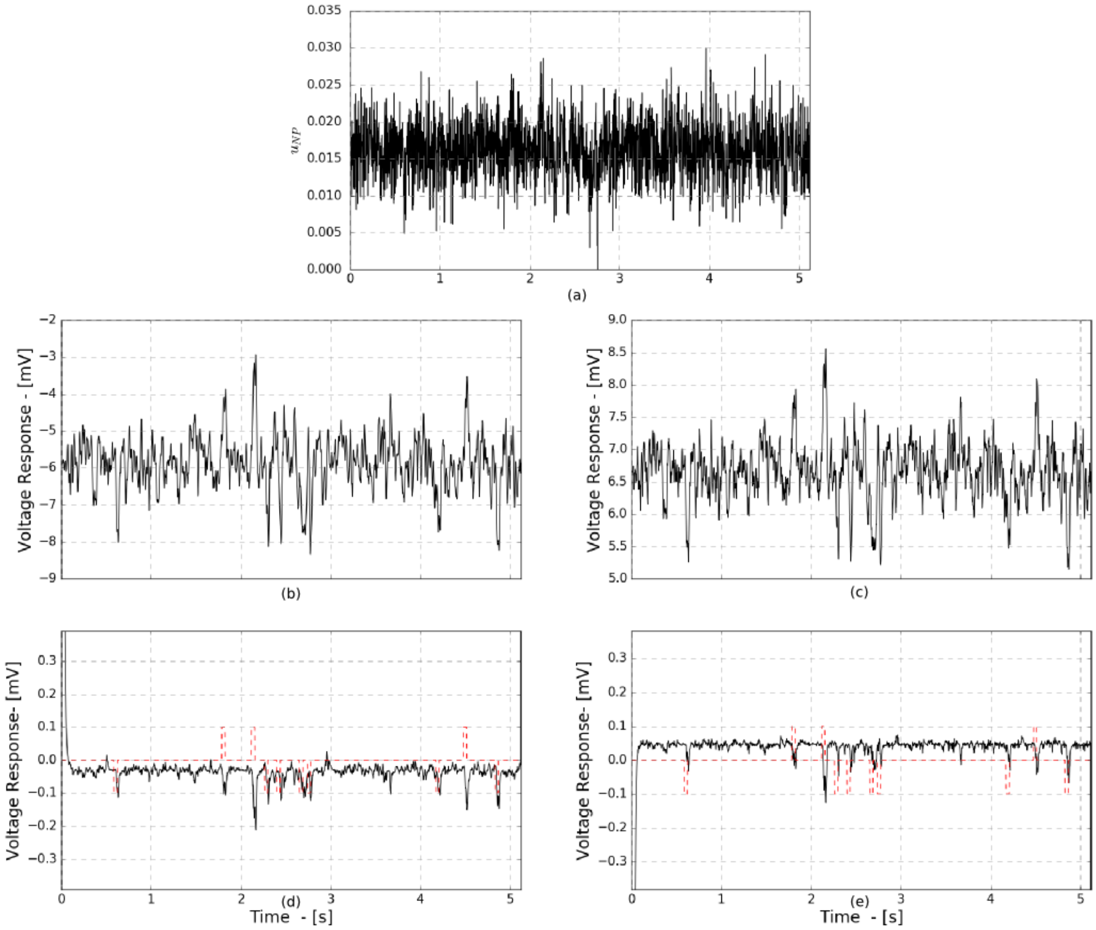

Fig. 6.3 Local phase congruency detection in fly photoreceptors. (a) Stimulus consisting of a sequence of pulses superimposed with white noise. First-order (linear) component response of the wild- and mutant- type flies are shown in (b) and (c) respectively. Second-order component of the response for wild- and mutant- type flies are shown in (d) and (e) respectively. Pulses embedded in the stimulus are shown with a dashed red line.

any assumptions about the input stimuli or noise, however, errors due to the extrapolation to the infinite limit of finite parameters could occur. In addition to the previous two studies Takalo et al. (2011) introduced a novel robust algorithm to estimate the information transfer rate of continuous signals. In the presented algorithm the use of principal component analysis is a key step for the robustness of the estimation.

In this chapter a new way of estimating the information processing capabilities of fly photoreceptors using the recently reported phase-congruency detection properties (Friederich et al., 2016) and rate-distortion(R-D) theory is proposed.

Define the pair of random processes $(S^N, \hat{S}^N)$ as the source, and estimated sequences where N is the number of random variables of each random process. Also, the i^{th} realisation of the pair of random processes is given by $(S_i^N, \hat{S}_i^N)$ with $S_i^N \sim B(p)$.

$$\begin{aligned}
y(t) = {} & \theta_1 y(t-1) + \theta_2 y(t-3) + \theta_3 s(t-5)s(t-4) \\
& + \theta_4 + \theta_5 s(t-6) + \theta_6 s(t-4)y(t-6) \\
& + \theta_7 s(t-7) + \theta_8 s(t-7)s(t-6) \\
& + \theta_9 y(t-4) + \theta_{10} y(t-5) + \theta_{11} s(t-4)y(t-5) \\
& + \theta_{12} s(t-4)y(t-2) + \theta_{13} s(t-7)s(t-3) + \theta_{14} s(t-5) \\
& + \theta_{15} s(t-4)
\end{aligned} \tag{6.1}$$

The predicted output, by the NARX model described by Equation 6.1 part of the photoreceptor model, when stimulated with S^N is defined as a random process Y^N.

In order to be able to compare the R-D feature profile of the NARX model against a theoretical bound, the source and estimated sequences are binarised using the following algorithm

Binarisation Algorithm

1. Obtain the mean of the sequence $\mu_x(t) = \frac{1}{N}\sum_{i=0}^{N-1} x(t_i)$
2. Remove the mean from the sequence $\bar{x}(t) = x(t) - \mu_x(t)$
3. Binarise the signal according to

$$\hat{x}(t) = \begin{cases} 0 & \text{if} \quad \mu_x(t) - \beta \leq x(t) \leq \mu_x(t) + \beta \\ 1 & \quad\text{elsewhere} \end{cases} \tag{6.2}$$

$$\beta := \mathbf{th} \times \alpha$$

$$\alpha := max(\bar{x}(t)) - min(\bar{x}(t))$$

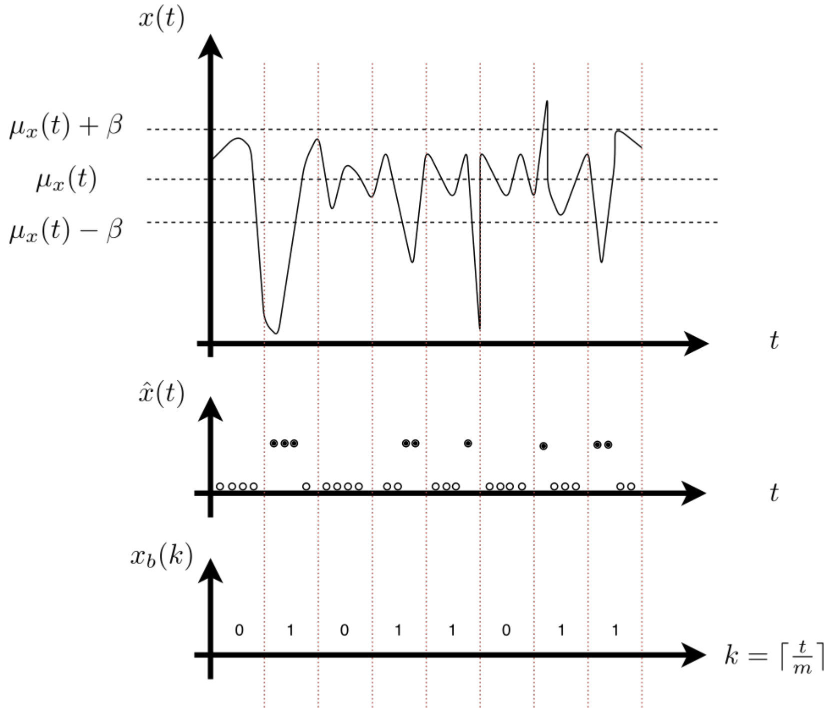

Fig. 6.4 Illustration of the *Binarisation Algorithm*

where **th** is a hyperparameter selected according to the stimuli.

4. Perform a logical 'or' operation using m bits using the following equation

$$x_b(k) = \bigvee_{j=0}^{m-1} \hat{x}(k+j) \tag{6.3}$$
$$k = \{0, m, \cdots, m\lceil \frac{N}{m} - 1 \rceil\}$$

An example of transmitted source and binarised signal using the *binarisation algorithm* is shown in Fig. 6.4.

After applying the *binarisation algorithm* to the source and estimated sequences $(X^N, \hat{Y}^N)$ the binarised versions are obtained $(X_b^N, \hat{X}_b^N)$, where $Y_b := \hat{X}_b^N$.

The distortion D is defined, according to (Cover and Thomas, 2006), as

$$D = \frac{1}{N}\mathbb{E}\left[\sum_{i=1}^{N} \left(S_i - S_i^N(Y^N)\right)\right] \tag{6.4}$$

Similarly the rate R, as function of the distortion D, is defined as

$$
\begin{aligned}
&R:\mathbb{R}\rightarrow\mathbb{R}\\
&R(D)=\inf{}_{g(\hat{X}^N):\mathbb{E}[X^N-\hat{X}_N]\leq D}I(X^N;\hat{X}^N) \qquad (6.5)
\end{aligned}
$$

For a Bernoulli source with probability p the rate-distortion function is given by (Cover and Thomas, 2006)

Theorem 1 *The rate of distortion function for a Bernoulli(p) source with Hamming distortion is given by*

$$
R(D)=\begin{cases} H(p)-H(D) & if \quad 0\leq D\, min(p,1-p)\\ 0 & if \quad D\geq\ min(p,1-p)\end{cases} \qquad (6.6)
$$

$$(6.7)$$

where $H(\cdot)$ is the entropy. And the hamming distortion is defined as

$$
d(x,\hat{x})=\begin{cases} 0 & \text{if } x=\hat{x}\\ 1 & \text{if } x\neq\hat{x}\end{cases} \qquad (6.8)
$$

where x is a realisation of a random process X^N.

In order to use R-D analysis, the photoreceptor model was stimulated with a sequence $s(t)$, which is a given realisation of the previously introduced random process S^N, defined as

$$
s(t) := \text{train of pulses, with } s\in[0,A], A\in\mathbf{R} \qquad (6.9)
$$

In addition to predicted output by the NARX filter, given by equation 6.1, $y(t)$, in this case produced by the input stimuli $s(t)$, by using the concepts of GFRFs and OFRFs introduced in chapter 3 and described by Equations 3.43 and 3.49,

$y_1(t)$ and $y_2(t)$, which are the linear and nonlinear parts of the predicted response were also computed. So, for a given stimuli sequence $s(t)$ three different output sequences, $y^s(t)$, $y^s_1(t)$ and $y^s_2(t)$ are obtained. Assuming that the NARX model is stable for the described $s(t)$ stimuli, then

$$
y^s_{(\cdot)}(t)\in\mathbf{R}\forall t=1,2,\cdots,N \qquad (6.10)
$$

Table 6.1 Rate-Distortion of Total (y), Linear(y_1), and Nonlinear(y_2) Photoreceptor's NARX Predicted Output with SNR of 18dB.

Output type	Distortion - D	Estimated Rate - R	Theoretical Rate - R
Full response y	0.00872	10.33703	0.21421
Linear response y_1	0.00720	13.58781	0.22479
Nonlinear response y_2	0.00330	8.14842	0.25444

The NARX model was simulated $M = 10000$ times using the random process S^N, with $N = 2000$. Where each realisation of the random process is given by Equation 6.9 with Bernoulli distribution of $B(p = 0.05)$. Before presenting the simulation results, since the Bernoulli probability has been set, the theoretical lower bound for the R-D curve was computed. The result is shown in Fig. 6.5.

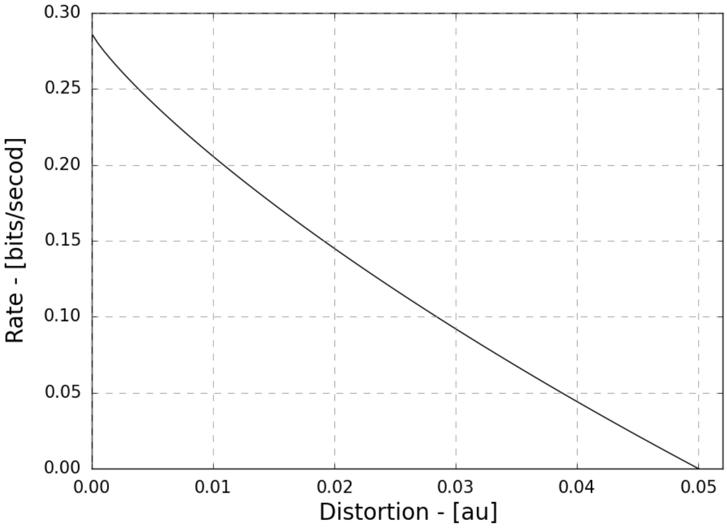

Fig. 6.5 Rate distortion function for a binary source with probability Bernoulli(p=0.05).

Estimates for the rate and distortion were computed using Equation 1 and Equation 6.8. The estimated results are presented in Table 6.1.

These results indicate that the nonlinear part of the photoreceptor predicted response by the NARX filter is more efficient, i.e. fewer bits/second are need to be transmitted in order to have a distortion that is not just similar but also fewer than either the linear part or the full response. In addition to being more efficient, when comparing the computed rates results to the theoretical lower bound, i.e. the rate values obtained using Theorem 1, y_2 the nonlinear response is closer (7.89398 bits/second) to the theoretical bound than the linear (13.36301 bits/second) and the full (10.12282 bits/second) responses.

In order to test the robustness to noise, more simulations were carried out. A new random process that describes the noise is introduced $W^N \sim N(0,\sigma_w^2)$. Where W^N is i.i.d(independent and identically distributed) and $w = [w_1,\cdots,w_r], r = 20$.

The $w_r = 20$ different values (0.05, 0.073, 0.097, 0.121, 0.144, 0.168, 0.192, 0.215, 0.239, 0.286, 0.31, 0.334, 0.357, 0.381, 0.405, 0.428, 0.452, 0.476, 0.5) were used to generate 20 different random processes which were added to the same set of stimuli used in the previous example. The newly created set of stimuli $[S^{N,w_0},\cdots,S^{N,w_r}]$, which resulted in input sequences with SNR ranging from 18dB($\sigma = 0.05$) to 7.6dB($\sigma = 0.5$), were used as input for the NARX photoreceptor model. Similarly to the previous simulation experiment, the full response $[Y^{N,w_0},\cdots,Y^{N,w_r}]$, the linear $[Y_1^{N,w_0},\cdots,Y_1^{N,w_r}]$ and nonlinear $[Y_2^{N,w_0},\cdots,Y_2^{N,w_r}]$ parts of the predicted response were obtained. The set of source and estimated sequences were transformed using the *binarisation algorithm* as in the previous example, to yield four different sets of random processes

$$\begin{aligned}
\text{input: } & [X^{N,w_0},\cdots,\hat{X}^{N,w_r}] \\
\text{predicted response: } & [\hat{X}_y^{N,w_0},\cdots,\hat{X}_y^{N,w_r}] \\
\text{linear part of the predicted response: } & [\hat{X}_{y_1}^{N,w_0},\cdots,\hat{X}_{y_1}^{N,w_r}] \\
\text{nonlinear part of the predicted response: } & [\hat{X}_{y_2}^{N,w_0},\cdots,\hat{X}_{y_2}^{N,w_r}]
\end{aligned}$$

The simulated and theoretical R-D pairs for the source (input) and each estimated(output) sequences were computed. The results are shown in Fig. 6.6. The results in this figure show that regardless of the noise level, the nonlinear part of the NARX filter is more efficient, i.e. closer to the theoretical bound - black line in the figure - that either the linear(blue) or full(red) NARX predicted responses. In fact, even for the greatest amount of noise used in this experiment, $W_N \sim N(0,\sigma_{w_{20}}^2)$, the nonlinear(green) part NARX photoreceptor still contains information. In the case of the linear part of the response, starting from $W_N \sim N(0,\sigma_{w_6}^2)$ the predicted response contains no information. Similarly, the full response stops being informative from $W_N \sim N(0,\sigma_{w_7}^2)$

Before computing the rate-distortion properties of the NARX filter for all simulations in the previous section the signals corresponding to the stimuli, total, linear and nonlinear components of the predicted response were processed using the Binarisation Algorithm to yield the source and estimated sequences X^N and $\hat{X}^N$ that were used to obtained the rate-distortion results.

In the third step of the algorithm, it is necessary to choose a threshold, the selection of this parameter is heuristic. In order to investigate the sensitivity of the rate-distortion estimates to

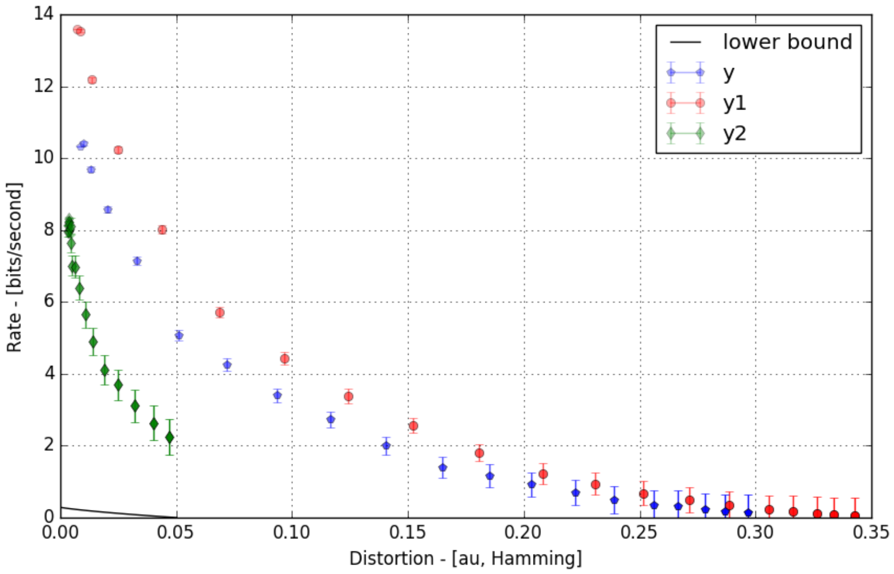

Fig. 6.6 Rate-Distortion, for threshold value of $th = 0.22$, for the total $y = y_1 + y_2$, linear y_1 and nonlinear y_2 photoreceptor responses. Different noise standard deviations are indicated by the error bars.

changes in the threshold, the algorithm was run with 50 different values of this parameter. The values were uniformly spaced between 0 and 0.5. Fig. 6.7 shows the comparison between the surfaces obtained by changing the selected threshold. The surface corresponding to the total response obtain is shown in blue, Fig.6.7 (a). The surfaces corresponding to the linear and nonlinear response are shown in red, Fig. 6.7 (b), and green, Fig. 6.7 (c), respectively.

The rate-distortion-threshold surfaces show that when increasing the threshold, the necessary rate to achieve a particular distortion decreases when using either encoding scheme. They also show that regardless of the noise level or selected threshold, the nonlinear encoding, y_2, outperforms the combined, $y = y_1 + y_2$ linear and nonlinear encodings which in turn outperforms the linear encoding, y_1.

In order to make these observations clearer, two-dimensional slices of the of each surface were computed.

The first slice is shown in Fig. 6.7 (d). This figure shows the behaviour of the surface when the distortion is kept zero (D=0), this situation is achieved when the level of noise in the signal is very small. In the figure it can be seen regardless of the threshold level none of the responses total, linear or nonlinear reach the theoretical limit, the grey area. This observation was expected and indicates the of the algorithm is obeys the theory. It also shows that for signals with very low levels of noise selecting a low value for the threshold favours, less

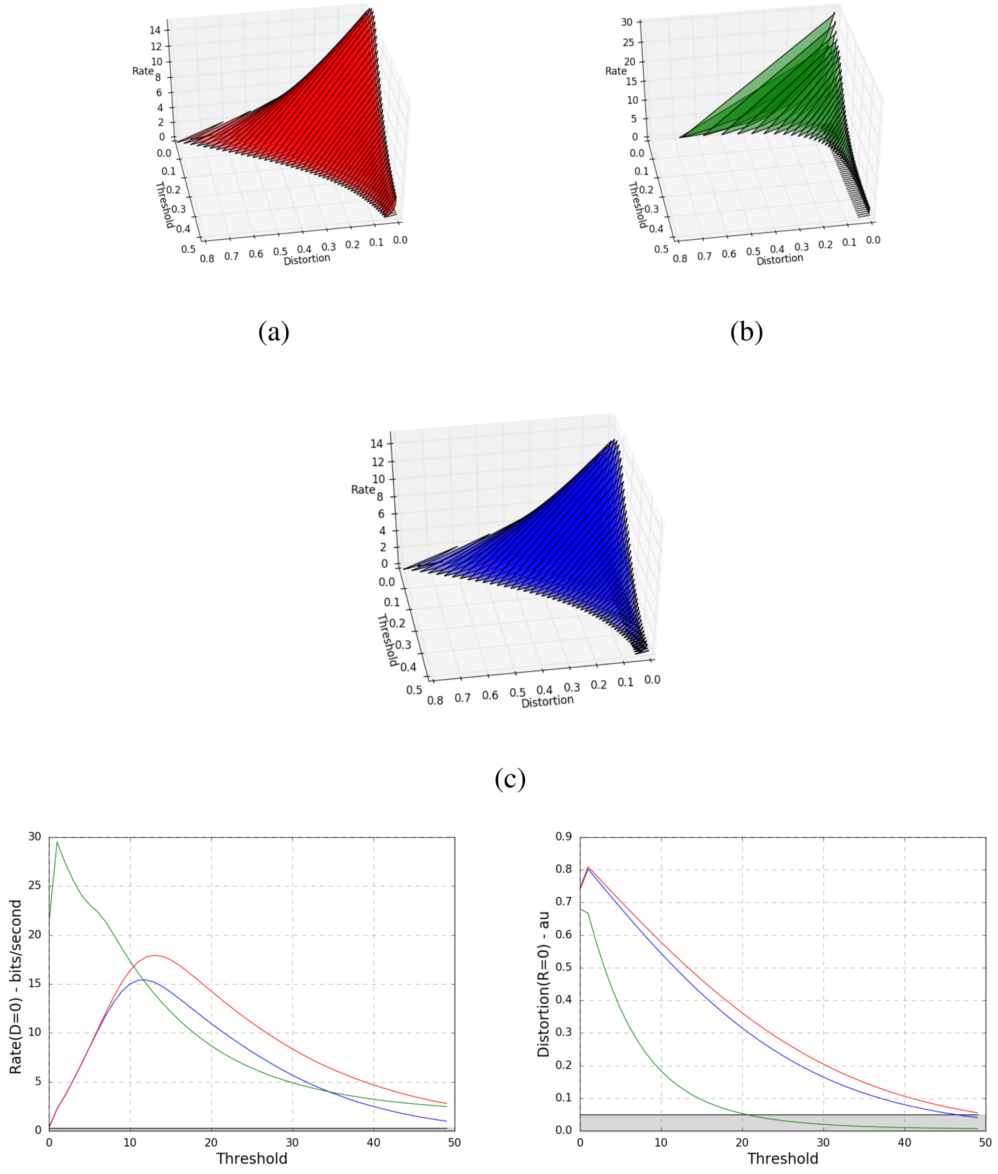

(a)

(b)

(c)

(d)

(e)

Fig. 6.7 Threshold-Rate-Distortion(TRD) Analysis. Individual TRD surfaces for (a) linear, (b) nonlinear and (c) total photoreceptor response when varying the threshold in the range of (0, 0.5) are shown in panels (b), (c) and (a) respectively. In all figures the theoretical lower bound is shown in black. Also, slices of these surfaces for the cases of low noise levels and high noise levels are shown in panels (d) and (e) respectively.

bits per second are required for reconstruction, the linear(red line) or total(blue line) over the nonlinear response. However selecting greater values for the threshold parameter, the difference is less significant. Moreover, for certain values of the threshold, between 13 and 34, using the nonlinear response(green line), to reconstruct the signal is more efficient than using either the linear or the total responses.

The second slice is shown in Fig. 6.7 (e). This figure corresponds to signals with high noise levels. In Fig. 6.7, the grey area indicates where information contained in the signal can be recovered using this algorithm. Taking this into account it is clear that when selecting threshold values less than 20, none of the responses convey any useful information for signal recovery. Moreover, it is mainly the nonlinear response the one that carries useful information for signal recovery purposes when the threshold is selected to be greater than 20.

For either encoding scheme, there is a considerable distance between the estimated R-D curve and the theoretical lower bound. Two main items can be highlighted from these results.The first one is that nonlinear transductions at photoreceptor level play an important role in encoding behavioural relevant features in an efficient and robust way. And the second is related to the distance to the theoretical lower bound, which indicates there is a more efficient way of encoding pulses embedded in noise than using the nonlinear coding derived from the photoreceptor's model.

6.4 Conclusion

In this Chapter the linear and nonlinear encoding capabilities of R1-R6 photoreceptors were investigated by performing separate rate-distortion (R-D) analysis on the linear and nonlinear components on the photoreceptor response for a binary Bernoulli(p) source.

It was shown that the photoreceptor models for wild-type and hdc$^{\mathrm{JK910}}$ process stimuli in a very similar fashion and both have the phase congruency detection features reported in (Friederich et al., 2016).

Making use of the photoreceptor's sensitivity to phase congruent features in stimuli, an artificial stimulus consisting of a sequence of pulses embedded in multiple white Gaussian noise signals with different standard deviations were created and used as inputs to the NARX filter of the photoreceptor model in order to explore its encoding capabilities.

The results showed that regardless of which photoreceptor response component was used, either full, linear or nonlinear, there exist more efficient strategies to encode stimuli with high phase congruency properties than using the NARX filter of the photoreceptor's model in combination with the introduced *Binarisation Algorithm*. It was also shown that using the nonlinear component of the predicted response of the photoreceptor's model is both, more robust to noise and more efficient at encoding the artificial stimulus used for the conducted study in this Chapter, than either the linear or total predicted response.

Chapter 7

Conclusions

This thesis introduced two new empirical models of the early visual system were introduced. The first model is capable of predicting the response of individual photoreceptors of wild-type and histamine-deficient hdc$^{\mathrm{JK910}}$ fruit flies. This model forms the basis for a combined model of six photoreceptors that receive input from the same source and connect via feedforward and feedback loops, with the same group of Large Monopolar and Amacrine cells in the lamina. This Model, referred as PR1-6/LMC, can predict photoreceptor responses of wild and blind flies. It also contains an explicit model of the lamina contribution in shaping the photoreceptors response. These models are used to characterise for the first time the information processing capabilities of photoreceptors using rate-distortion theory.

7.1 Contributions Summary

For the first time, thanks to the availability of electrophysiological recordings obtained from *in-vivo* experiments carried out in wild and hdc$^{\mathrm{JK910}}$ PR1-PR6 photoreceptors and by applying state-of-the-art nonlinear system identification technique, it was possible to estimate a model of the interaction between neurons in the retina and lamina. This model provides the most faithful representation of the dynamical information processing implemented by monochromatic photoreceptors in *Drosophila's* visual system.

By carrying out a detailed analysis of the input-output data collected from the intracellular recordings from photoreceptors of wild- and mutant- type when using naturalistic stimulus it was possible to identify the key differences in stimulus adaptation between the two different types of flies. The identification of these differences led to the implementation of separate mechanisms for mean and contrast gain control. Specifically, the analysis revealed that photoreceptors implement distinct mean and contrast adaptation mechanisms and that these mechanisms are altered in a different fashion in the absence of histamine mediated feedforward and feedback signalling from the lamina. In particular for bright intensities, mean adaptation is faster in wild-type than mutant photoreceptors. Furthermore, the lamina seems to play a key role in the contrast adaptation i.e. in the absence of feedback from lamina the contrast adaptation is severely impaired for bright stimuli.

The new photoreceptor model captures all these characteristics by incorporating separate models of mean and contrast gain control. In order to be able to characterise both the wild-type and mutant responses using a single model architecture, the contribution from the lamina was modelled as a separate interconnected block, such that when simulating mutant response, the lamina model could be simply switched off. This modelling approach, allowed for the first time to characterise quantitatively the role of the lamina in shaping the photoreceptor adaptation at different level of light intensities.

The model of the interneurones that connect with a group of six photoreceptors was derived using system identification.

The new photoreceptor model predicts well the responses wild and hdc$^{\mathrm{JK910}}$ flies to naturalistic stimulation. At the same time, the new model architecture enables building a model of the local retina network involving six photoreceptors and their interneurones partners in the lamina, which can be used as a building block for a complete model of the fly retina.

The lamina dynamical model was obtained using system identification At the same time, the new model architecture enables building a model of the local retina network involving six photoreceptors and their interneurones partners in the lamina, which can be used as a building block for a complete model of the fly retina.

This is arguably the first model that represents explicitly the contribution from lamina interneurones to the photoreceptor adaptation in fruit flies. In terms of prediction capabilities, the model yields results with NMSE of about 1% for wild-type and mutant fly photoreceptors. The results indicate that further improvements are possible if additional experimental recordings from photoreceptors and interneurones of the same fly are available.

The mathematical models developed as part of the research project were used to characterise for the first time and in a rigorous manner, using information theoretic tools, the performance and information capacity limits of fly photoreceptors. Specifically, the analysis, provides further quantitative characterisation of the recently discovered (Friederich et al., 2016) phase congruency encoding properties of fly photoreceptors. The analysis involves performing a time and frequency domain decomposition of the photoreceptor response to a synthetic stimulus sequence, into linear and nonlinear response components that correspond to different kernels of the associated Volterra series expansion. Specifically, the synthetic stimuli was designed as a superposition of random squared pulses, that follow a Bernoulli distribution and Gaussian noise with different variances. Using rate-distortion analysis, an encoding algorithm proposed in this thesis and the decomposed photoreceptor responses, the transductions that take place at photoreceptor level were characterised from an information theoretic point of view.

The results of this study demonstrate that encoding pulses using the nonlinear part of the photoreceptor model is more efficient and robust than using either the overall response or just the linear part. The results also show that for all the different cases with increasing levels of noise, using nonlinear encoding was more efficient than using linear coding. In particular, the required rate to achieve low distortion is much lower when using nonlinear encoding.

7.2 Future Work

The research presented in this thesis can form the basis for future studies that aim to elucidate further visual processing in fruit flies.

The new photoreceptor model suggests that we should look for plausible, separate biophysical mechanisms for mean and contrast adaptation. These mechanisms could be explicitly modelled and used to refine the current biophysical models of photoreceptors. The model of the elementary retinal network circuit could be used to develop a complete, anatomically realistic model of the *Drosophila* early visual system, i.e. the entire retina and lamina interconnected. Such model could form the basis of developing neurodegenerative disease models for Parkinson disease for example (Whitworth, 2011).

The rate distortion analysis introduced in chapter 6 will be used in the near future to investigate the differences shown by fly photoreceptors in coding information for different types of stimuli and in different environments.

References

Aguirre, L. A. and Aguirre, A. (2002). Analysis of economic time series using narmax polynomial models. In *Modelling and Forecasting Financial Data*, pages 213–235. Springer.

Aguirre, L. A. and Billings, S. A. (1995). Dynamical effects of overparametrization in nonlinear models. *Physica D: Nonlinear Phenomena*, 80(1):26–40.

Ahrens, M. B., Paninski, L., and Sahani, M. (2008). Inferring input nonlinearities in neural encoding models. *Network: Computation in Neural Systems*, 19(1):35–67.

Ai, M., Min, S., Grosjean, Y., Leblanc, C., Bell, R., Benton, R., and Suh, G. S. (2010). Acid sensing by the drosophila olfactory system. *Nature*, 468(7324):691–695.

Akaike, H. (1974). A new look at the statistical model identification. *IEEE transactions on automatic control*, 19(6):716–723.

Arlot, S., Celisse, A., et al. (2010). A survey of cross-validation procedures for model selection. *Statistics surveys*, 4:40–79.

Badoual, M., Zou, Q., Davison, A. P., Rudolph, M., Bal, T., Frégnac, Y., and Destexhe, A. (2006). Biophysical and phenomenological models of multiple spike interactions in spike-timing dependent plasticity. *International journal of neural systems*, 16(02):79–97.

Barlow, H. (2001). Redundancy reduction revisited. *Network: computation in neural systems*, 12(3):241–253.

Barlow, H. B. (1961). Possible principles underlying the transformations of sensory messages.

Bassett, D. S. and Gazzaniga, M. S. (2011). Understanding complexity in the human brain. *Trends in cognitive sciences*, 15(5):200–209.

Battle, G. (1987). A block spin construction of ondelettes. part i: Lemarié functions. *Communications in Mathematical Physics*, 110(4):601–615.

Beckingham, K. M., Armstrong, J. D., Texada, M. J., Munjaal, R., and Baker, D. A. (2007). Drosophila melanogaster-the model organism of choice for the complex biology of multi-cellular organisms. *Gravitational and Space Research*, 18(2).

Bellen, H. J., Tong, C., and Tsuda, H. (2010). 100 years of drosophila research and its impact on vertebrate neuroscience: a history lesson for the future. *Nature Reviews Neuroscience*, 11(7):514–522.

Berg, A., McMurry, T., and Politis, D. N. (2012). Testing time series linearity: traditional and bootstrap methods. *Handbook of Statistics: Time Series Analysis: Methods and Applications*, 30:27.

Billings, S. (1980). Identification of nonlinear systems¿ a survey. In *IEE Proceedings D-Control Theory and Applications*, volume 127, pages 272–285. IET.

Billings, S., Chen, S., and Korenberg, M. (1989). Identification of mimo non-linear systems using a forward-regression orthogonal estimator. *International Journal of Control*, 49(6):2157–2189.

Billings, S. and Coca, D. (1999). Discrete wavelet models for identification and qualitative analysis of chaotic systems. *International Journal of Bifurcation and Chaos*, 9(07):1263–1284.

Billings, S., Coca, D., of Automatic Control, S. U. K. D., and Engineering;, S. (2001). Identification of narmax and related models.

Billings, S. and Peyton Jones, J. (1990). Mapping non-linear integro-differential equations into the frequency domain. *International Journal of Control*, 52(4):863–879.

Billings, S. and Tsang, K. (1989). Spectral analysis for non-linear systems, part ii: Interpretation of non-linear frequency response functions. *Mechanical Systems and Signal Processing*, 3(4):341–359.

Billings, S., Tsang, K., and Tomlinson, G. (1990). Spectral analysis for non-linear systems, part iii: Case study examples. *Mechanical Systems and Signal Processing*, 4(1):3–21.

Billings, S. and Voon, W. (1986). Correlation based model validity tests for non-linear models. *International journal of Control*, 44(1):235–244.

Billings, S. and Zhu, Q. (1994). Nonlinear model validation using correlation tests. *International Journal of Control*, 60(6):1107–1120.

Billings, S. and Zhu, Q. (1995). Model validation tests for multivariable nonlinear models including neural networks. *International Journal of Control*, 62(4):749–766.

Billings, S. A. (2013). *Nonlinear system identification: NARMAX methods in the time, frequency, and spatio-temporal domains*. John Wiley & Sons.

Billings, S. A. and Chen, S. (1989). Identification of non-linear rational systems using a prediction-error estimation algorithm. *International Journal of Systems Science*, 20(3):467–494.

Billings, S. A., Korenberg, M. J., and Chen, S. (1988). Identification of non-linear output-affine systems using an orthogonal least-squares algorithm. *International Journal of Systems Science*, 19:1559–1568.

Billings, S. A. and Leontaritis, I. J. (1981). Identification of nonlinear Systems using Parameter Estimation Techniques. In *IEE Conference Publication, Warwick University Computing Systems*, pages 183–187.

Billings, S. A. and Wei, H.-L. (2005). The wavelet-narmax representation: A hybrid model structure combining polynomial models with multiresolution wavelet decompositions. *International Journal of Systems Science*, 36(3):137–152.

Boaghe, O., Balikhin, M., Billings, S., and Alleyene, H. (1999). Identification of nonlinear processes in the magnetospheric dynamics and forecasting of dst index.

Boaghe, O., Billings, S., Li, L., Fleming, P., and Liu, J. (2002). Time and frequency domain identification and analysis of a gas turbine engine. *Control Engineering Practice*, 10(12):1347–1356.

Borst, A. (2009). Drosophila's view on insect vision. *Current biology*, 19(1):R36–R47.

Borst, A. (2014). Fly visual course control: behaviour, algorithms and circuits. *Nature Reviews Neuroscience*, 15(9):590–599.

Brinkworth, R. S., Mah, E.-L., Gray, J. P., and O'Carroll, D. C. (2008). Photoreceptor processing improves salience facilitating small target detection in cluttered scenes. *Journal of vision*, 8(11):8–8.

Browne, M. W. (2000). Cross-validation methods. *Journal of mathematical psychology*, 44(1):108–132.

Carandini, M., Demb, J. B., Mante, V., Tolhurst, D. J., Dan, Y., Olshausen, B. A., Gallant, J. L., and Rust, N. C. (2005). Do we know what the early visual system does? *The Journal of neuroscience*, 25(46):10577–10597.

Chen, S. (2006). Local regularization assisted orthogonal least squares regression. *Neurocomputing*, 69(4):559–585.

Chen, S. and Billings, S. (1989a). Representations of non-linear systems: the narmax model. *International Journal of Control*, 49(3):1013–1032.

Chen, S., Billings, S., Cowan, C., and Grant, P. (1990). Practical identification of narmax models using radial basis functions. *International Journal of Control*, 52(6):1327–1350.

Chen, S. and Billings, S. A. (1989b). Representations of non-linear systems: the NARMAX model. *International Journal of Control*, 49(3):1013–1032.

Chen, S., Billings, S. A., and Luo, W. (1989). Orthogonal least squares methods and their application to non-linear system identification. *International Journal of Control*, 50:1873–1896.

Chen, S., Cowan, C. F., and Grant, P. M. (1991). Orthogonal least squares learning algorithm for radial basis function networks. *IEEE Transactions on neural networks*, 2(2):302–309.

Chen, S., Hong, X., Luk, B. L., and Harris, C. J. (2009). Orthogonal-least-squares regression: A unified approach for data modelling. *Neurocomputing*, 72(10):2670–2681.

Chua, L. O. and Ng, C.-Y. (1979). Frequency domain analysis of nonlinear systems: general theory. *Electronic Circuits and Systems, IEE Journal on*, 3(4):165–185.

Coca, D. and Billings, S. (2001). Non-linear system identification using wavelet multiresolution models. *International Journal of Control*, 74(18):1718–1736.

Coca, D. and Billings, S. A. (2002). Identification of finite dimensional models of infinite dimensional dynamical systems. *Automatica*, 38(11):1851–1865.

Cover, T. M. and Thomas, J. A. (2006). Elements of information theory 2nd edition.

Dau, A., Friederich, U., Dongre, S., Li, X., Bollepalli, M. K., Hardie, R. C., and Juusola, M. (2016). Evidence for dynamic network regulation of drosophila photoreceptor function from mutants lacking the neurotransmitter histamine. *Frontiers in neural circuits*, 10.

Diaz, H. and Desrochers, A. A. (1988). Modeling of nonlinear discrete-time systems from input-output data. *Automatica*, 24(5):629–641.

Dubs, A. (1981). Non-linearity and light adaptation in the fly photoreceptor. *Journal of Comparative Physiology A: Neuroethology, Sensory, Neural, and Behavioral Physiology*, 144(1):53–59.

Frechter, S. and Minke, B. (2006). Light-regulated translocation of signaling proteins in drosophila photoreceptors. *Journal of Physiology-Paris*, 99(2):133–139.

French, A. (1976). Practical nonlinear system analysis by wiener kernel estimation in the frequency domain. *Biological Cybernetics*, 24(2):111–119.

French, A. (1979). The effect of light adaptation on the dynamic properties of phototransduction in the fly, phormia regina. *Biological Cybernetics*, 32(2):115–123.

French, A. and Butz, E. (1973). Measuring the wiener kernels of a non-linear system using the fast fourier transform algorithm†. *International Journal of Control*, 17(3):529–539.

French, A., Korenberg, M., Järvilehto, M., Kouvalainen, E., Juusola, M., and Weckström, M. (1993). The dynamic nonlinear behavior of fly photoreceptors evoked by a wide range of light intensities. *Biophysical journal*, 65(2):832.

French, A. S. and Marmarelis, V. Z. (1999). Nonlinear analysis of neuronal systems. In *Modern Techniques in Neuroscience Research*, pages 627–640. Springer.

Friederich, U. (2011). *Nonlinear System Identification and Analysis of Adaptive Neural Information Processing in the Fly Early Visual System*. PhD thesis, The University of Sheffield.

Friederich, U., Billings, S. A., Hardie, R. C., Juusola, M., and Coca, D. (2016). Fly photoreceptors encode phase congruency. *PLoS One*, 11(6):e0157993.

Friederich, U., Billings, S. A., Juusola, M., and Coca, D. (2013). We now know what fly photoreceptors compute. *BMC Neuroscience*, 14(1):1–2.

Friederich, U., Billings, S. A., Juusola, M. A., and Coca, D. (2012). Reverse Engineering Gain Adaptation in Sensory Systems. ACTAPRESS.

Friederich, U., Coca, D., Billings, S., and Juusola, M. (2009). Data Modelling for Analysis of Adaptive Changes in Fly Photoreceptors. In Leung, C. S., Lee, M., and Chan, J. H., editors, *Neural Information Processing*, number 5863 in Lecture Notes in Computer Science, pages 34–48. Springer Berlin Heidelberg.

Functions, S. (1981). Basic theory. *Larry L Schumaker, Cambridge Mathematical Library.*

Giri, F. and Bai, E.-W. (2010). *Block-oriented nonlinear system identification*, volume 1. Springer.

Gollisch, T. and Meister, M. (2008). Modeling convergent on and off pathways in the early visual system. *Biological cybernetics*, 99(4-5):263–278.

González, J., Rojas, I., Ortega, J., Pomares, H., Fernandez, F. J., and Díaz, A. F. (2003). Multiobjective evolutionary optimization of the size, shape, and position parameters of radial basis function networks for function approximation. *IEEE Transactions on Neural Networks*, 14(6):1478–1495.

Guerra, F. A. and Coelho, L. d. S. (2008). Multi-step ahead nonlinear identification of lorenz's chaotic system using radial basis neural network with learning by clustering and particle swarm optimization. *Chaos, Solitons & Fractals*, 35(5):967–979.

Hadjieconomou, D., Timofeev, K., and Salecker, I. (2011). A step-by-step guide to visual circuit assembly in drosophila. *Current opinion in neurobiology*, 21(1):76–84.

Hardie, R. (1987). Is histamine a neurotransmitter in insect photoreceptors? *Journal of Comparative Physiology A*, 161(2):201–213.

Hardie, R. (1991). Whole-cell recordings of the light induced current in dissociated drosophila photoreceptors: evidence for feedback by calcium permeating the light-sensitive channels. *Proceedings of the Royal Society of London B: Biological Sciences*, 245(1314):203–210.

Hardie, R., Peretz, A., Suss-Toby, E., Rom-Glas, A., Bishop, S., Selinger, Z., and Minke, B. (1993). Protein kinase c is required for light adaptation in drosophila photoreceptors. *Nature*, 363(6430):634–637.

Hardie, R. and Postma, M. (2008a). 1.05–phototransduction in microvillar photoreceptors of drosophila and other invertebrates. In *The senses: a comprehensive reference*, pages 77–130. Elsevier Science/Academic Press.

Hardie, R. C. (1985). Functional organization of the fly retina. In *Progress in sensory physiology*, pages 1–79. Springer.

Hardie, R. C. (1989). A histamine-activated chloride channel involved in neurotransmission at a photoreceptor synapse. *Nature*, 339(6227):704–706.

Hardie, R. C. (2001). Phototransduction in drosophila melanogaster. *Journal of Experimental Biology*, 204(20):3403–3409.

Hardie, R. C. (2012a). Phototransduction mechanisms in drosophila microvillar photoreceptors. *Wiley Interdisciplinary Reviews: Membrane Transport and Signaling*, 1(2):162–187.

Hardie, R. C. (2012b). Polarization vision: Drosophila enters the arena. *Current Biology*, 22(1):R12–R14.

Hardie, R. C. and Minke, B. (1994). Calcium-dependent inactivation of light-sensitive channels in drosophila photoreceptors. *The Journal of general physiology*, 103(3):409–427.

Hardie, R. C. and Postma, M. (2008b). Phototransduction in Microvillar Photoreceptors of Drosophila and Other Invertebrates. In *The Senses: A Comprehensive Reference,Vol 1, Vision I.* Academic Press, T. D. Albright and R. Masland.,San Diego.

Hardie, R. C. and Postma, M. (2008c). Phototransduction in Microvillar Photoreceptors of Drosophila and Other Invertebrates. In *The Senses: A Comprehensive Reference,Vol 1, Vision I.* Academic Press, T. D. Albright and R. Masland.,San Diego.

Hardie, R. C. and Raghu, P. (2001a). Visual transduction in Drosophila. *Nature*, 413(6852):186–193.

Hardie, R. C. and Raghu, P. (2001b). Visual transduction in drosophila. *Nature*, 413(6852):186–193.

Hateren, J. H. v. (1992). A theory of maximizing sensory information. *Biological Cybernetics*, 68(1):23–29.

Hateren, J. H. v. and Snippe, H. P. (2006). Phototransduction in primate cones and blowfly photoreceptors: different mechanisms, different algorithms, similar response. *Journal of Comparative Physiology A*, 192(2):187–197.

Haykin, S. and Network, N. (2004). A comprehensive foundation. *Neural Networks*, 2(2004).

Heintz, N. (2001). Bac to the future: the use of bac transgenic mice for neuroscience research. *Nature Reviews Neuroscience*, 2(12):861–870.

Heisenberg, M. and Buchner, E. (1977). The role of retinula cell types in visual behavior of drosophila melanogaster. *Journal of comparative physiology*, 117(2):127–162.

Heisenberg, M. and Wolf, R. (2013). *Vision in Drosophila: genetics of microbehavior*, volume 12. Springer-Verlag.

Homberg, U., Heinze, S., Pfeiffer, K., Kinoshita, M., and El Jundi, B. (2011). Central neural coding of sky polarization in insects. *Philosophical Transactions of the Royal Society of London B: Biological Sciences*, 366(1565):680–687.

Hong, X., Mitchell, R., Chen, S., Harris, C., Li, K., and Irwin, G. (2008). Model selection approaches for non-linear system identification: a review. *International Journal of Systems Science*, 39(10):925–946.

Horridge, G., Mimura, K., and Hardie, R. (1976). Fly photoreceptors. iii. angular sensitivity as a function of wavelength and the limits of resolution. *Proceedings of the Royal Society of London B: Biological Sciences*, 194(1115):151–177.

Hu, W., Wang, T., Wang, X., and Han, J. (2015). I h channels control feedback regulation from amacrine cells to photoreceptors. *PLoS Biol*, 13(4):e1002115.

Hunter, I. and Korenberg, M. (1986). The identification of nonlinear biological systems: Wiener and hammerstein cascade models. *Biological cybernetics*, 55(2-3):135–144.

James, G., Witten, D., Hastie, T., and Tibshirani, R. (2013). *An introduction to statistical learning*, volume 6. Springer.

Jones, J. P. (2007). Simplified computation of the volterra frequency response functions of non-linear systems. *Mechanical systems and signal processing*, 21(3):1452–1468.

Jones, J. P. and Billings, S. (1989). Recursive algorithm for computing the frequency response of a class of non-linear difference equation models. *International Journal of Control*, 50(5):1925–1940.

Jones, J. P. and Choudhary, K. (2012). Efficient computation of higher order frequency response functions for nonlinear systems with, and without, a constant term. *International Journal of Control*, 85(5):578–593.

Juusola, M. (1994). Measuring complex admittance and receptor current by single electrode voltage-clamp. *Journal of neuroscience methods*, 53(1):1–6.

Juusola, M. and de Polavieja, G. G. (2003). The rate of information transfer of naturalistic stimulation by graded potentials. *The Journal of general physiology*, 122(2):191–206.

Juusola, M. and Hardie, R. C. (2001). Light adaptation in drosophila photoreceptors i. response dynamics and signaling efficiency at 25 c. *The Journal of general physiology*, 117(1):3–25.

Juusola, M., Kouvalainen, E., Järvilehto, M., and Weckström, M. (1994). Contrast gain, signal-to-noise ratio, and linearity in light-adapted blowfly photoreceptors. *The Journal of general physiology*, 104(3):593–621.

Juusola, M., Uusitalo, R., and Weckström, M. (1995a). Transfer of graded potentials at the photoreceptor-interneuron synapse. *The Journal of general physiology*, 105(1):117–148.

Juusola, M., Weckstrom, M., Uusitalo, R., Korenberg, M., and French, A. (1995b). Nonlinear models of the first synapse in the light-adapted fly retina. *Journal of Neurophysiology*, 74(6):2538–2547.

Kalueff, A. V., Stewart, A. M., and Gerlai, R. (2014). Zebrafish as an emerging model for studying complex brain disorders. *Trends in pharmacological sciences*, 35(2):63–75.

Kibangou, A. Y. and Favier, G. (2010). Tensor analysis-based model structure determination and parameter estimation for block-oriented nonlinear systems. *IEEE Journal of Selected Topics in Signal Processing*, 4(3):514–525.

Kim, A. J., Lazar, A. A., and Slutskiy, Y. B. (2011). System identification of drosophila olfactory sensory neurons. *Journal of computational neuroscience*, 30(1):143–161.

Kim, A. J., Lazar, A. A., and Slutskiy, Y. B. (2015). Projection neurons in drosophila antennal lobes signal the acceleration of odor concentrations. *Elife*, 4:e06651.

Kirschfeld, K. (1967). Die projektion der optischen umwelt auf das raster der rhabdomere im komplexauge von musca. *Experimental Brain Research*, 3(3):248–270.

Kirschfeld, K. and Franceschini, N. (1969). Ein mechanismus zur steuerung des lichtflusses in den rhabdomeren des komplexauges von musca. *Kybernetik*, 6(1):13–22.

Kolodziejczyk, A., Sun, X., Meinertzhagen, I. A., and Nässel, D. R. (2008). Glutamate, gaba and acetylcholine signaling components in the lamina of the drosophila visual system. *PloS one*, 3(5):e2110.

Korenberg, M., Billings, S. A., Liu, Y. P., and McIlroy, P. J. (1988a). Orthogonal parameter estimation algorithm for non-linear stochastic systems. *International Journal of Control*, 48(1):193–210.

Korenberg, M., Bruder, S., and Mcllroy, P. (1988b). Exact orthogonal kernel estimation from finite data records: Extending weiner's identification of nonlinear systems. *Annals of biomedical engineering*, 16(2):201–214.

Korenberg, M. J. (1991). Parallel cascade identification and kernel estimation for nonlinear systems. *Annals of biomedical engineering*, 19(4):429–455.

Korenberg, M. J. and Hunter, I. (1986). The identification of nonlinear biological systems: Lnl cascade models. *Biological cybernetics*, 55(2-3):125–134.

Korenberg, M. J. and Hunter, I. W. (1996). The identification of nonlinear biological systems: Volterra kernel approaches. *Annals of biomedical engineering*, 24(2):250–268.

Korenberg, M. J. and Paarmann, L. D. (1989). Applications of fast orthogonal search: Time-series analysis and resolution of signals in noise. *Annals of biomedical engineering*, 17(3):219–231.

Krishnanathan, K., Anderson, S. R., Billings, S. A., and Kadirkamanathan, V. (2012). A data-driven framework for identifying nonlinear dynamic models of genetic parts. *ACS synthetic biology*, 1(8):375–384.

Labhart, T. and Meyer, E. P. (1999). Detectors for polarized skylight in insects: a survey of ommatidial specializations in the dorsal rim area of the compound eye. *Microscopy research and technique*, 47(6):368–379.

Lang *, Z. Q. and Billings, S. A. (2005). Energy transfer properties of non-linear systems in the frequency domain. *International Journal of Control*, 78(5):345–362.

Lang, Z., Billings, S., Yue, R., and Li, J. (2007). Output frequency response function of nonlinear Volterra systems. *Automatica*, 43(5):805–816.

Larsen, J. and Goutte, C. (1999). On optimal data split for generalization estimation and model selection. In *Neural Networks for Signal Processing IX, 1999. Proceedings of the 1999 IEEE Signal Processing Society Workshop.*, pages 225–234. IEEE.

Laughlin, S. B. (1989a). The role of sensory adaptation in the retina. *Journal of Experimental Biology*, 146(1):39–62.

Laughlin, S. B. (1989b). The role of sensory adaptation in the retina. *The Journal of experimental biology*, 146:39–62.

Laughlin, S. B. and Hardie, R. C. (1978). Common strategies for light adaptation in the peripheral visual systems of fly and dragonfly. *Journal of comparative physiology*, 128(4):319–340.

Lee, Y. and Schetzen, M. (1965). Measurement of the wiener kernels of a non-linear system by cross-correlation†. *International Journal of Control*, 2(3):237–254.

Leeb, H. and Pötscher, B. M. (2009). Model selection. In *Handbook of Financial Time Series*, pages 889–925. Springer.

Lemarié, P.-G. (1988). Ondelettesa localisation exponentielle. *J. Math. Pures Appl*, 67(3):227–236.

Lennart, L. (1999). System identification: theory for the user. *PTR Prentice Hall, Upper Saddle River, NJ*, pages 1–14.

Leu, J.-F., Jang, J.-C., and Hwang, C. (1998). Computation of battle–lemarie wavelets using an fft-based algorithm. *Journal of scientific computing*, 13(4):485–504.

Levenberg, K. (1944). A method for the solution of certain non-linear problems in least squares. *Quarterly of applied mathematics*, 2(2):164–168.

Li, L. and Billings*, S. (2005). Discrete time subharmonic modelling and analysis. *International Journal of Control*, 78(16):1265–1284.

Ljung, L. (2009). *System identification: theory for the user*. Prentice-Hall, Upper Saddle River, NJ.

Ljung, L. (2010). Perspectives on system identification. *Annual Reviews in Control*, 34(1):1–12.

Luo, W. and Billings, S. (1995). Adaptive model selection and estimation for nonlinear systems using a sliding data window. *Signal Processing*, 46(2):179–202.

Marmarelis, V. Z. (1993). Identification of nonlinear biological systems using laguerre expansions of kernels. *Annals of biomedical engineering*, 21(6):573–589.

Marmarelis, V. Z. (1997). Modeling methology for nonlinear physiological systems. *Annals of biomedical engineering*, 25(2):239–251.

Marmarelis, V. Z. (2004). *Nonlinear dynamic modeling of physiological systems*, volume 10. John Wiley & Sons.

Marquardt, D. W. (1963). An algorithm for least-squares estimation of nonlinear parameters. *Journal of the society for Industrial and Applied Mathematics*, 11(2):431–441.

Meinertzhagen, I. and Sorra, K. (2001). Synaptic organization in the fly's optic lamina: few cells, many synapses and divergent microcircuits. *Progress in brain research*, 131:53.

Minke, B. and Cook, B. (2002). Trp channel proteins and signal transduction. *Physiological reviews*, 82(2):429–472.

Minke, B. and Hardie, R. (2000). Genetic dissection of drosophila phototransduction. *Handbook of biological physics*, 3:449–525.

Mizunami, M. (1995). Information processing in the insect ocellar system: comparative approaches to the evolution of visual processing and neural circuits. *Advances in Insect Physiology*, 25:151–265.

Montell, C. (2012). Drosophila visual transduction. *Trends in neurosciences*, 35(6):356–363.

Morante, J. and Desplan, C. (2008). The color-vision circuit in the medulla of drosophila. *Current Biology*, 18(8):553–565.

Nelles, O. (2013). *Nonlinear system identification: from classical approaches to neural networks and fuzzy models*. Springer Science & Business Media.

Nikolaev, A., Zheng, L., Wardill, T. J., O'Kane, C. J., de Polavieja, G. G., and Juusola, M. (2009). Network adaptation improves temporal representation of naturalistic stimuli in drosophila eye: Ii mechanisms. *PLoS One*, 4(1):e4306.

Nikolic, K., Loizu, J., Degenaar, P., and Toumazou, C. (2010). A stochastic model of the single photon response in Drosophila photoreceptors. *Integrative biology: quantitative biosciences from nano to macro*, 2(7-8):354–370.

Niven, J. E., Vähäsöyrinki, M., Kauranen, M., Hardie, R. C., Juusola, M., and Weckström, M. (2003a). The contribution of shaker k+ channels to the information capacity of drosophila photoreceptors. *Nature*, 421(6923):630–634.

Niven, J. E., Vähäsöyrinki, M., Kauranen, M., Hardie, R. C., Juusola, M., and Weckström, M. (2003b). The contribution of Shaker K+ channels to the information capacity of Drosophila photoreceptors. *Nature*, 421(6923):630–634.

Niven, J. E., Vähäsöyrinki, M., Kauranen, M., Hardie, R. C., Juusola, M., and Weckström, M. (2003c). The contribution of Shaker K+ channels to the information capacity of Drosophila photoreceptors. *Nature*, 421(6923):630–634.

Ogata, K. (1995). *Discrete-time control systems*, volume 8. Prentice-Hall Englewood Cliffs, NJ.

Ogura, H. (1985). Estimation of wiener kernels of a nonlinear system and a fast algorithm using digital laguerre filters. In *15th NIBB Conference, Okazaki, Japan*, pages 14–62.

Orr, M. J. (1995). Regularization in the selection of radial basis function centers. *Neural computation*, 7(3):606–623.

Palm, G. (1979). On representation and approximation of nonlinear systems. *Biological Cybernetics*, 34(1):49–52.

Pantazis, A., Segaran, A., Liu, C.-H., Nikolaev, A., Rister, J., Thum, A. S., Roeder, T., Semenov, E., Juusola, M., and Hardie, R. C. (2008). Distinct roles for two histamine receptors (hcla and hclb) at the drosophila photoreceptor synapse. *The Journal of Neuroscience*, 28(29):7250–7259.

Paulk, A., Millard, S. S., and van Swinderen, B. (2013). Vision in drosophila: seeing the world through a model's eyes. *Annual review of entomology*, 58:313–332.

Pearson, R. K. (1995). Nonlinear input/output modelling. *Journal of Process Control*, 5(4):197–211.

Pece, A., French, A., Korenberg, M., and Kuster, J. (1990). Nonlinear mechanisms for gain adaptation in locust photoreceptors. *Biophysical journal*, 57(4):733.

Peng, Z., Lang, Z.-Q., and Billings, S. (2007). Non-linear output frequency response functions for multi-input non-linear volterra systems. *International Journal of Control*, 80(6):843–855.

Peretz, A., Abitbol, I., Sobko, A., Wu, C.-F., and Attali, B. (1998). A Ca2+/Calmodulin-Dependent Protein Kinase ModulatesDrosophila Photoreceptor K+ Currents: A Role in Shaping the Photoreceptor Potential. *The Journal of Neuroscience*, 18(22):9153–9162.

Peyton Jones, J. and Choudhary, K. (2012). Output frequency response characteristics of nonlinear systems. part i: general multi-tone inputs. *International Journal of Control*, 85(9):1263–1278.

Pisoni, E., Farina, M., Carnevale, C., and Piroddi, L. (2009). Forecasting peak air pollution levels using narx models. *Engineering Applications of Artificial Intelligence*, 22(4):593–602.

Pumir, A., Graves, J., Ranganathan, R., and Shraiman, B. I. (2008). Systems analysis of the single photon response in invertebrate photoreceptors. *Proceedings of the National Academy of Science*, 105:10354–10359.

Raghu, S. V. and Borst, A. (2011). Candidate glutamatergic neurons in the visual system of drosophila. *PLoS One*, 6(5):e19472.

Rankin, C. H., Beck, C. D., and Chiba, C. M. (1990). Caenorhabditis elegans: a new model system for the study of learning and memory. *Behavioural brain research*, 37(1):89–92.

Reppert, S. M., Gegear, R. J., and Merlin, C. (2010). Navigational mechanisms of migrating monarch butterflies. *Trends in neurosciences*, 33(9):399–406.

Rister, J., Pauls, D., Schnell, B., Ting, C.-Y., Lee, C.-H., Sinakevitch, I., Morante, J., Strausfeld, N. J., Ito, K., and Heisenberg, M. (2007). Dissection of the peripheral motion channel in the visual system of drosophila melanogaster. *Neuron*, 56(1):155–170.

Rivera-Alba, M., Vitaladevuni, S. N., Mishchenko, Y., Lu, Z., Takemura, S.-y., Scheffer, L., Meinertzhagen, I. A., Chklovskii, D. B., and de Polavieja, G. G. (2011). Wiring economy and volume exclusion determine neuronal placement in the drosophila brain. *Current Biology*, 21(23):2000–2005.

Sakai, H. M. (1992). White-noise analysis in neurophysiology. *Physiological Reviews*, 72(2):491–505.

Salcedo, E., Huber, A., Henrich, S., Chadwell, L. V., Chou, W.-H., Paulsen, R., and Britt, S. G. (1999). Blue-and green-absorbing visual pigments ofdrosophila: Ectopic expression and physiological characterization of the r8 photoreceptor cell-specific rh5 and rh6 rhodopsins. *The Journal of Neuroscience*, 19(24):10716–10726.

Sarthy, P. V. (1991). Histamine: a neurotransmitter candidate for drosophila photoreceptors. *Journal of neurochemistry*, 57(5):1757–1768.

Schwarz, G. et al. (1978). Estimating the dimension of a model. *The annals of statistics*, 6(2):461–464.

Scott, K., Sun, Y., Beckingham, K., and Zuker, C. S. (1997). Calmodulin regulation of drosophila light-activated channels and receptor function mediates termination of the light response in vivo. *Cell*, 91(3):375–383.

Simoncelli, E. P. and Olshausen, B. A. (2001). Natural Image Statistics and Neural Representation. *Annual Review of Neuroscience*, 24(1):1193–1216.

Sjöberg, J., Zhang, Q., Ljung, L., Benveniste, A., Delyon, B., Glorennec, P.-Y., Hjalmarsson, H., and Juditsky, A. (1995). Nonlinear black-box modeling in system identification: a unified overview. *Automatica*, 31(12):1691–1724.

Solares, J. R. A., Wei, H.-L., Boynton, R., Walker, S. N., and Billings, S. A. (2016). Modelling and prediction of global magnetic disturbance in near-earth space: a case study for kp index using narx models. *Space Weather*.

Song, Z., Coca, D., Billings, S., Postma, M., Hardie, R. C., and Juusola, M. (2009). Biophysical Modeling of a Drosophila Photoreceptor. In Leung, C. S., Lee, M., and Chan, J. H., editors, *Neural Information Processing*, number 5863 in Lecture Notes in Computer Science, pages 57–71. Springer Berlin Heidelberg.

Song, Z., Postma, M., Billings, S. A., Coca, D., Hardie, R. C., and Juusola, M. (2012). Stochastic, adaptive sampling of information by microvilli in fly photoreceptors. *Current Biology*, 22(15):1371–1380.

Stone, M. (1974). Cross-validatory choice and assessment of statistical predictions. *Journal of the Royal Statistical Society. Series B (Methodological)*, pages 111–147.

Swain, A. and Billings, S. (2001). Generalized frequency response function matrix for mimo non-linear systems. *International Journal of Control*, 74(8):829–844.

Takalo, J., Ignatova, I., Weckström, M., and Vähäsöyrinki, M. (2011). A novel estimator for the rate of information transfer by continuous signals. *PloS one*, 6(4):e18792.

Takemura, S.-y., Karuppudurai, T., Ting, C.-Y., Lu, Z., Lee, C.-H., and Meinertzhagen, I. A. (2011). Cholinergic circuits integrate neighboring visual signals in a drosophila motion detection pathway. *Current Biology*, 21(24):2077–2084.

Tamara, G.-B. P. (2009). *Photoreceptor spatial performance of the fruit Drosophila melanogaster and the killer fly Coenosia attenuata*. PhD thesis, The University of Sheffield.

Trujillo-Cenóz, O. (1965). Some aspects of the structural organization of the intermediate retina of dipterans. *Journal of ultrastructure research*, 13(1):1–33.

van den Bosch, P. P. and van der Klauw, A. C. (1994). *Modeling, identification and simulation of dynamical systems*. crc Press.

van Hateren, J. (1997). Processing of natural time series of intensities by the visual system of the blowfly. *Vision Research*, 37(23):3407–3416.

Van Hateren, J. (1997). Processing of natural time series of intensities by the visual system of the blowfly. *Vision research*, 37(23):3407–3416.

Van Hateren, J. and Snippe, H. (2001). Information theoretical evaluation of parametric models of gain control in blowfly photoreceptor cells. *Vision research*, 41(14):1851–1865.

van Hateren, J. H. (1997). Processing of natural time series of intensities by the visual system of the blowfly. *Vision research*, 37(23):3407–3416.

van Hateren, J. H. and Snippe, H. P. (2001). Information theoretical evaluation of parametric models of gain control in blowfly photoreceptor cells. *Vision research*, 41(14):1851–1865.

Van Steveninck, R. d. R. and Laughlin, S. (1996). The rate of information transfer at graded-potential synapses. *Nature*, 379(6566):642–645.

Victor, J. D. and Canel, A. (1992). A relation between the akaike criterion and reliability of parameter estimates, with application to nonlinear autoregressive modelling of ictal eeg. *Annals of biomedical engineering*, 20(2):167–180.

Vidal-Rosas, E. E., Billings, S. A., Zheng, Y., Mayhew, J. E., Johnston, D., Kennerley, A. J., and Coca, D. (2014). Reduced-order modeling of light transport in tissue for real-time monitoring of brain hemodynamics using diffuse optical tomography. *Journal of biomedical optics*, 19(2):026008–026008.

Vogt, N. and Desplan, C. (2007). The first steps in drosophila motion detection. *Neuron*, 56(1):5–7.

Volterra, V. (2005). *Theory of functionals and of integral and integro-differential equations*. Courier Corporation.

Weckström, M. (1989). Light and dark adaptation in fly photoreceptors: duration and time integral of the impulse response. *Vision research*, 29(10):1309–1317.

Wei, H.-L., Lang, Z.-Q., and Billings, S. A. (2007). An algorithm for determining the output frequency range of volterra models with multiple inputs. *IEEE Transactions on Circuits and Systems II: Express Briefs*, 54(6):532–536.

Wernet, M. F., Labhart, T., Baumann, F., Mazzoni, E. O., Pichaud, F., and Desplan, C. (2003). Homothorax switches function of drosophila photoreceptors from color to polarized light sensors. *Cell*, 115(3):267–279.

Whitworth, A. J. (2011). 1 drosophila models of parkinson's disease. *Advances in genetics*, 73:1.

Wilson, M. (1978). The functional organisation of locust ocelli. *Journal of comparative physiology*, 124(4):297–316.

Yamaguchi, S., Wolf, R., Desplan, C., and Heisenberg, M. (2008). Motion vision is independent of color in drosophila. *Proceedings of the National Academy of Sciences*, 105(12):4910–4915.

Yue, R., Billings, S., and Lang, Z.-Q. (2005). An investigation into the characteristics of non-linear frequency response functions. part 1: Understanding the higher dimensional frequency spaces. *International Journal of Control*, 78(13):1031–1044.

Zhang, H. and Billings, S. (1993). Analysing non-linear systems in the frequency domain–i. the transfer function. *Mechanical Systems and Signal Processing*, 7(6):531–550.

Zhang, L. F., Zhu, Q. M., and Longden, A. (2007). A set of novel correlation tests for nonlinear system variables. *International Journal of Systems Science*, 38(1):47–60.

Zhao, X. and Marmarelis, V. (1998). Nonlinear parametric models from volterra kernels measurements. *Mathematical and Computer Modelling*, 27(5):37–43.

Zheng, L., de Polavieja, G. G., Wolfram, V., Asyali, M. H., Hardie, R. C., and Juusola, M. (2006). Feedback network controls photoreceptor output at the layer of first visual synapses in drosophila. *The Journal of general physiology*, 127(5):495–510.

Zheng, L., Nikolaev, A., Wardill, T. J., O'Kane, C. J., de Polavieja, G. G., and Juusola, M. (2009). Network adaptation improves temporal representation of naturalistic stimuli in drosophila eye: I dynamics. *PLoS One*, 4(1):e4307.

Zhu, Q. and Billings, S. (1994). Identification of polynomial & rational narmax models. *IFAC Proceedings Volumes*, 27(8):259–264.